Droplet Assisted Growth and Shaping: A broadly applicable chemical synthesis method for in situ shaping of multiple nanostructures

---

Dissertation
zur
Erlangung der naturwissenschaftlichen Doktorwürde
(Dr. sc. nat.)
vorgelegt der
Mathematisch-naturwissenschaftlichen Fakultät
der
Universität Zürich
von
Naeem-ul-Hasan Saddiqi
aus
Pakistan

Promotionskomitee
Prof. Dr. Stefan Seeger (Vorsitz)
Prof. Dr. Karl-Heinz Ernst
Prof. Dr. Roland K. O. Sigel

Zürich, 2019

Acknowledgments

CMSZH
CHEMICAL MOLECULAR SCIENCES ZURICH
GRADUATE SCHOOL

First and foremost, I would like to thank Prof. Dr. Stefan Seeger for giving me the opportunity to carry out my doctoral thesis research in his group. I am very thankful to him for giving me the freedom to explore the science of interfaces. I cannot thank him enough for his continuous support, scientific supervision, constant optimism and tremendous amount of confidence he placed in me.

Prof. Dr. Karl-Heinz Ernst and Prof. Dr. Roland K.O. Sigel, I express my gratitude for agreeing to supervise my thesis as part of the Doctoral Committee.

Associate Prof. Dr. Debabrata Patra, I would like to express a special appreciation for his guidance and collaboration in early years of my doctoral research. His consistent support and valuable discussions laid the foundation of my doctoral research.

Dr. Georg Artus, I am very thankful for his invaluable help he provided me throughout the course of my doctoral research.

Dr. Samet Varol, I am very glad and thankful to have him as a colleague who has always been very welcoming to discuss scientific problems and providing useful and thoughtful insights of the crucial details.

I am very grateful to Dr. Malay Patra for the helpful and fruitful discussions over coffee breaks.

Dr. sc nat. Andres Käch of the Center for Microscopy and Image Analysis (ZMB) of University of Zurich I would like to thank him for the helpful discussions and introducing me to Scanning and Transmission Electron Microscopy. His continuous support in sample preparation, imaging, composition analysis and interpretation of the data have played a vital role in my doctoral research. I would also like to acknowledge ZMB for providing imaging facilities.

Xiaotian Zhang I would like to thank him for being an amazing office mate who always maintained a positive atmosphere in the office.

I would like to thank the whole Seeger group for keeping a friendly and nice working environment in the group.

Special thanks to Fabienne Stutz for always helping in organizational matters. I would also like to thank the staff, Roland Zehnder, Chantal Henningsen-Conus, Larissa Mostacciuolo, Dr.

Sabine Stockhause and Sascha Giger for their continuous assistance during the course of my PhD.

I am indebted to Graduate School of Chemical and Molecular Sciences Zurich (CMSZH) for the generous financial support, and joyful annual winter retreats.

Finally, my family and friends I am very thankful for their continuous support, encouragement and never-ending patience to keep me balanced. Without their love and support, this work would never be possible.

Abstract

Tuning the surface of a substance by tailoring the physical, chemical and mechanical properties is a vital field of material science. The topic which has received tremendous amount of interest of the scientific community is to control physical and chemical properties of a surface on micro and nanometer level to generate surfaces with unique functionalities. An example are superhydrophobic surfaces which exhibit unique wetting properties due to its low surface energy and high surface roughness. These superhydrophobic surfaces are inspired by the objects in nature such as lotus leaves or water striders.

In this work the fabrication of such superhydrophobic surfaces, surface modifications and extension of their area of application are discussed. For the synthesis, chemical vapor deposition of silanes using ambient conditions of temperature and pressure have been applied. The developed method yields coatings with minimum requirements of processing and lab instrumentation. The chemical vapor deposition method yields thick coatings of highly entangled networks of silicone nanofilaments (SNFs). SNFs are essentially composed of polymethylsilsesquioxane with diameter in the range of 50-80 nm and length ranging from nanometer to micrometer scale. The as prepared coatings show full optical transparency and high water repellency. The coating deposition process has been developed for various substrates such as glass, silicon, polymer and textile to explore the application of superhydrophobic surfaces for self-cleaning, water repellency and oil/water separation.

The SNFs based coatings have also been used for biological applications where the surface of nanofilaments has been modified by hydroxyl, carboxylic acid and amine functional groups to study their influence on biomimetic growth of hydroxyapatite for faster bone regeneration and repair.

In addition, the extension of SNFs to design smart materials has also been discussed in this work where hybrid coatings composed of silicone nanofilaments-carbon nanofibers have been prepared by facile dip-coating method. The as prepared coatings have been applied as a multifunctional coating exhibiting extreme water repellency, electric conductivity and transparency. In addition, the stability of multifunctional coatings in extreme conditions such as high humidity, water immersion and long term corrosive chemical exposure has also been studied.

The synthesis of SNFs depends on the formation of water droplets at the surface of the substrate which determine the shape of growing materials. The mechanism of droplet assisted growth and shaping (DAGS) was applied to non-silicone systems to synthesize 1D nanostructures. The DAGS method was for the first time applied to synthesize germanium oxide nanofilaments (GNFs), alumina nanofilaments (AlNFs) and mixed alumina-silicone based nanofilaments (Al-SiNFs). The influence of various reaction parameters as well as type of precursors on the synthesis of 1D nanostructures using DAGS chemistry have also been discussed in this work. This can be considered as a break-through since not only new types of nanostructures have been synthesized for the first time, but it also shows the very first time that the newly developed DAGS reaction mechanism is not silicone-specific, but a generally applicable pathway to chemically synthesize and in situ shape nano- and microparticles of different materials.

The results presented here show that SNFs open a new avenue to develop coatings with tunable wetting properties as well as they have shown potential for biomineralization applications. The ease of fabrication in terms of room temperature processing and no liquid waste production, and the properties of SNFs in terms of water repellency, optical transparency, and chemical inertness make them to stand out from the known superhydrophobic coatings. In addition, the DAGS mechanism of synthesis has been extended to synthesize various 1D nanostructures, which show its universality and its potential to synthesis various nanomaterials using facile processing.

Zusammenfassung

Die Optimierung der Oberflächenstruktur einer Substanz durch Anpassung deren physikalischen, chemischen sowie mechanischen Eigenschaften gehört zu den wichtigsten Bereichen der Materialwissenschaft. Das Thema, welches vielfach auf enormes Interesse innerhalb der wissenschaftlichen Gemeinschaft stößt, ist die Kontrolle der physikalischen und chemischen Eigenschaften einer Oberfläche auf der Mikro- und Nanometerebene, um Oberflächen mit einzigartigen Funktionalitäten zu schaffen. Als Beispiel einer solchen Oberfläche ist die superhydrophobe Oberfläche zu erwähnen, welche einzigartige Benetzungseigenschaften durch geringe Oberflächenenergie und hohe Oberflächenrauigkeit aufweist. Die Idee zur Herstellung sogenannter superhydrophoben Oberflächen beruht auf der Natur selbst, wie zum Beispiel auf Lotusblättern oder Wasserläufern.

In dieser Arbeit wird die Herstellung solcher superhydrophoben Oberflächen, deren Oberflächen-Modifikation sowie die Erweiterung ihrer Anwendungen thematisch behandelt. Für die Synthese wurde die chemische Gasphasenabscheidung von Silanen unter Umgebungsbedingungen von Temperatur und Druck eingesetzt. Die entwickelte Methode ermöglicht Beschichtungen mit minimalen Anforderungen an Verarbeitungsprozessen sowie Laborausrüstung. Die chemische Gasphasenabscheidung liefert eine dicke Beschichtung aus einem hochverstrickten Geflecht von Silikon-Nanofilamenten (SNFs). SNFs bestehen im Wesentlichen aus Polymethylsilsesquioxan mit einem Durchmesser im Bereich von 50-80 nm und einer Länge im Nanometer- bis Mikrometerbereich. Die so vorbereiteten Beschichtungen zeigen volle optische Transparenz und hohe wasserabweisende Wirkung. Der Beschichtungsprozess wurde für verschiedene Substrate wie Glas, Silizium, Polymer und Textil entwickelt, um die Anwendung superhydrophober Oberflächen für die Selbstreinigung, Wasserabweisung, sowie die Öl/Wasser-Trennung zu untersuchen.

Die auf SNFs basierenden Beschichtungen wurden auch für biologische Anwendungen verwendet, bei denen die Oberfläche von Nanofilamenten durch Hydroxyl-, Carbonsäure- und Aminogruppen modifiziert wurde, um ihren Einfluss auf das biomimetische Wachstum von Hydroxylapatit für eine schnellere Knochenregeneration und -reparatur zu untersuchen.

Darüber hinaus wurde in dieser Arbeit auch die Ausdehnung der SNFs auf das Design intelligenter Materialien diskutiert, wobei Hybridbeschichtungen aus Silikon-Nanofilament-Kohlenstoff-Nanofasern durch einfache Tauchbeschichtung hergestellt wurden. Die vorbereiteten Beschichtungen wurden als multifunktionale Beschichtung aufgebracht, die eine extreme Wasserabweisung, elektrische Leitfähigkeit und Transparenz aufweisen. Zusätzlich wurde auch die Stabilität von multifunktionalen Beschichtungen unter extremen Bedingungen, wie hohe Luftfeuchtigkeit, Wasserlagerung und langfristige korrosive chemische Belastung, untersucht.

Die Synthese von SNFs hängt von der Bildung von Wassertropfen auf der Oberfläche des Substrats ab, diese bestimmt die Form des wachsenden Materials. Der Mechanismus des tropfenunterstützten Wachstums und Formens (DAGS) wurde erstmals auf silikonfreie Systeme angewendet, um 1D-Nanostrukturen zu synthetisieren. Die DAGS-Methode wurde zur Synthese von Germaniumoxid-Nanofilamenten (GNFs), Aluminiumoxid-Nanofilamenten (AlNFs) und Aluminiumoxid-Silizium- Nanofilamenten (Al-SiNFs) eingesetzt. Der Einfluss verschiedener Reaktionsparameter sowie Vorläufersubstanzen auf die Synthese von 1D-Nanostrukturen mittels DAGS-Chemie wird ebenfalls in dieser Arbeit diskutiert. Dies kann als Durchbruch in der chemischen Synthese betrachtet werden, da nicht nur neuartige Nanostrukturen hergestellt wurden, sondern die allgemeine Anwendbarkeit des DAGS-Mechanismus gezeigt wird, um Nano- und Mikrostrukturen unterschiedlicher Form und verschiedensten Materialien zu synthetisieren.

Die hier vorgestellten Ergebnisse zeigen, dass SNFs einen neuen Weg zur Entwicklung von Beschichtungen mit veränderbaren Benetzungseigenschaften eröffnen und das Potenzial für Biomineralisationsanwendungen aufgezeigt haben. Die einfache Herstellung in Bezug auf Raumtemperaturverarbeitung und Abwesenheit von Flüssigabfällen sowie die Eigenschaften der SNFs in Bezug auf Wasserabweisung, optische Transparenz und chemische Inaktivität heben sie von den bekannten superhydrophoben Beschichtungen ab. Darüber hinaus wurde der DAGS-Synthese-Mechanismus erweitert, um verschiedene 1D-Nanostrukturen zu synthetisieren, die ihre Universalität und ihr Potenzial zur Synthese verschiedener Nanomaterialien durch einfache Verarbeitung zeigen.

List of Publications

Journal Publications

- N. H. Saddiqi, D. Patra, S. Seeger
  Hydroxyapatite Biomineralization on Functionalized Silicone Nanofilaments
  Colloid and Interface Science Communications 16, 1-5 (2017)

- N. H. Saddiqi, D. Patra, S. Seeger
  Room-Temperature Synthesis of Germanium Oxide Nanofilaments and Their Potential Use as Luminescent Self-Cleaning Surfaces
  ChemPhysChem 20, 4 (2019)
  Selected as Front Cover

- N. H. Saddiqi, S. Seeger
  Chemically Resistant, Electric Conductive, and Superhydrophobic Coatings
  Advanced Materials Interfaces 6, 7 (2019)
  Selected as Front Cover

- N. H. Saddiqi, S. Seeger
  Droplet Assisted Growth and Shaping of Alumina and Mixed Alumina-Silicone 1-Dimensional Nanostructures.
  Journal of Colloid and Interface Science *(accepted)*

Posters Presentations

- N. H. Saddiqi, S. Seeger
  Synthesis of 1D Al and Al-Si Nano-structures using Facile Room Temperature Chemical Vapor Deposition
  35th Meeting of Surface Science and Thin Films Community of Switzerland, Fribourg, Switzerland, February 1, 2018

- N. H. Saddiqi, D. Patra, S. Seeger
  Silicone Nanofilaments: A Support Material for Biomimetic Growth of Hydroxyapatite

13th International Conference on Nanosciences & Nanotechnologies, Thessaloniki, Greece, July 5-8, 2016

Contents

Acknowledgments ii
Abstract iv
Zusammenfassung vi
List of Publications viii
Abbreviations xiii
1. Introduction 1
2. Theory and background 3
2.1 Wetting of solids 3
2.2 Wetting of rough solids 4
2.3 Wetting of heterogeneous solids 5
2.4 Super wetting and super non-wetting 6
2.5 Synthesis of nanomaterials 7
2.5.1 Physical deposition methods 8
2.5.1.1 Thermal evaporation deposition 9
2.5.1.2 Sputtering 9
2.5.1.3 Laser ablation 11
2.5.1.4 Lithography 12
2.5.1.4.1 Colloidal lithography 12
2.5.1.4.2 Electron beam lithography 13
2.5.1.5 Confined growth 14
2.5.2 Chemical deposition method 16
2.5.2.1 Microwave plasma chemical vapor deposition 16
2.5.2.2 Hot filament chemical vapor deposition 17
2.5.2.3 Room temperature chemical vapor deposition 18
2.6 The growth mechanisms 23
2.6.1 Vapor liquid solid growth mechanism 23
2.6.2 Vapor solid growth mechanism 24
2.6.3 Solution liquid solid growth mechanism 25
2.6.4 Droplet assisted growth and shaping mechanism 26
3. Materials and Methods 29
3.1 Chemicals 29
3.2 Substrates 30
3.3 Synthesis of silicone nanofilaments 30
3.3.1 Cleaning and surface activation of substrates 30

3.3.2 Chemical vapor deposition 31
3.3.2.1 Protocol I 32
3.3.2.2 Protocol II 32
3.4 Hydroxyapatite biomineralization 33
3.4.1 Functionalization of SNFs 33
3.4.2 Preparation of simulated body fluid 33
3.5 Preparation of superhydrophobic/conductive surfaces by dip coating 34
3.5.1 Preparation of hybrid surfaces with Parafilm addition 34
3.5.2 Sheet resistance measurement 35
3.5.3 Environmental durability 35
3.5.4 Chemical durability 35
3.5.5 Mechanical durability 36
3.6 Synthesis of other nanomaterials by CVD 36
3.6.1 Synthesis of germanium-based nanomaterials 36
3.6.1.1 Cleaning and surface activation of substrates 36
3.6.1.2 Chemical vapor deposition of germanium oxide nanofilaments (GNFs) 36
3.6.1.3 Annealing 36
3.6.1.4 Treatment with silanes 37
3.6.2 Synthesis of alumina-based nanomaterials 37
3.6.2.1 Cleaning and surface activation of substrates 37
3.6.2.2 Chemical vapor deposition 37
3.6.2.3 Annealing 37
3.6.3 Synthesis of mixed alumina-silicone based nanomaterials 38
3.6.3.1 Cleaning and surface activation of substrates 38
3.6.3.2 Chemical vapor deposition 38
3.6.3.3 Annealing 38
3.7 Characterization 38
3.7.1 Scanning electron microscopy 38
3.7.2 Transmission electron microscopy 39
3.7.3 Energy dispersive x-ray spectroscopy 39
3.7.4 IR spectroscopy 39
3.7.5 UV-Vis spectroscopy 39
3.7.6 Photoluminescence spectroscopy 39
3.7.7 X-ray photoelectron spectroscopy 39
3.7.8 Characterization of superhydrophobicity 40

4. Results and Discussion 41
4.1 Hydroxyapatite biomineralization 41
4.1.1 Synthesis and functionalization of SNFs 42
4.1.2 Growth of Hydroxyapatite 44
4.1.3 Time dependent studies of HA biomineralization 48
4.2 Multifunctional electrical conductive and superhydrophobic coatings 51
4.2.1 Fabrication of multifunctional coatings 52
4.2.2 Microstructure of multifunctional coatings 52
4.2.3 Electrical conduction and superhydrophobicity 54
4.2.4 Optical transparency 56
4.2.5 Other surface properties 57
4.2.6 Environmental durability of the coatings 59
4.2.7 Chemical durability of the coatings 61
4.2.8 Mechanical durability of the coatings 66
4.3 Chemical vapor deposition of Germanium oxide nanofilaments 73
4.3.1 Synthesis of germanium oxide nanofilaments 75
4.3.2 DAGS mechanism and influence of humidity on GNFs synthesis 78
4.3.3 Time dependent growth of GNFs 81
4.3.4 Thermal stability of GNFs 82
4.3.5 Photoluminescence spectra of GNFs 84
4.3.6 Application of GNFs for superhydrophobicity 85
4.4 Chemical vapor deposition of Aumina and mixed Alumina-Silicone based nanostructures 92
4.5 Synthesis of alumina nanostructures 92
4.5.1 The influence of relative humidity and reaction time 94
4.5.2 Thermal stability studies 98
4.6 Synthesis of mixed alumina-silicone nanostructures 99
4.6.1 Influence of relative humidity and reaction time 105
4.6.2 Thermal stability studies 109
5. Summary and outlook 114
References 118
Curriculum Vitae 125

Abbreviations

AlNFs	Alumina nanofilaments
Ar	Argon
Al-SiNFs	Alumina-Silicone nanofilaments
CNFs	Carbon nanofibers
CVD	Chemical vapor deposition
DAGS	Droplet assisted growth and shaping
EDX	Energy dispersive X-ray spectroscopy
FTIR	Fourier transform infra-red
GNFs	Germanium oxide nanofilaments
HA	Hydroxyapatite
HFCVD	High frequency chemical vapor deposition
HFMOCVD	High frequency metal oxide chemical vapor deposition
IR	Infra-red
MMA	Methylmethacrylate
N_2	Nitrogen
PF	Parafilm
PMMA	Poly(methylmethacrylate)
RF	Radio frequency
RIE	Reactive ion etching
SEM	Scanning electron microscope
SAED	Selected area electron diffraction
SNFs	Silicone nanofilaments
SBF	Simulated body fluid
SLS	Solution liquid solid

TEM	Transmission electron microscope
TCES	Trichloroethylsilane
TCMS	Trichloromethylsilane
TEA	Triethylaluminum
TMA	Trimethylaluminum
UV-Vis	Ultra-violet visible
VLS	Vapor liquid solid
VS	Vapor solid
XPS	X-ray photoelectron spectroscopy

1. Introduction

Fabrication of the surfaces which exhibit unique functionalities is an important field of material science and it has gained numerous attention from research and industry. The advancements in nanotechnology have revolutionized the realization of surfaces in real life applications. An example is the surface which mimics the objects in nature e.g. lotus leaf or water strider. These micro- and nanostructured surfaces possess distinctive wetting properties and have been found very useful for water proofing, anti-wetting and self-cleaning applications. Silicone nanofilaments (SNFs) [1] which have been discovered more than a decade ago exhibit extreme anti-wetting and self-cleaning properties due to the high roughness generated by highly entangled network at the surface. Due to their unique chemical composition (presence of organic groups at the surface) and high surface roughness, the surfaces fabricated with SNFs show high water contact angles and low sliding angles. Due to the sliding of water droplets at slightly titled surfaces, SNFs exhibit excellent dirt repellency and self-cleaning properties.

SNFs have been synthesized at room temperature using gas and liquid phase chemical syntheses methods [1] [2]. The gas phase method is of significant importance due to solvent free handling and ease in scalability [3]. The as synthesized SNFs possess very good thermal stability, chemical inertness and stability in various environmental conditions [4]. The ability to coat almost any substrate material after appropriate surface activation and tuning the surface properties is hence very versatile [5] [6]. Due to these properties, the materials coated with SNFs have been found useful for various surface science applications such as superhydrophobicity, superhydrophilicity, superoleophobicity, superoleophilicity, self-cleaning, anti-fouling and oil/water separation [7]. The ease of modifying surface wetting properties by SNFs coatings has been explored to fabricate surfaces with patterned superhydrophobic and superhydrophilic regions which is useful for liquid handling and water harvesting applications [8]. In addition, the patterned surfaces have been valuable for designing microfluidic devices [9]. The high surface area provided by 1D SNFs has been explored for catalytic [10], antibacterial [11] and protein adsorption applications [12].

The simplicity of the synthesis methods applied for the fabrication of SNFs based surfaces and the ability to coat various substrates indicate the potential of SNFs. The aim of this thesis is to expand the spectrum of SNFs use in various material science applications and extend the facile synthesis method to non-silicon material systems. For this purpose, an overview of various methods used for the synthesis of 1D nanomaterials and different mechanisms for the growth of 1D nanostructures have also been discussed in the thesis.

The second part of the thesis focuses on high surface area of SNFs which is applied for biological applications where various functional groups attached at the surface of SNFs have been studied to grow hydroxyapatite (HA) for orthopedic implantation application. The functionalized SNFs immersed in a simulated body fluid (SBF) which has composition similar to human blood plasma, was checked for their bioactivity. The bioactivity of the functionalized SNFs was tested in terms of HA growth.

The third part of the thesis emphases on extending the use of SNFs to fabricate multifunctional coatings. The substrates coated with SNFs were dip-coated in the suspension of inexpensive carbon nanofibers to yield electrically conductive coatings with tunable transparency. The prepared multifunctional coatings exhibited variable wettability which was explored for water droplet transportation and droplet confined reactions. Furthermore, the stability of the multifunctional coatings in harsh environmental conditions such as extreme humidity, water contact, and long-term exposure in acidic and basic aqueous solutions was also tested. The mechanical properties of such coatings which is a crucial and least addressed topic, was also investigated and the mechanical robustness was enhanced by the addition of a polymer.

The fourth and fifth part of the thesis focuses on the synthesis method itself. The gas phase method applied for the synthesis of SNFs relies on the formation of water droplets at the surface which determine the shape of growing 1D nanostructures. Due to the ease of this synthesis method in terms of i) application of ambient temperature and pressure, ii) solvent free handling, iii) ease in scalability and iv) less complicated instrumentation, this synthesis method is environment friendly and easy to execute. The extension of this method to synthesize 1D nanostructures of other materials such as germanium oxide, alumina and alumina-silicone is also discussed in this thesis. The influence of various reaction conditions such as relative humidity, reaction time and type of starting precursors have also been included in this thesis. In addition, the application of 1D germanium oxide nanofilaments (GNFs) synthesized by this method for self-cleaning applications is also discussed in the thesis.

2. Theory and background

2.1 Wetting of solids

When a liquid drop comes in contact with the solid surface, the interfacial energies of the liquid and solid surface determine the extent to which the surface is wetted by the liquid drop. The liquid drop can either spread on the solid surface (wetting) or not spread on the solid surface (non-wetting). The degree of wetting determines the shape of the liquid drop which can be described by Young's equation. In 1805 Thomas Young proposed an equation which relates the shape of the liquid drop and interfacial energies [13]:

$$cos\theta = \frac{\gamma_S - \gamma_{SL}}{\gamma_L} \quad \text{(Equation 2.1)}$$

Where γ_S, γ_L and γ_{SL} are solid/vapor, liquid/vapor and solid/liquid interfacial energies respectively. The θ represents the angle at which the liquid drop contacts the solid surface. The contact of liquid drop with the solid surface can also be called three phase contact line (liquid/solid/vapor contact line). Three phase contact line and the shape of the drop can be understood by balancing the interface energies as shown in Figure 2.1.

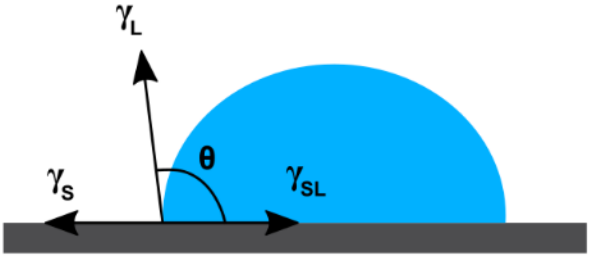

Figure 2.1. Three phase contact line and balance of interface energies

By using Young's equation, the interfacial energies can be easily correlated to the shape of the drop which is determined by θ. When the contact angle (θ) is below 90°, the wetting of surface occurs. If the contact angle is above 90°, the drop is non-wetting the surface. In other terms, the surface exhibiting contact angle below 90° the surface is called hydrophilic, and surface is hydrophobic for the contact angle 90° or above (Figure 2.2).

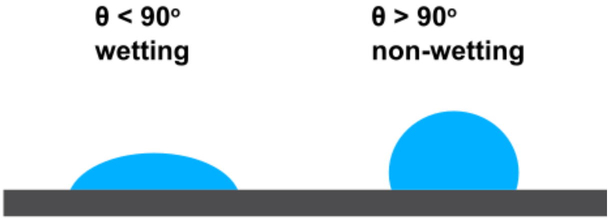

Figure 2.2. Contact angles on the surface for wetting and non-wetting states

2.2 Wetting of rough solids

The Young's equation represented in equation 2.1 is valid only for a flat surface. This equation does not hold true for the rough surface because the balance of interfacial energies at the contact line is different for a rough surface.

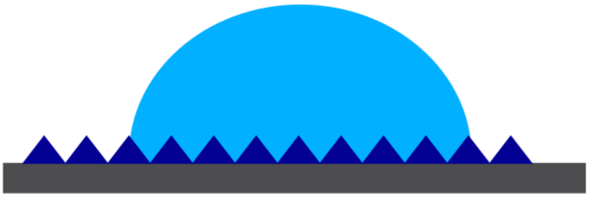

Figure 2.3. Wetting of a rough surface

To account for the roughness, a roughness factor *r* was introduced by Wenzel [14]. The roughness factor relates the solid surface tensions of the flat surface to the surface tensions of the rough surface.

$$r = \frac{actual\ area}{geometrical\ area} \qquad \text{(Equation 2.2)}$$

The surface tension of rough surface as a function of flat surface is related as:

$$\gamma^* = r \cdot \gamma \qquad \text{(Equation 2.3)}$$

The new balance of surface forces:

$$cos\theta^* = \frac{\gamma_S^* - \gamma_{SL}^*}{\gamma_L} = r \cdot \left(\frac{\gamma_S - \gamma_{SL}}{\gamma_L}\right) \qquad \text{(Equation 2.4)}$$

The term $\frac{\gamma_S - \gamma_{SL}}{\gamma_L}$ represents Young's equation. So, the equation 2.4 can be written as:

$$cos\theta^* = r \cdot cos\theta \qquad \text{(Equation 2.5)}$$

The equation 2.5 is called Wenzel equation which correlates the contact angle measured on a rough surface to the intrinsic contact angle defined by the material properties. The Wenzel equation states the roughness enhances the intrinsic wetting of the surface, i.e. wettable surface will become more wettable and non-wettable surface will become more non-wettable.

2.3 Wetting of heterogeneous solids

The Young's equation described in equation 2.1 is valid only for flat surface which is perfectly homogenous in chemical composition. In other words, it does not take into account the difference of surface tension generated by the presence of different chemical species at the surface. Cassie Baxter introduced the factor to account for such chemical heterogeneities. The Cassie Baxter equation is given as [15]:

$$cos\theta^* = \sum_i f_i \, cos\theta_i \qquad \text{(Equation 2.6)}$$

Where f represents the solid fraction of different chemical fractions, and θ_i represents the contact angle on individual chemical fractions. The figure of surface with different chemical composition patches in shown in Figure 2.4.

Figure 2.4. The surface consisting of two different chemical components

For a surface which is composed of two different chemical components as shown in Figure 2.4, the Cassie Baxter equation is as follows:

$$cos\theta^* = f_1 cos\theta_1 + f_2 cos\theta_2 \qquad \text{(Equation 2.7)}$$

2.4 Super wetting and super non-wetting

The super wetting or super non-wetting means the condition at which the liquid drop completely spreads on the solid or is stays spherical on the solid surface. Super wetting conditions correspond to complete wetting and contact angle values approaching 0°. While super non-wetting condition corresponds to complete non-wetting of the solid and contact angle values of the liquid drop 150° or above.

For a perfectly flat solid, super wetting can be achieved when $\gamma_S - \gamma_{SL} > \gamma_L$. While super non-wetting condition can be achieved when $\gamma_{SL} - \gamma_S > \gamma_L$, which is not possible for a perfectly flat surface. The solids with the lowest surface energy such as fluorinated materials do not exhibit complete non-wetting state. But by introducing the roughness super wetting and super non-wetting conditions can be easily achieved.

The drop of liquid partially wets the solid surface when it comes in contact with the rough surface instead of complete wetting (as in Wenzel state). A layer of air is formed between the drop and the rough asperities of the surface as shown in Figure 2.5.

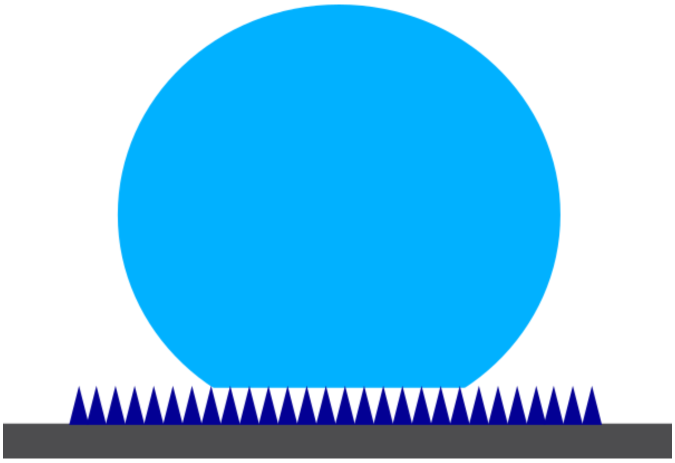

Figure 2.5. The partial wetting of highly rough solid surface

Taking into account the partial wetting, solid surface tensions becomes

$$\gamma^* = f \cdot \gamma \qquad \text{(Equation 2.8)}$$

Where *f* is the fraction of solid wetted by liquid.

Balancing the three-phase contact line for this situation yields:

$$cos\theta^* = \frac{f\gamma_S - f\gamma_{SL} - (1-f)\gamma_L}{\gamma_L} \qquad \text{(Equation 2.9)}$$

$$cos\theta^* = \frac{f(\gamma_S - \gamma_{SL} + \gamma_L)}{\gamma_L} - 1 \qquad \text{(Equation 2.10)}$$

Taking into account the Young's equation, the expression becomes

$$cos\theta^* = f(cos\theta + 1) - 1 \qquad \text{(Equation 2.11)}$$

Similar equation is obtained when surface is composed of two components in Cassie-Baxter state. The purpose of this section is to give a brief overview of surface wetting phenomenon and governing equations. The detailed discussion on the transition between Wenzel and Cassie-Baxter state can be found in the literature.

2.5 Synthesis of nanomaterials

Over the last few decades the advancements in the field of nanoscience has inspired researchers to discover new and innovative materials. In addition to finding new functional materials, efforts have also been made to tailor the fabrication of materials at nanoscale. Materials with at least one dimension in the range of 1-100 nanometers are usually referred as nanomaterials. The nanomaterials are broadly classified into different categories such as 0D, 1D and 2D depending on the morphology or shape. It is worth to mention that as the size is reduced, the materials exhibit different properties as compared to its bulk counter parts. The changes in the dimension lead to the change of both physical and chemical properties of materials.

1D nanomaterials carry a significant importance among all nanomaterials due to their high aspect ratio. 1D nanomaterials in the range of nanometers and length ranging from micrometer to millimeter scale is of vital importance for nano-electronics [16] [17] and catalysis [18] [19].

Due to their unique morphology 1D nanomaterials have found extensive applications such as solar-cells [20], sensors [21] [22], transistors [23], functional textiles [6], and smart windows [24]. 1D nanomaterials in the shape of tips [25], wires [26], tubes [27], filaments [1], fibers [28], belts [29], rods [30], cables [31], spirals [32], zigzag [33] structures have been prepared using different synthesis routes. However, during the synthesis of 1D nanomaterials, the control over the shape, morphology, size, uniformity and chemical composition is a challenging task. Therefore, the synthesis of 1D nanomaterials with controllable physical and chemical properties requires further development.

Various methods for the synthesis of 1D nanostructures have been developed over the course of years. Usually the classification of synthesis techniques can be done by the nature of the phases involved. The synthesis techniques which require presence of liquid phase for the synthesis are referred as wet chemical processes. Wet chemical synthesis involves different synthesis methods such as hydrothermal [34] [35] [36], solvothermal [37] [38] or sol-gel [39] [40]. In the other type of synthesis methods which do not require presence of liquid phase are referred as gas phase synthesis methods. The advantages of gas phase synthesis over wet chemical processing are mainly because of i) zero liquid waste production and ii) easy-scale up [3]. In this thesis only the details of gas phase synthesis will be discussed which will include various types of gas phase synthesis, different type of materials and the growth mechanisms.

The gas phase methods can be classified into two categories: i) physical deposition method and ii) chemical deposition method. Physical deposition or chemical deposition can be identified by the strategy involved for the synthesis. For example, physical deposition method such as lithography can be regarded as a good "top down" technique, while chemical deposition methods usually involve "bottom up" technique. In the next sections the details of physical and chemical deposition methods have been discussed.

2.5.1 Physical deposition methods

The physical deposition methods involve various types such as thermal evaporation, sputtering, laser ablation, lithography and confined growth etc. These methods have been used for the synthesis of various 1D metal oxides or compounds. The physical deposition methods do not involve any chemical reaction during the growth of 1D nanomaterials. The details of various physical deposition methods are discussed in following sections.

2.5.1.1 Thermal evaporation deposition

Thermal evaporation deposition method is one of the most important and widely used technique employed for the synthesis of 1D nanomaterials. As the name suggests it involves evaporation of substances due to heating at high temperature. Schematics of thermal evaporation method are shown in Figure 2.6. Thermal evaporation deposition usually involves a tube furnace connected with the supply of inert gas or the vacuum pump.

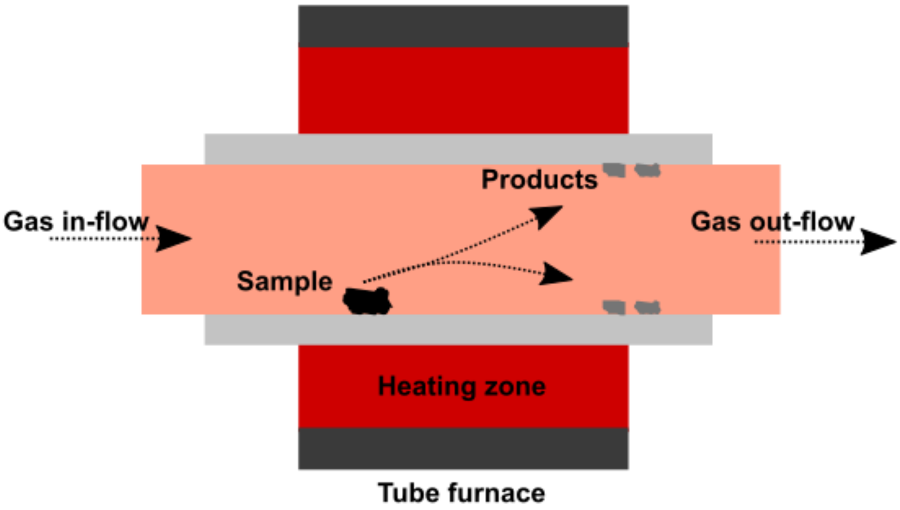

Figure 2.6. Schematics of a tube furnace used for the synthesis of 1D nanomaterials using thermal evaporation method. Reproduced with permission from [41]

The bulk material placed in the tube furnace vaporizes due to heating at high temperature. The vaporized material is deposited at a rather low temperature region inside the tube furnace and condenses to 1D structure. Due to the ease of synthesis and the ability to heat any material, thermal evaporation has been used to synthesize variety of 1D nanostructures of materials including ZnO [29] [42], SnO_2 [29] [43], In_2O_3 [29], CdO [29], PbO_2 [44], Ga_2O_3 [29], TiO_2 [45] and mixed structures of ZnO-Sn [46] and ZnO-Pb [46]. 1D nanomaterials in different forms such as nano-rods [42], nano-whiskers [43] and nano-belts [29] have also been synthesized by thermal evaporation method.

2.5.1.2 Sputtering

The radio frequency (RF) magnetron sputtering also known as sputtering method, is a technique which has been used frequently for the synthesis of 1D nanostructures. This process involves the generation of plasma by using RF. Usually argon (Ar) is used for plasma generation in sputtering process. Before the deposition process, the substrates are cleaned by using Milli-Q® water followed by rinsing with acetone and/or ethanol. The cleaned substrates are placed in the sputtering chamber and if required the sputtering chamber is evacuated to low pressure (~ 10^{-6} mbar). The evacuation of the chamber is usually done as a precaution to remove any remaining impurities from the chamber and the surface of the substrate. The target of the desired material is placed in the chamber. The sputtered material is deposited on the substrate. The schematics of the sputtering process are shown in Figure 2.7.

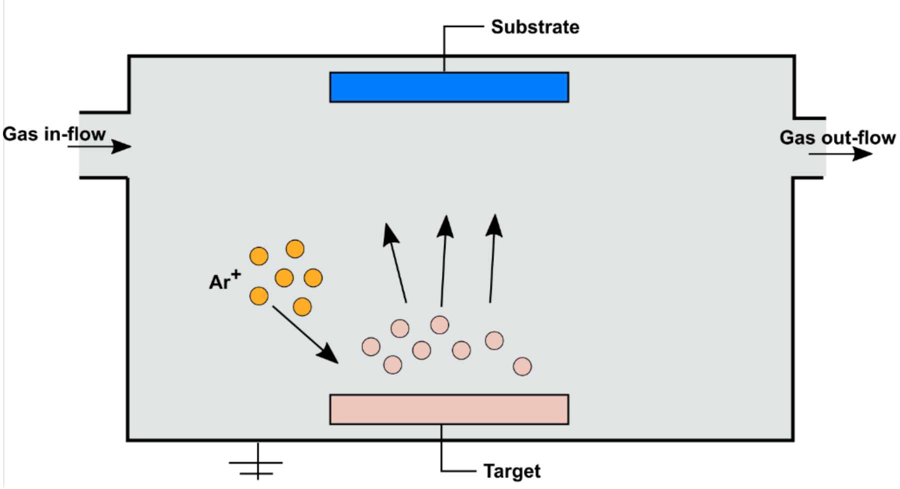

Figure 2.7. Schematics of sputtering method for the synthesis of 1D nanomaterials. Reproduced with permission from [47]

The RF power, deposition time, distance between the target and substrate, and substrate temperature play an important role in the synthesis of nanostructures by this method. To achieve homogenous distribution of temperature on the surface of the substrate, a conducting carbon tape is also deposited on the back of the substrate. Sputtering methods have been used to synthesize 1D nanostructures of various materials including Cu [48], Ni [48], WC [48], Bi [49] as well as oxides such as ZnO [50] and Bi_2O_3 [51]. This method yields very homogenous nanostructures with good control over surface morphology and shape. 1D Cu and Ni nanostructures in the form of nanorods synthesized by sputtering are shown in Figure 2.8. The degree of homogeneity in the size distribution of nanostructures obtained from sputtering is clearly visible in Figure 2.8.

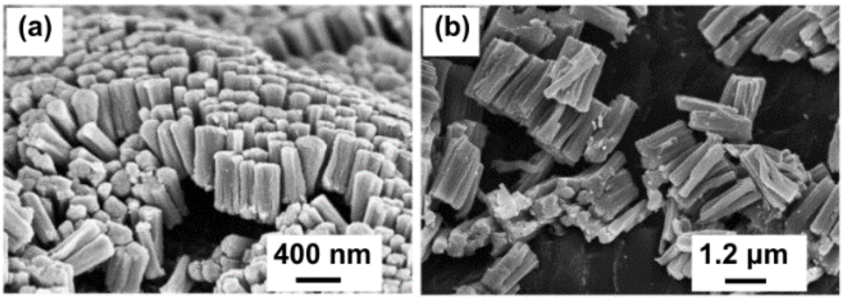

Figure 2.8. SEM images of (a) Cu and (b) Ni nanorods synthesized by sputtering method. Reprinted with permission from [48]

2.5.1.3 Laser ablation

The synthesis of nanomaterials using laser ablation involves the irradiation of the target material with the help of a laser beam. The laser beam penetrates into the surface of the target material with a penetration depth dependent on the power of the laser beam and refractive index of the target. The incident laser causes the removal of electrons from the target material which oscillate in the electromagnetic field of laser. The collision of free electrons with the material atoms causes an increase in the temperature which in turns vaporizes the bulk material. The vapors of the bulk material are transported by a carrier gas such as Ar, N_2 or O_2 and are deposited at the substrate which has a rather lower temperature. Usually a tube furnace is used for laser ablation technique. Schematics of laser ablation method employing a tube furnace for the synthesis of 1D nanostructures is shown in Figure 2.9.

Laser ablation method has been widely used for the synthesis of 1D nanostructures and has been applied to a wide range of materials which includes MgO [52], SnO_2 [53], ZnO [54] and mixed structures such as SiC [55] and GaN [56]. Different types of 1D nanostructures in the form of nanowires [52], nanorods [54] and nanoribbons [53] have been prepared using laser ablation technique.

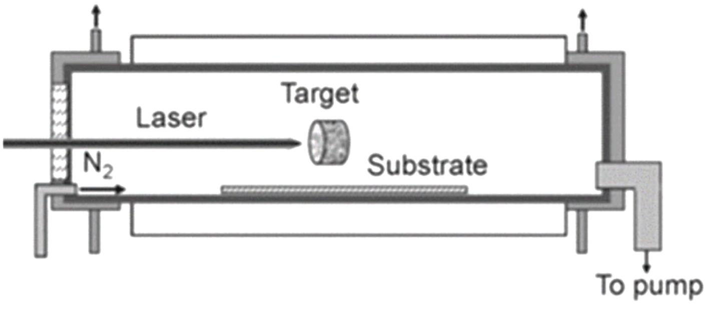

Figure 2.9. Schematics of laser ablation technique for the synthesis of 1D nanostructures. Reprinted with permission from [57]

2.5.1.4 Lithography

Lithography technique for the synthesis of 1D nanostructures has been used for many years. But the cost intensive processing and instrumentation involved in this method are the limiting factors of this technique. There are many types of lithography methods which have been used for the synthesis of nanomaterials and only few of them are discussed in the following sections.

2.5.1.4.1 Colloidal lithography

The colloidal lithography or nano-sphere lithography has been used to fabricate nano-arrays on the substrates for device fabrication [58]. The fabrication of nanostructures by this technique usually involves three steps: i) deposition of spheres, ii) reactive ion etching (RIE) of the spheres and iii) deep RIE of nanostructures (Figure 2.10). Spheres composed of polystyrene are used for this method, which are deposited on the substrate by spin coating. The highly dense spheres are subjected to RIE by oxygen plasma which reduces the size of the spheres and increase the distance between them. The final step involves deep RIE of the intermediate region between spheres leading to fabrication of arrays of nano-pillars. The advantages of this method are the ease in controlling the density and size of nano-pillars by simply tuning the etching conditions. An example of such is shown in Figure 2.11 where the influence of oxygen plasma etching on the size of polystyrene spheres and the size of resulting nanostructures is illustrated. The increase in oxygen plasma etching reduced the diameter of polystyrene spheres which lead to decrease in the diameter of etched silicon nanostructures.

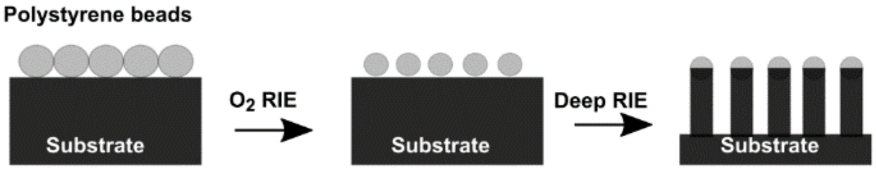

Figure 2.10. Schematics of colloidal lithography for the synthesis of 1D nanostructures. Reproduced with permission from [59]

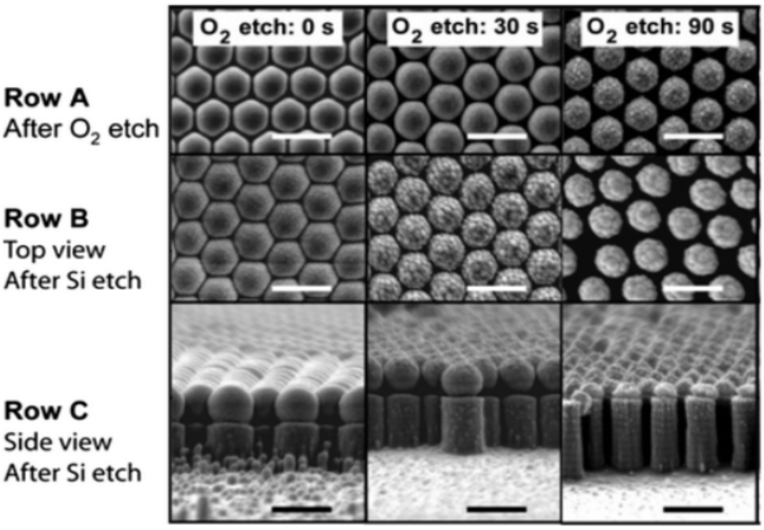

Figure 2.11. SEM images showing nano-spheres on the substrate. Row A & B show top view of nano-spheres after oxygen plasma etching and Si etching, Row C show side view of etched nanostructures. The scale bars are 750 nm. Reprinted with permission from [59]

2.5.1.4.2 Electron beam lithography

Electron beam lithographic technique has the ability to generate nanoscale architectures at the surface. Synthesis of nanostructures by electron beam lithography involves the benefit of using wet chemistry and lithography. An electron beam resist is first deposited at the surface of the substrate. Various types of electron beam resists have been employed for this purpose which includes methylmethacrylate (MMA), poly(methylmethacrylate) (PMMA) and poly(methyl 2-methylpropenoate). After coating the substrate with polymer resist, the desired patterns are generated using electron beam (Figure 2.12a-b). The oxygen plasma treatment of the generated patterns is performed after electron lithography. The plasma treatment removes remaining residues of the polymer resist in the patterns and makes them hydrophilic in nature (Figure 2.12c). Plasma treatment is followed by spin coating the substrate with precursor solution. Rinsing of the precursor coated substrate in acetone is performed to dissolve the polymer resist and generate nanostructures of the precursor at the surface (Figure 2.12d-f).

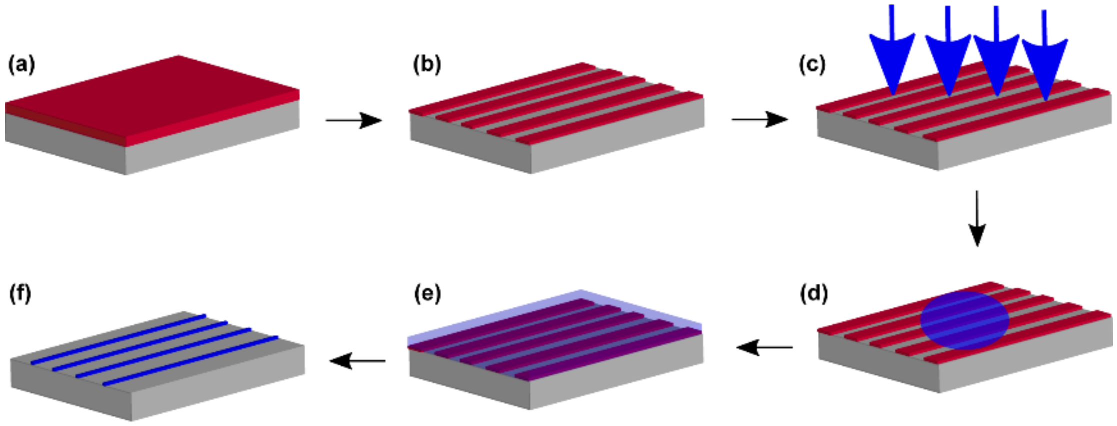

Figure 2.12. Schematics of electron beam lithography, (a) coating of substrate with electron beam resist, (b) generation of patterns using electron beam, (c) oxygen plasma treatment, (d) spin coating with precursor solution, (e) drying of the coated substrate, (f) removal of electron beam resist by rinsing in acetone. Reproduced with permission from [60]

Electron beam lithography has been applied to fabricate 1D nanostructures of various materials such as Pt [61], ZnO [60] [62] and $BiFeO_3$ [62]. It is not only possible to have control over the density and location of the nanostructures at the substrate, but electron beam lithography is also capable of generating structures in different forms. An example of bead type ZnO nanostructures and straight Pt nanowire prepared by electron beam lithography is presented in Figure 2.13.

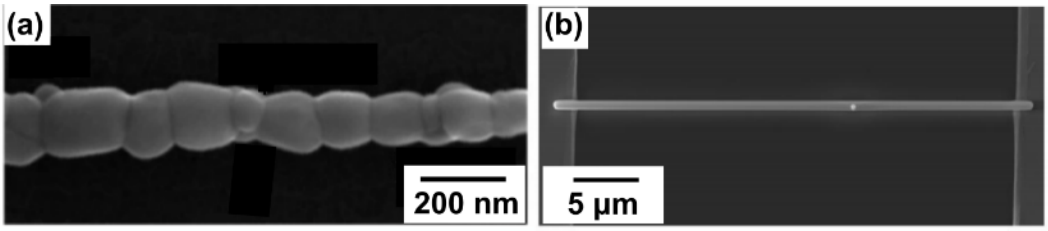

Figure 2.13. SEM images of (a) bead type ZnO nanostructures, (b) Pt nanowire synthesized by electron beam lithography. Printed with permission from [62] [61]

2.5.1.5 Confined growth

The growth of 1D nanostructures using confined growth involves the application of templates which direct the growth of material. Confined growth includes various types of synthesis methods which employ either a template, capping agents or surfactant molecules which determine the shape of the growing material. Template assisted growth usually involves porous plates with long nano-sized channels which direct the growth of material. Anodic aluminum oxide is an example of such template which has been used to synthesize metal and metal oxide 1D nanostructures. SEM image of such a porous anodic aluminum oxide template is shown in Figure 2.14. This template offers long array of porous channels which are more than 100 nm in length and less than 100 nm in diameter. The long porous channels direct vertical growth of 1D nanostructures. An example of the growth of 1D nanostructure in the porous channels of anodic aluminum oxide is illustrated in Figure 2.15. 1D nanostructures of Carbon [63], PbO_2 [64], $PbTiO_3$ [64], and $BaTiO_3$ [64] have been synthesized using template assisted growth.

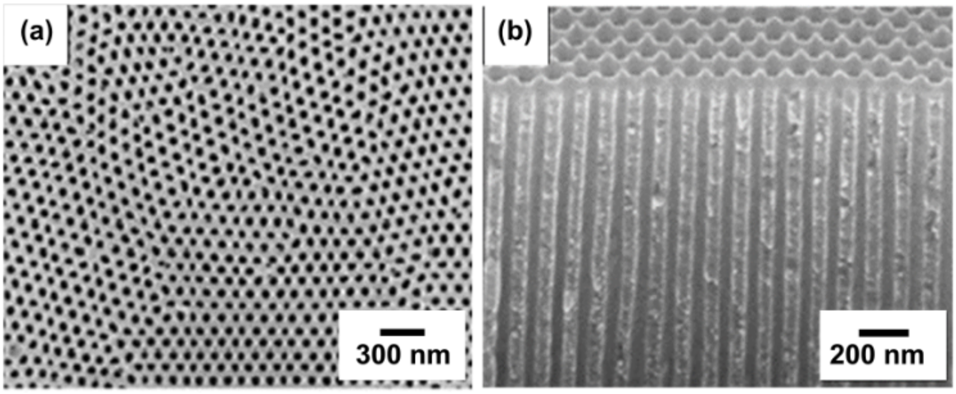

Figure 2.14. SEM images of (a) top and (b) cross-sectional view of anodic aluminum oxide template. Printed with permission from [64]

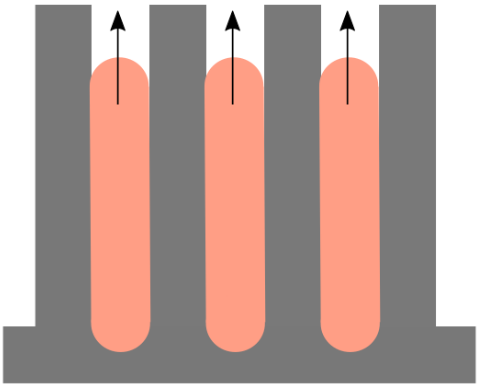

Figure 2.15. The growth of 1D nanostructures in the pores of anodic aluminum oxide. Reproduced with permission from [41]

In addition to templates, the growth of 1D nanostructures using capping agents or surfactant molecules has also been widely reported for the synthesis of range of materials such as ZnO [65], SnO_2 [66], NiO [67], PbO_2 [30] and CeO_2 [68]. In this type of growth surfactant molecules adsorb at the surface of the growing structure in a micelle manner (Figure 2.16) leading to 1D growth. Other than surfactants and capping agents, the use of biological organisms such as viruses [69] has also been reported to yield 1D growth.

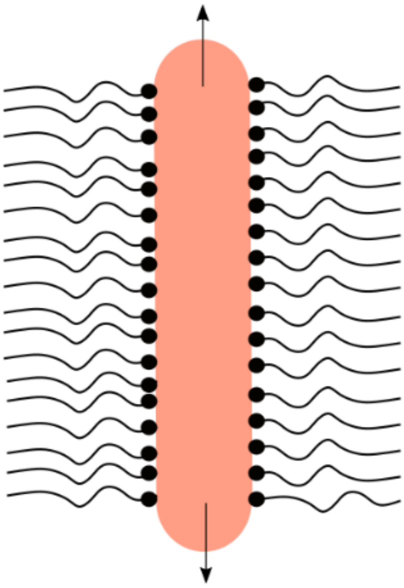

Figure 2.16. The growth of 1D nanostructures directed by surfactant molecules. The arrows show the growth direction. Reproduced with permission from [41]

2.5.2 Chemical deposition method

As the name suggests, chemical deposition method involves chemical reactions of reactive gases and volatile precursors at various values of temperature and pressure for the synthesis of 1D nanostructures. There are many type of chemical deposition methods and only few of them are discussed in the following section.

2.5.2.1 Microwave plasma chemical vapor deposition

Schematics of microwave plasma chemical vapor deposition (CVD) method are shown in Figure 2.17. Typically, a quartz tube furnace is used for the synthesis purpose which is provide with the inlet and outlet for the reactive gases. The microwaves generate the plasma from the gas and deposit the nanomaterial at the sample holder. CVD using plasma has been often used for the synthesis of 1D metal oxide nanostructures [70] [71] [72], but this technique has also been used for the synthesis of carbon nanotubes [73] [74].

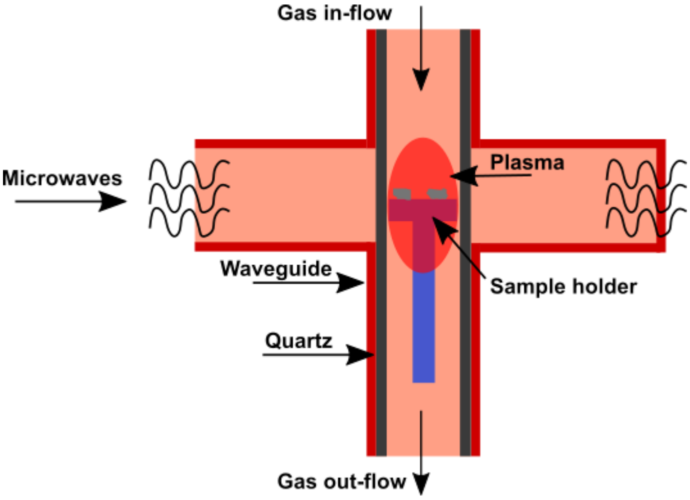

Figure 2.17. Schematics of microwave plasma CVD method. Reproduced with permission from [41]

2.5.2.2 Hot filament chemical vapor deposition

In the hot filament chemical vapor deposition (HFCVD), the filaments are heated by resistive heating which increases the temperature inside the reaction chamber and causes the dissociation of precursor gases (Figure 2.18). The deposition of the nanostructures occurs at the substrate (Si wafer in this case). Different metal nanostructures such as Si [75], SiC [76], and metal oxides nanostructures such as WO_3 [77], MoO_3 [78] and $NiMoO_4$ [79] have been synthesized by HFCVD. A method similar to HFCVD which is specially used for the synthesis of metal oxides is called hot filament metal oxide chemical vapor deposition (HFMOCVD). The major difference in these two types of syntheses is the role of hot filament, in HFMOCVD the hot filament does not only provide a source of heating but also becomes part of the reaction mixture. When the hot filament is heated at a high temperature the surface atoms of the filament vaporize and become part of the reaction mixture. Due to this reason the reactive precursor gases are not required in HFMOCVD.

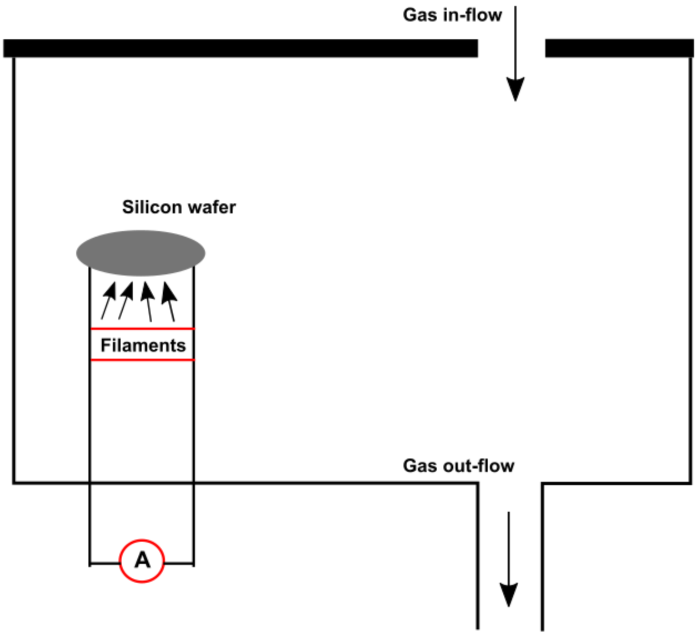

Figure 2.18. Schematics of HFCVD process. Reproduced with permission from [41]

Synthesis of nanostructures using CVD has many advantages which combine: i) the ability to coat large surface area of substrate, ii) good control over the size, shape and morphology of the synthesized nanostructures. But there are some serious drawbacks associated with CVD in general such as i) application of high deposition temperature, ii) possibility of chemical impurities, iii) sophisticated instrumentation making the process cost intensive, and iv) difficulties of synthesizing doped nanostructures (mixed structures by using two different type of precursors).

2.5.2.3 Room temperature chemical vapor deposition

The problems associated with conventional CVD processes are resolved by using the room temperature chemical vapor deposition method. This method was reported more than a decade ago by Prof. Seeger's group to synthesize 1D nanostructures of silicone using ambient conditions [1]. The advantages of this method do not only include the room temperature processing but also ambient pressure conditions and the use of less complicated instrumentation. The synthesis is carried out in a modified desiccator which is normally used for the storage of samples in inert conditions. The pre-cleaned and activated substrates are placed in the coating chamber (desiccator) which is connected to the supply of nitrogen. The cleaning of substrates is performed to remove the presence of impurities and oxygen plasma activation is carried out to create hydroxyl (-OH) groups at the surface. The relative humidity inside the coating chamber is adjusted by tuning the flow of nitrogen which is in fact the mixture of dry and humidified nitrogen gas. The precursors are injected from the top septum and vaporization of the precursor leads to the growth of 1D nanostructures on the surface of the substrate. The schematics of such room temperature CVD process are shown in Figure 2.19.

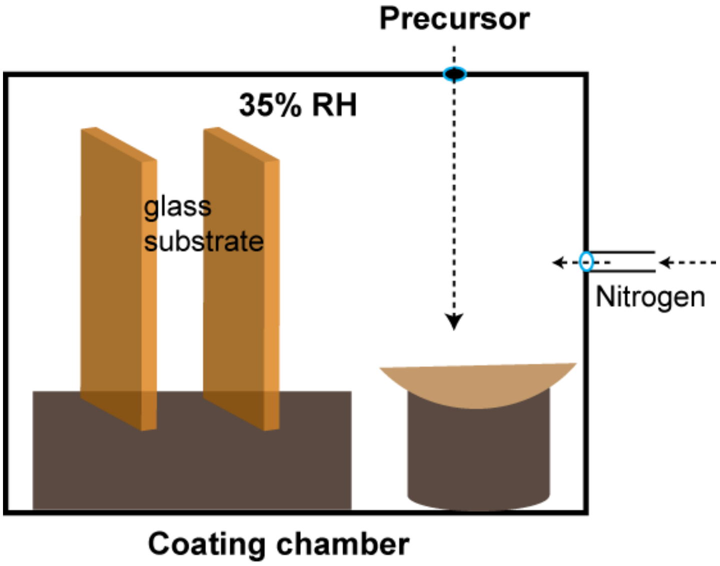

Figure 2.19. Schematics of room temperature CVD process. Reproduced with permission from [80]

This room temperature CVD process has been extensively used to synthesize 1D nanostructures of silicone called silicone nanofilaments (SNFs). The synthesized SNFs showed remarkable change in the surface properties of the substrate materials. The substrates coated with SNFs showed perfect transparency and excellent water repellent properties (Figure 2.20a). The presence of highly entangled SNFs on a glass substrate after room temperature CVD method is shown in Figure 2.20b.

Figure 2.20. (a) Formation of spherical water droplets on glass substrate after the synthesis of SNFs, (b) SEM images of corresponding SNFs structures. Reprinted with permission from [5]

The synthesis of 1D SNFs is not only possible on glass substrates but many other technologically important substrates could be coated with SNFs. Figure 2.21 & Figure 2.22 shows the SEM images of Si, cotton, aluminum, PDMS and various fibrous substrates coated with SNFs, while the insets show the water droplets on corresponding substrates.

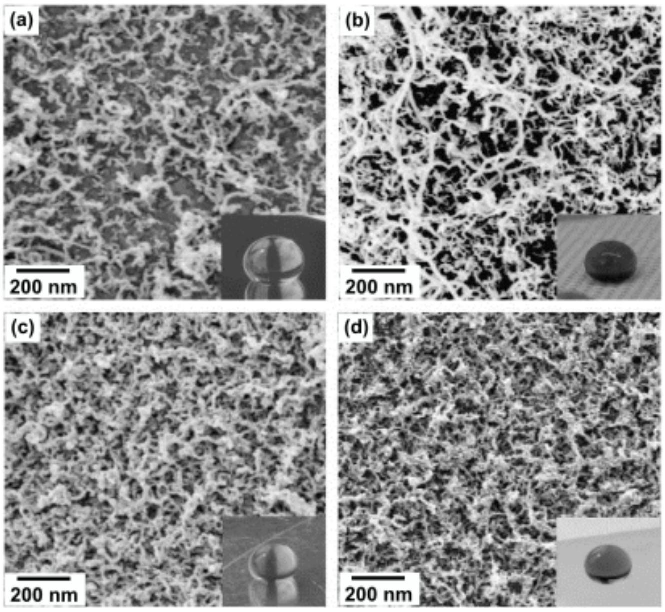

Figure 2.21. SEM images of (a) silicon, (b) cotton, (c) aluminum, and (d) PDMS substrate coated with SNFs. Insets shows photographs of water on corresponding substrates. Reprinted with permission from [5]

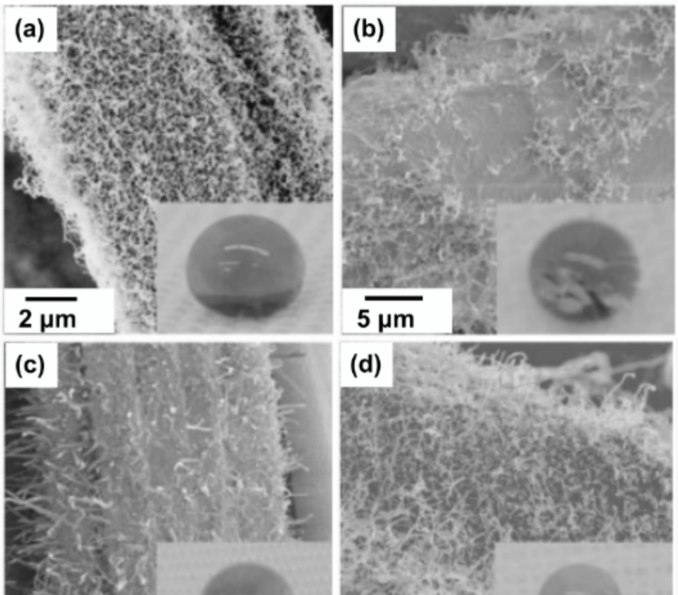

Figure 2.22. SEM images of (a) cotton, (b) wool, (c) acetate, and (d) PET fibers coated with SNFs. Insets show photographs of water on corresponding substrates. Reprinted with permission from [6]

In addition to the already mentioned substrate materials, room temperature CVD method has also been successfully applied to grow SNFs on various other materials to impart wetting or anti-wetting properties. The other coated materials include silk [6], viscose [6], polyacrylonitrile [6], polyethylene, Kevlar® [81], wood [1] and titanium [82]. In addition, this process has also been up-scaled [3] to coat large substrates for industrial applications.

Room temperature CVD process is not only limited to nanofilament structures but has also been extended to synthesize other structures such as nanotubes. By tuning the relative humidity inside the coating chamber highly dense siloxane nanotubes were synthesized by Stojanovic et al [83] (Figure 2.23).

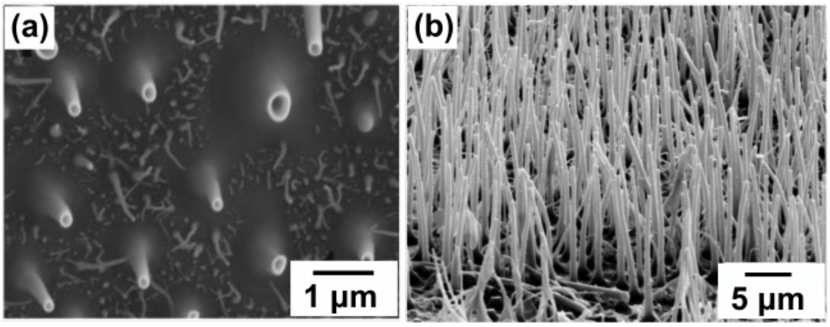

Figure 2.23. SEM images of siloxane nanotubes (a) top view, and (b) cross-sectional view. Reprinted with permission from [83]

As mentioned previously the relative humidity inside the coating chamber plays an important role in determining the shape of the silicone nanostructures. Artus et al [84] described the synthesis of silicone nanostructures in various shapes and forms by controlling the reaction conditions. Silicone nanostructures were synthesized in different 1D forms as well as complex shapes. Figure 2.24 shows the SEM images of silicone nanostructures reported by Artus et al [84]. 1D silicone structures in the form of filaments, tubes, rods, chalices and complex shapes such as stars, helices, volcanoes and chalice on top of volcanoes were synthesized by varying humidity, temperature and surface chemistry. The different process parameters to synthesize various type of silicone structures are represented in Figure 2.25. Around room temperature or below, SNFs were obtained while at low humidity (Figure 2.24d), while at high humidity levels volcanoes type structures were observed (Figure 2.24e). At intermediate conditions mixed structures were observed. Around 57% relative humidity at 35^{o}C filament types structures on top of volcanoes were observed (Figure 2.24f). At relative humidity 60%-80% and 20^{o}C-50^{o}C rod like structures were observed (Figure 2.24g). At high levels of humidity from 80% or above and 25°C-35°C chalice type structures were obtained (Figure 2.24h & i).

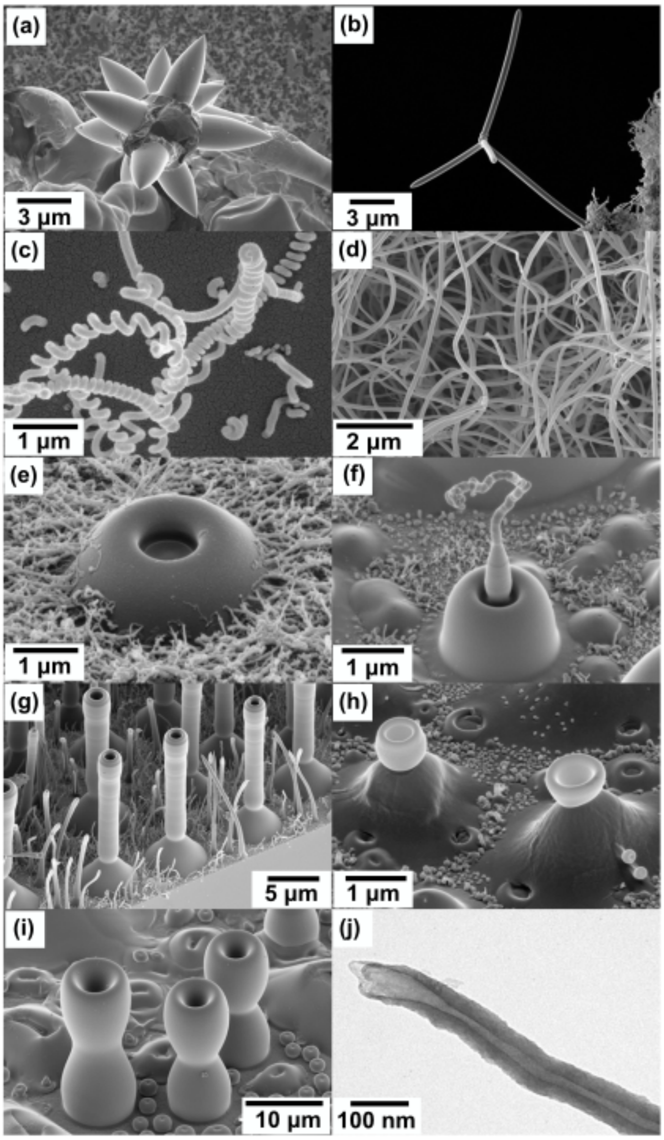

Figure 2.24. SEM images of silicone nanostructures, (a-b) stars, (c) helices, (d) SNFs, (e) volcanoes, (f) filament, (g) rod, (h) chalice on the top of a volcano, (i) chalices and (j) TEM image of tubes. Reprinted with permission from [84]

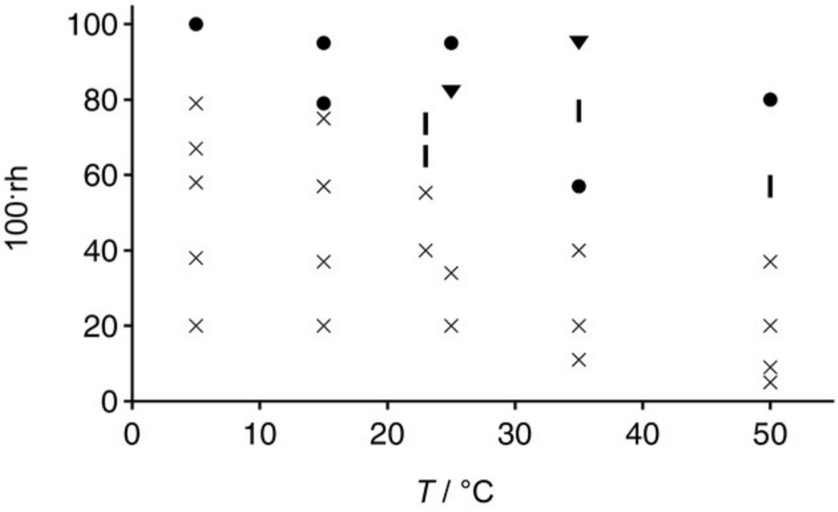

Figure 2.25. The relation of relative humidity and temperature for the synthesis of silicone nano and micro structures using chemical vapor deposition, × SNFs; ● volcanoes; | rods; ▾ chalices. Reprinted with permission from [84]

The in situ shaping of objects with a precise control over the morphology is a step forward in the synthesis of nanomaterials, and it also highlights the significance of this synthesis technique.

2.6 The growth mechanisms

As described in previous sections, there are many physical and chemical methods used for the synthesis of 1D nanostructures. The growth mechanisms which govern the synthesis of such 1D nanostructures are discussed in this section. The growth mechanisms discussed in this section usually involve the interaction of atoms or molecules, growth and assembly of such atoms and nuclei to form 1D nanostructures. The nuclei play a vital role in the growth of nanostructures as they act as seeds for the further growth. The size, shape and number density of such nuclei determine the shape of growing material at nanoscale. Depending on the type of interactions, nucleation, growth of nuclei and assembly, growth mechanisms are classified into i) vapor liquid solid (VLS), ii) vapor solid (VS) and iii) solution liquid solid (SLS) mechanisms. In addition to the above-mentioned growth mechanisms, we also discuss a new growth mechanism called droplet assisted growth and shaping (DAGS).

2.6.1 Vapor liquid solid growth mechanism

VLS growth mechanism is the most known growth mechanism for the synthesis of nanomaterials since 1964 [85]. This growth mechanism has been applied extensively on a range of materials for the synthesis of 1D nanostructures. The schematics of VLS growth mechanism are shown in Figure 2.26. This growth mechanism involves the use of metal particles which act as catalyst seed for the synthesis of 1D nanostructures (Figure 2.26a). Usually the high temperature at which the synthesis is carried out, the metal particles melt due to their high surface to volume ratio. The melts of the particles react with the reactive precursor molecules to form eutectic alloys (Figure 2.26b). The alloys are formed due to the dissolution of reactive precursor molecules into the liquid metals. Due to continuous supply of precursor molecules, saturation of precursor solutes in liquid alloys occur which leads to precipitation of solid phase out of the liquid alloys (Figure 2.26c-d). As this mechanism involves formation of liquid alloys of metal particles, that is why the choice of metal catalyst particles play an important role in determining the final shape, size and morphology of grown 1D nanostructures.

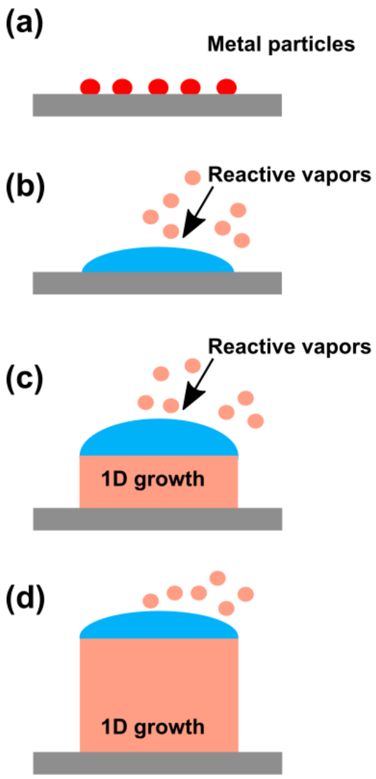

Figure 2.26. Schematics of VLS growth mechanism, (a) catalyst metal particles act as seeds (b) formation of liquid alloys, (c-d) growth of 1D nanostructure from the alloys after saturation. Reprinted with permission from [41]

2.6.2 Vapor solid growth mechanism

The vapor solid (VS) growth mechanism does not involve application of metal catalyst particles for the growth of 1D nanostructures. Due to the absence of liquid metal particles, only two phases are involved in VS growth mechanism i.e. vapor and solid. VS growth mechanism is a self-catalytic method where solid in the form of 1D grows from the supply of active precursor vapors. The schematics of VS growth are illustrated in Figure 2.27. The 1D growth according to VS mechanism occurs in the following steps: i) vaporization of metal precursor or sublimation of the hot filament (Figure 2.27a), ii) reaction of metal vapors with oxygen gas (Figure 2.27b), iii) condensation of metal oxide vapors on the substrate surface (Figure 2.27c), iv) and anisotropic growth (Figure 2.27d). The VS growth mechanism represented in Figure 2.27 is typically applied to explain the growth of 1D metal oxide nanostructures [86] [87] [88]. But VS growth mechanism has also been applied for the synthesis of pure metal 1D nanostructures [89]. In the case of metal 1D nanostructures, the oxygen gas is replaced by inert carrier gas such as argon or nitrogen and 1D growth occurs in the following steps: i) vaporization of metal precursor or sublimation of hot filament, ii) condensation of metal vapors on the substrate surface and iii) anisotropic growth of 1D metal nanostructures.

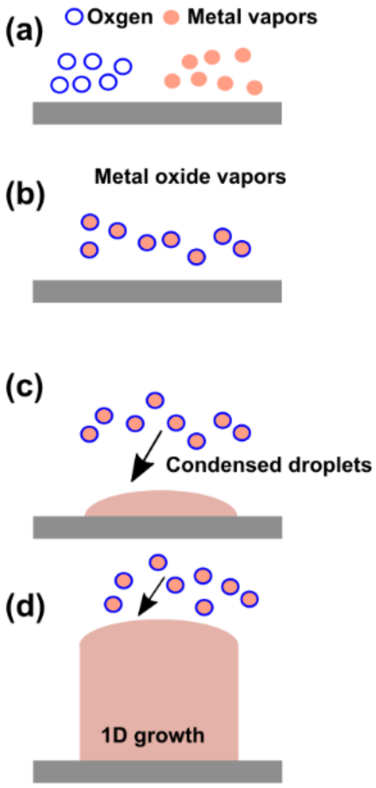

Figure 2.27. Schematics of VS growth mechanism, (a) vaporization of metal precursor (b) reaction of metal vapors with oxygen, (c) condensation of formed metal oxide vapors, (d) growth of 1D metal oxide nanostructure. Reprinted with permission from [41]

2.6.3 Solution liquid solid growth mechanism

The solution liquid solid (SLS) growth mechanism is very similar to VLS growth mechanism. Here, the system is entirely submerged in a solution. The metal catalyst particles play an important role in SLS growth mechanism. The metal precursors are provided from the solution phase which dissolve in the metal particles to form eutectic alloys. When the saturation of the solute (metal precursor) in eutectic alloys occur, they precipitate outside the alloys as 1D solid. The size, shape and morphology of the growing 1D nanostructure is dependent on the type of metal particles used. The schematics of SLS growth mechanism are shown in Figure 2.28. SLS mechanism has been successfully applied to synthesize 1D nanostructures of semiconductors and metal oxides. Usually SLS mechanism is applied for the synthesis of 1D nanostructures in solution phase including sol-gel technique [90].

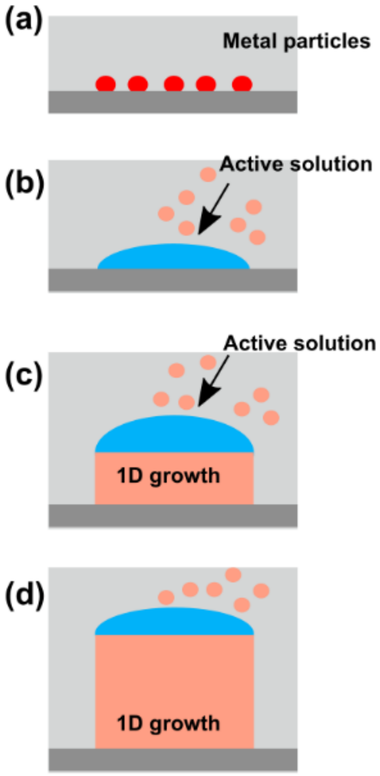

Figure 2.28. Schematics of SLS growth mechanism, SLS system submerged in solution (highlighted in light grey), (a) catalyst metal particles act as seeds (b) formation of liquid alloys, (c-d) growth of 1D nanostructure from the alloys after saturation. Reprinted with permission from [41]

2.6.4 Droplet assisted growth and shaping mechanism

The droplet assisted growth and shaping (DAGS) growth mechanism has been developed by the Seeger group and is rather new compared to the conventionally known growth mechanisms for the synthesis of 1D nanostructures. The DAGS growth mechanism was used for the first time in 2003 [91] to synthesize 1D silicone nanostructures called silicone nanofilaments [1]. Since then DAGS growth method has been applied to synthesize various forms of 1D silicone nanostructures. Unlike other methods, it does not involve thermal evaporation of precursors and/or metal catalyst particles to direct 1D growth, instead it utilizes facile processing combining room temperature processing and polymerization reactions of precursors. The advantage of DAGS growth is the ability to carry out the synthesis at room temperature and it depends on the vaporization of volatile reactive precursors. DAGS growth mechanism relies on the formation of nano-water droplets at the surface of the substrates in humid atmosphere and the reaction of precursors inside the droplets to yield 1D growth. The formation of water droplets at the surface of the substrates occurs due to the presence of structural and chemical inhomogeneity [92] [93]. Due to the presence such effects, water droplets in the form of islands form at the surface (Figure 2.29a). These water droplets act as confined reaction vessels where reaction of the precursor vapors with water occur [84]. Figure 2.29 illustrates DAGS growth mechanism for the synthesis of 1D silicone nanostructures. For the synthesis of 1D silicone nanostructures, alkylchlorosilanes are used. The hydrolysis of the precursor vapors leads to the formation of HCl and silanol (Figure 2.29b). The as produced HCl acts as catalyst for the further hydrolysis and condensation reactions of precursor molecules (Figure 2.29c). The water molecules are constantly supplied from the humid atmosphere to sustain hydrolysis and condensation reactions. When the saturation of the products of hydrolysis and condensation reactions occur, they are deposited as a solid outside of the water droplet (Figure 2.29d). By changing the humidity and the surface wetting, the formation of water droplets can be tuned to synthesize various shapes of 1D nanostructures. Artus et al [84] reported the synthesis of various 1D and complex silicone nanostructures by manipulating such conditions. The DAGS growth mechanism is a very smart method for the synthesis of nanomaterials at room temperature.

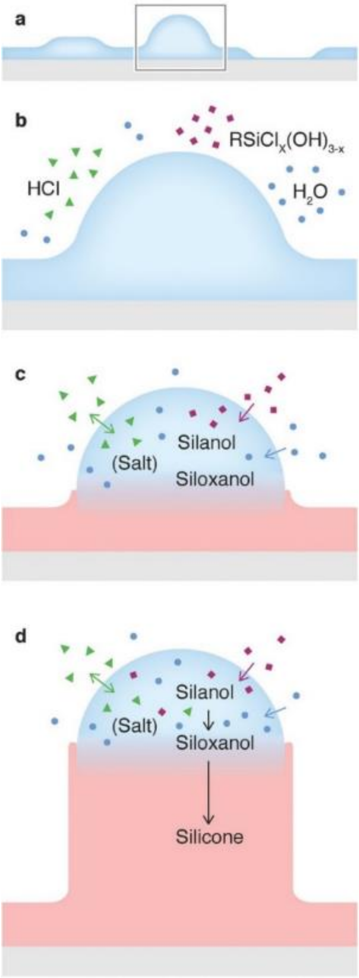

Figure 2.29. DAGS growth mechanism, (a) formation of water droplets at the surface, (b) reaction of precursor vapors with water droplet, (c) formation of products as a result of hydrolysis and condensation reactions, (d) growth of 1D nanostructures. Reprinted with permission from [84]

3. Materials and Methods

3.1 Chemicals

Table 3.1 List of Chemicals (in alphabetical order)

Chemicals	Quality	Supplier
Aceton	technical grade	Sigma Aldrich
3-aminopropyltriethoxysilane	99%	Sigma Aldrich
Calcium chloride	99.9%	Sigma Aldrich
2-(carbomethoxy)ethyltrichlorosilane	95%	ABCR GmbH
Carbon nanofibers	graphitized	Sigma Aldrich
Copper sulfate	99.9%	Sigma Aldrich
Deconex® 11 universal	n.a	Borer Chemie AG
Ethanol	92.6-93.8%	Sigma Aldrich
Germanium tetrachloride	99.9%	ABCR GmbH
Hydrochloric acid	32 vol. %	Merck
Milli-Q® water	18.2 MΩ.cm at 25°C	Millipore systems
Magnesium chloride hexahydrate	99%	Sigma Aldrich
Parafilm M®	n.a	Sigma Aldrich
1H, 1H, 2H, 2H-perfluorodecyltriethoxysilane	97%	Sigma Aldrich
Phenyltrichlorogermane	95%	ABCR GmbH
Phosphate buffer	n.a	Sigma Aldrich
Potassium chloride	99%	Sigma Aldrich
Potassium phosphate dibasic	99%	Sigma Aldrich
Sodium bicarbonate	99.7%	Sigma Aldrich
Sodium chloride	98%	Sigma Aldrich
Sodium hydroxide	97%	Sigma Aldrich

Sodium sulfate	99%	Sigma Aldrich
Toluene extra dry	99.8%	Sigma Aldrich
Trichloroethylsilane	98%	ABCR GmbH
Trichloromethylsilane	99%	Sigma Aldrich
Triethylaluminum	1 M solution in hexane	Sigma Aldrich
Trimethylaluminum	2 M solution in toluene	Sigma Aldrich
Tris-hydroxymethyl amminomethane	99.8%	Sigma Aldrich

3.2 Substrates

Table 3.2 List of substrates (in alphabetical order)

Substrate type	Specifications	Supplier
Germanium wafers	<100>, (10 mm x 10 mm), un-doped, single side polished	Crystec GmbH
Glass slides	(26 mm x 76 mm)	Menzel Gläser
Silicon wafers	<100>, (10 mm x 10 mm), un-doped, single side polished	Crystec GmbH

3.3 Synthesis of silicone nanofilaments

3.3.1 Cleaning and surface activation of substrates

A precondition for the good coating is cleanliness of the substrate therefore surface of the substrate should be free of any dust particles or any impurities. In the field of coatings or thin films cleaning of the substrate prior to deposition is essential. In some cases, deposition is carried out in clean room to avoid any contact with dirt particles or impurities. However, for the synthesis of silicone nanofilaments (SNFs) such measures are not necessary, even a minimal cleaning treatment of the substrate is enough to obtain homogenous growth of SNFs over the entire substrate.

The cleaning procedure for the glass substrates was adopted from the literature reported protocol [1]. Glass substrates were immersed in a container filled with 10 vol. % aqueous solution of Deconex® 11 Universal (Borer Chemie AG, Switzerland) and sonicated for 30 minutes at 50°C. Glass substrates were washed with copious amount of Milli-Q® water and dried in the stream of nitrogen. For the growth of SNFs on Si and Ge wafers, cleaning of substrates was performed by immersing in acetone for 30 minutes followed by washing with Milli-Q® water. Surface activation of cleaned glass substrates and wafers was performed in oxygen plasma chamber Femto (Diener Electronic, Nagold Germany) at 100-watt power (100%) for 10 minutes.

3.3.2 Chemical vapor deposition

Synthesis of SNFs was performed by chemical vapor deposition method in a custom-built coating chamber using literature reported protocol [1]. The schematics of the coating setup are show in Figure 3.1. The setup for the synthesis of SNFs is comprised of two units: (a) the coating chamber, (b) humidity adjuster to prepare the gas mixture. Vacuum desiccator (Schott DURAN) was used as coating chamber for the deposition. The desiccator was provided with an inlet and outlet valve to control the gas flow inside the coating chamber. A perforated ceramic plate was placed inside the desiccator which acts as a platform for the sample holder and silane vial holder. The humidity adjuster consisted of a custom built mixing chamber with an inlet for dry and humidified nitrogen. Humidified nitrogen was generated by flushing dry nitrogen into a bottle filled with Milli-Q® water. The ratio of dry and humidified nitrogen was adjusted with the help of flow meters to regulate the humidity of the gas mixture. The humidity and temperature of the gas mixture was measured by EE23 hygrometer (E+E Elektronik).

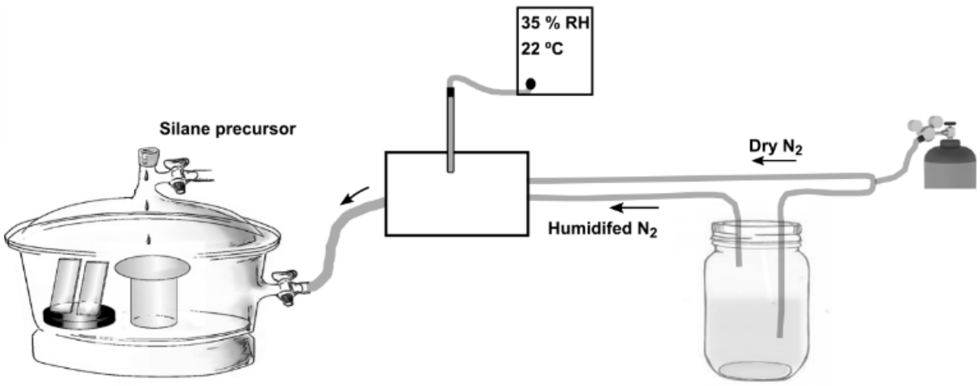

Figure 3.1. Setup for the synthesis of SNFs

Synthesis of SNFs was performed using two different silane precursors with slightly different conditions named as protocol I and protocol II.

3.3.2.1 Protocol I

In protocol I the following procedure was adopted for the synthesis of SNFs:

i. Placing the pre-cleaned and activated substrates inside the coating chamber.
ii. Adjusting the humidity of the coating chamber by controlling co-flow of dry and humidified nitrogen at the value of ~35% RH.
iii. Flushing the coating chamber for 1 hour with the gas mixture (dry + humidified nitrogen).
iv. Isolating the coating chamber by closing the inlet and outlet valves.
v. Introducing trichloromethylsilane (TCMS, 500 µL, 4.24 mmol) into the coating chamber from top septum.
vi. Reaction carried out at room temperature (20-22°C) for overnight.
vii. Flushing the coating chamber with dry nitrogen to remove HCl.
viii. Opening the coating chamber.
ix. Washing the substrates with deionized water.

3.3.2.2 Protocol II

In protocol II the following procedure was adopted for the synthesis of SNFs:

i. Placing the pre-cleaned and activated substrates inside the coating chamber.
ii. Adjusting the humidity of the coating chamber by controlling co-flow of dry and humidified nitrogen at the value of ~35% ± 2% RH.
iii. Flushing the coating chamber for 1 hour with the gas mixture (dry + humidified nitrogen).
iv. Isolating the coating chamber by closing the inlet and outlet valves.
v. Introducing trichloroethylsilane (TCES, 500 µL, 3.8 mmol) into the coating chamber from top septum.
vi. Reaction carried out at room temperature (21-22°C) for 4 hours.
vii. Flushing the coating chamber with dry nitrogen to remove HCl.
viii. Opening the coating chamber.

ix. Washing the substrates with deionized water.

3.4 Hydroxyapatite biomineralization

3.4.1 Functionalization of SNFs

The glass substrates were coated with SNFs using protocol I. SNFs coated glass substrates were introduced into the oxygen plasma chamber Femto (Diener Electronic, Nagold Germany), and subjected to oxygen plasma generated at 100-watt power for duration of 2 minutes. Oxygen plasma activated SNFs were functionalized with amino and carboxyl groups. 3-aminopropyltriethoxysilane (3-APTES) (Sigma Aldrich) was used for amine while 2-(carbomethoxy)ethyltrichlorosilane (2-CETS) (ABCR GmbH) was used for carboxyl functionalization.

Plasma activated substrates were immersed in extra dry toluene (Sigma Aldrich) and 3-APTES (200 µL, 0.85 mmol) was introduced into the reaction chamber. Functionalization was performed 4 hours. Functionalization of substrates with carboxyl groups was achieved by immersing the substrates in extra dry toluene with 2-CETS (200 µL, 1.19 mmol) for 4 hours followed by ester hydrolysis in 50 mmol phosphate buffer. All functionalized substrates were dried in nitrogen stream and stored at ambient conditions.

3.4.2 Preparation of simulated body fluid

To study the biomineralization of hydroxyapatite (HA), the functionalized substrates were dipped into simulated body fluid (SBF) which had the same composition and concentration of salts as compared to the human blood plasma. 1.5 SBF was used for all studies with the composition described in the Table 3.3. The SBF was prepared by dissolving NaCl, $NaHCO_3$, KCl, K_2HPO_4, $MgCl_2.6H_2O$, $CaCl_2$ and Na_2SO_4 in Milli-Q® water. The buffer solution was prepared by tris-hydroxymethylamminomethane. To adjust the pH 1M HCl was used and pH of SBF was maintained at 7.4. The substrates with the dimensions 10 mm x 10 mm were immersed in 50 ml of SBF kept at 37°C.

Table 3.3. Composition of prepared SBF

Ions	Composition (mmol)
Na^+	213
K^+	7.5
Ca^{2+}	3.8
Mg^{2+}	2.3
HCO^-_3	6.3
Cl^-	223
HPO^-_4	1.5
SO^{2-}_4	0.75

3.5 Preparation of superhydrophobic/conductive surfaces by dip coating

Hybrid coatings with superhydrophobic and conductive property were obtained by dip coating SNFs coated glass substrates in carbon nanofibers (CNFs, Sigma Aldrich) suspension. SNFs were synthesized on glass and textile substrates using protocol II. Except for the textile, cleaned samples were dried in the oven overnight at 80° followed by oxygen plasma treatment for 30 minutes. Suspensions were prepared by sonicating (0.1, 0.25, 0.5, 0.75 and 1 wt. %) CNFs in toluene at 30°C for duration of 15-20 minutes. Dip coating of substrates in CNFs suspensions was performed for 5 minutes followed by washing with toluene and Milli-Q® water to remove loosely bound CNFs. Drying of substrates was carried out under the stream of nitrogen to remove volatile compounds.

3.5.1 Preparation of hybrid surfaces with Parafilm addition

The method used was modified procedure of Mates et al [94]. Parafilm-M® (PF, Sigma Aldrich) was dissolved in toluene kept at 50°C under continuous stirring for 30 minutes. Solution of PF was prepared by dissolving 0.125, 0.15, 0.175, 0.2 and 0.225 g of PF in 5 ml of toluene. The solution of PF was added to 1 wt. % CNFs dispersion in toluene to yield (*x* wt. % PF + 1 wt. % CNFs) dispersions, where *x* is equal to 0.5, 0.6, 0.7, 0.8 and 0.9 wt. %. Sonication of final dispersion for 10 minutes at 30°C was performed to obtain a stable dispersion. SNFs coated glass substrates prepared by protocol II were dip coated in the dispersions for 5 minutes followed by washing with copious amounts of toluene and Milli-Q® water. Drying of all substrates was performed under nitrogen stream. Substrates for control experiments were prepared with the same procedure.

3.5.2 Sheet resistance measurement

Sheet resistance of coatings was measured by Interface 1000 potentiostat (GAMRY Instruments, USA) using 4 probe method. A custom-built kit with four equidistant electrodes (5 mm) was used to measure the sheet resistance. The value of current was kept from 50-100 µA. Voltage drop on inner electrodes in response to the current applied on outer electrodes was determined to calculate the sheet resistance using Equation 3.1.

$$R_S = \frac{V}{I} \cdot \frac{\pi}{ln2}$$ Equation 3.1

Where I stands for the current applied at the outer probes, V is the voltage generated at inner probes and R_S donates sheet resistance expressed as Ohm/Square or Ohm/□.

For one sample at least 3 measurements were performed and an average sheet resistance value was used for further calculations.

3.5.3 Environmental durability

The stability of the coatings against humid environment was checked by subjecting the substrates to extreme humid conditions. The substrates were placed in the glass desiccator kept at room temperature (20°C - 22°C) connected to nitrogen gas inlet. Humidified nitrogen was flushed through the glass desiccator and relative humidity was maintained at 90% ± 2%. The humidity and temperature inside the glass desiccator was monitored using EE23 hygrometer (E + E Elektronik).

3.5.4 Chemical durability

The chemical durability of the coatings was tested by immersing the dip coated substrates into aqueous solutions of acidic and basic nature. NaOH and HCl were used to prepare the aqueous solutions of pH 2 and pH 14. The values of pH were controlled using inoLab® benchtop pH meter.

3.5.5 Mechanical durability

The resistance of the coatings to scratch or abrasion was measured by AB5000 Washability Tester (TQC, Netherlands). Abrasion resistance of the coatings was measured using ASTM standard D4213 which is often used to check the abrasion or scrub resistance of paints and coatings. The pressure of 1.86 kPa was applied on a sponge which was moving over the coated substrate with frequency of 5 cycles/minute.

3.6 Synthesis of other nanomaterials by CVD

3.6.1 Synthesis of germanium-based nanomaterials

3.6.1.1 Cleaning and surface activation of substrates

For cleaning purpose glass substrates with dimensions (26 mm x 76 mm) (Menzel Gläser, Germany) were immersed in 10 vol. % aqueous solution of Deconex® 11 Universal (Borer Chemie AG, Switzerland). Sonication of glass substrates at 50°C for 30 minutes was performed followed by washing with Milli-Q® water. After drying the substrates under the nitrogen stream, plasma activation was performed in oxygen plasma chamber Femto (Diener Electronics Nagold, Germany) at 100-Watt (100%) power for duration of 10 minutes.

3.6.1.2 Chemical vapor deposition of germanium oxide nanofilaments (GNFs)

Cleaned and activated glass substrates were placed in the glass desiccator (Schott DURAN), provided with a perforated ceramic plate. The synthesis method was the adaptation of already documented procedure for the synthesis of SNFs [1]. The desiccator was provided with an inlet and outlet valve for the gas flow. Pre-mixed dry and humidified nitrogen gas was flushed through the glass desiccator for 1 hour of equilibrium time. The relative humidity and temperature inside the coating chamber was monitored using EE23 (E + E Elektronik) hygrometer. The relative humidity inside the glass desiccator was maintained at 35% ± 2%. $GeCl_4$ (ABCR GmbH) with an amount of (8.7 mmol, 1 mL) was introduced inside the glass desiccator with a syringe. Reaction was carried out for overnight (~12 hours) at room temperature (~20°C - 22°C).

3.6.1.3 Annealing

Annealing of the GNFs was performed in air using muffle furnace (Carbolite). All coated substrates were heated at 300°C, 400°C, 500°C and 600°C with the heating rate of 10°C/min. Dwell time of 4 hours was used for all substrates followed by cooling inside the furnace.

3.6.1.4 Treatment with silanes

Functionalization of GNFs with silane molecules was performed. For this purpose, surface activation of GNFs was carried out using oxygen plasma chamber Femto (Diener Electronics Nagold, Germany). GNFs were subjected to plasma generated at 100-watt power for 5 minutes with oxygen flow rate of 20 sccm. Activated substrates were placed in anhydrous toluene (water ppm <30) and TCMS (100 µL, 0.8 mmoles) was introduced into the reaction chamber. Reaction was carried out for the duration of 4 hours followed by cleaning of functionalized substrates in toluene and Milli-Q® water. Drying of substrates was performed in nitrogen stream.

3.6.2 Synthesis of alumina-based nanomaterials

3.6.2.1 Cleaning and surface activation of substrates

Silicon wafers with dimension of 10 mm x 10 mm were used as substrate. To remove the organic impurities from the surface wafers were immersed in acetone for 30 minutes followed by washing with Milli-Q® water. Activation of wafers to create hydroxyl (-OH) groups on the surface was carried out in oxygen plasma chamber Femto (Diener Electronics Nagold, Germany) at 100-Watt (100%) power for duration of 10 minutes.

3.6.2.2 Chemical vapor deposition

Pre-cleaned and activated substrates (wafers) were placed in the coating chamber and same coating procedure was repeated which is described in Figure 3.1. In brief, the substrates were placed in the glass desiccator which was supplied with an inlet and outlet valve for the gas flow. The relative humidity inside the glass desiccator was adjusted by co-flow of dry and humidified nitrogen gas. The temperature and relative humidity inside the glass desiccator was monitored using EE23 hygrometer (E + E Elektronik). The relative humidity of 35% ± 1% was maintained inside the glass desiccator for 1 hour. The precursor used for the synthesis was 2 M solution of trimethylaluminum (TMA) in toluene. Due to the high sensitivity of TMA towards moisture, it was stored in the glove box with O_2 and H_2O content below 1 ppm. 0.4 mmol of TMA was transferred in an air tight glass vial from the glove box and introduced into the glass desiccator with a syringe. Reaction was carried out for the duration of 4 hours.

3.6.2.3 Annealing

Thermal stability of synthesized nanomaterials was tested by annealing the coated substrates in air using muffle furnace (Carbolite). Substrates were heated at 300°C, 400°C, 500°C and 600°C with the heating rate of 10°C/minute with dwell time of 4 hours. Cooling of the substrates was performed inside the furnace.

3.6.3 Synthesis of mixed alumina-silicone based nanomaterials

3.6.3.1 Cleaning and surface activation of substrates

Silicon wafers with dimension of 10 mm x 10 mm were immersed in acetone for 30 minutes to remove any organic impurities. Washing of wafers with Milli-Q® water was performed followed by plasma activation in oxygen plasma chamber Femto (Diener Electronics Nagold, Germany) at 100-Watt (100%) power for duration of 10 minutes.

3.6.3.2 Chemical vapor deposition

Chemical vapor deposition for the synthesis of mixed alumina-silicone based nanomaterials was performed using the same conditions as employed for the synthesis of alumina-based nanomaterials. The only difference in these two syntheses was the type of precursors. For alumina-based nanomaterials synthesis TMA precursor was used, while for the synthesis of mixed alumina-silicone based nanomaterials synthesis mixture of TMA and TCMS in ratios of 1:2 was used. TMA and TCMS were mixed inside the glove box and injected inside the glass desiccator kept at a specific relative humidity.

3.6.3.3 Annealing

Thermal stability of synthesized mixed alumina-silicone nanomaterials was tested by annealing the coated substrates in air using muffle furnace (Carbolite). Substrates were heated at 300°C, 400°C, 500°C and 600°C with the heating rate of 10°C/minute for the duration of 4 hours followed by cooling inside the furnace.

3.7 Characterization

3.7.1 Scanning electron microscopy

Scanning electron microscopy (SEM) was performed in the Center for Microscopy and Image Analysis (ZMB) of the University of Zurich. Prior to SEM analysis all samples were coated with 10 nm thick platinum layer using Sputter Coater Safematic CCU-010 (Switzerland) under high vacuum. SEM investigations were carried out using Zeiss Supra 50 VP SEM. Secondary electron and in-lens detectors were used to acquire images with an accelerating voltage of 6 keV and 2 keV respectively. For secondary electron detector working distance of 9 mm was used while for in-lens detector working distance of 3 mm was used to obtain images.

3.7.2 Transmission electron microscopy

Transmission electron microscopy (TEM) was performed at ZMB of the University of Zurich. A small piece of the substrate coated with nanomaterials was cut and immersed in toluene. Sonication was performed for the duration of 2-3 minutes. Few drops of nanoparticles dispersion were drop cast on a carbon supported copper TEM grid. The procedure was repeated three times to increase the number of nanoparticles on copper grid. FEI Tecnai G2 Spirit microscope with an accelerating voltage of 120 keV was used for analysis.

3.7.3 Energy dispersive x-ray spectroscopy

Energy dispersive x-ray spectroscopy (EDX) was carried out at Zeiss Supra 50 VP SEM equipped with a sapphire Si (Li) detecting unit (EDAX Inc.). Accelerating voltage of 10-15 keV was used for every analysis. JOEL JSM-6010 SEM equipped with EDX detector (Bruker) was also used for EDX analysis operated at an accelerating voltage of 10 keV. EDX analysis at TEM was performed using X-Max system (Oxford) at an accelerating voltage of 120 keV.

3.7.4 IR spectroscopy

Attenuated total reflectance (ATR) IR spectroscopy was performed using Vertex (Bruker) equipped with an ATR accessory. Samples were scanned in the range of 500-4000 cm^{-1} with the scan speed of 252 scans per minute.

3.7.5 UV-Vis spectroscopy

Lambda 950 (Perkin Elmer) was used for UV-Vis spectroscopy. Scanning of the samples was performed at the speed of 268 nm/min in the wavelength range of 300-900 nm.

3.7.6 Photoluminescence spectroscopy

Fluorolog® spectrofluorometer (Horiba) was used for photoluminescence measurements. Xenon lamp was used as a source. Grating density of 1200 and slit width of 3 nm was employed. Emission spectra was collected in the range of 340-600 nm.

3.7.7 X-ray photoelectron spectroscopy

X-ray photoelectron spectroscopy (XPS) was carried out at Ph5000 VersaProbe spectrometer (ULVAC-PHI, Inc.) equipped with multichannel detection system consisting of 16 channels and 180^{o} spherical capacitor energy analyzer. Al-Kα monochromatic source (1486.6 eV) with a spot size of 200 μm was used. To acquire spectra base pressure of 5×10^{-8} Pa was used. Pass energy of 46.95 eV and 187.85 eV was used for detail spectra and survey scan respectively. FAT analyzer mode was run with the electrons emitted an angle of 45° to the surface normal. Charge neutralization was performed throughout the analysis using cool cathode electron flood source (1.2 eV) and low energy Ar+- ions (10 eV). CasaXPS (Version 2.3.16) program was used for the data analysis. All spectra were calibrated to aliphatic C at 285 eV.

3.7.8 Characterization of superhydrophobicity

For the characterization of superhydrophobic properties contact angle system OCA (Dataphysics, Germany) was employed. SCA software (Dataphysics, Germany) was used for contact angle measurements. For contact angle measurements Milli-Q® water with a volume of 5 µL was used, and for sliding angle measurements 10 µL volume was used. For one sample at least 3 contact angle measurements were performed, and the average value of contact angle was used for further calculations. Videos with high speed camera were recorded using SpeedCam MiniVis EoSens (HS VISION) attached to KRÜSS DSA100 system. Videos of water droplet sliding were recorded at the speed of 200 frames per second.

4. Results and Discussion

4.1 Hydroxyapatite biomineralization

High life expectancy or serious accidental injuries often require orthopedic implantation. For implant applications the use of different materials such as polymers, ceramics and metals has been explored. Especially, the application of metals e.g. titanium as orthopedic implants has been widely reported. Even the metals offer better mechanical properties but still they lack in biocompatibility [95]. Modification of the metal surface with biocompatible material is an attractive alternative for the fabrication of biomaterials. Hydroxyapatite (HA) is an example of such a bioactive and biocompatible material used for the fabrication of biomaterials. HA is an inorganic mineral with a chemical formula of $Ca_{10}(PO_4)_6(OH)_2$ constituting major portion (~60%) of bone tissues. Due to its bioactivity it binds effectively with the growing bones and shows bone formation *in-vivo* conditions [96]. The modification of the substrate surface with HA is broadly divided into two broad categories: (i) coating method, (ii) bio-inspired mineralization. Different coatings methods such as electrochemical deposition [97], electrophoretic deposition [98], sol-gel method [99], pulsed laser deposition [100] and plasma spraying methods [101] have been explored for the deposition of HA on the substrates. Among all of these coating techniques, plasma spraying is the only coating method which has been approved by Food and Drug Administration (FDA) [101]. The plasma spraying method is commercially viable technique, but this process has drawbacks such as the phase impurity of deposited HA and desorption of HA coatings from the surface [102].

These drawbacks can be overcome by growing bioactive HA using bio-inspired mineralization methods which mimic natural mineralization processes. These consist of placing the substrate in a simulated body fluid (SBF) which has composition and concentration of salts similar to human blood plasma. SBF is a model fluid which is used to check the bioactivity of the materials. The advantages of bio-inspired growth include the ability of growing HA on complex and intricate shapes as well as the use of simple and economical technology. Bio-inspired growth of HA has been extended to coat a range of substrate materials such as silicon [103], metals [104] and nanomaterials e.g. porous silica [105], polymer microspheres [106] and graphene oxide [107] etc. The idea of using nanomaterials as a scaffold to grow HA is quite unique as the high surface area promotes fast growth of HA. The development of such a nanomaterial which provides high surface area as well as involves facile fabrication could prove to be beneficial. SNFs which form a 1D network of biocompatible silicone polymer provide high aspect ratio and involve room temperature processing. Moreover, SNFs are chemically stable and have the ability to be coated on a range of substrates.

4.1.1 Synthesis and functionalization of SNFs

SNFs employed to study the growth of HA were synthesized using Protocol I (details in Materials and Method section). Cleaned and activated glass substrate were placed in a custom-built coating chamber. Relative humidity was maintained at ~35% by co-flow of dry and humidified nitrogen. After 1 hour of equilibration time, 500 µL of TCMS was introduced into the coating chamber and reaction was carried out for the duration of 13-14 hours (overnight). SNFs were coated on both sides of the glass substrate leading to a network of nanofilament structure (Figure 4.1b). Oxygen plasma treatment was performed on the synthesized SNFs to create abundant moieties of hydroxyl groups (Figure 4.1c). These hydroxyl groups act as an anchor group to attach carboxylic acid or amine functional groups to further tailor the surface properties of SNFs [11]. SNFs functionalized with carboxylic acid and amine groups were immersed in 1.5 SBF at 37°C to study the growth of HA (details in Materials and Method section).

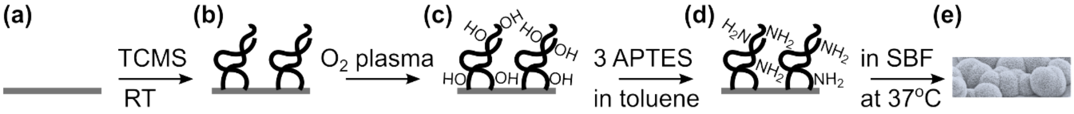

Figure 4.1. Schematic illustration of steps performed to prepare the substrate for the growth of HA

The extent of functionalization and SNF coating on glass substrate was characterized by checking the wettability of the substrates. Contact angle value of 156.5° ± 4.4° (Figure 4.2a) was observed on glass substrate coated with SNFs confirming the superhydrophobic nature of the coating. After attachment of amine or carboxylic acid functional groups on the surface of SNFs contact angle values of 20.9° ± 2.2° and 26.7° ± 2.7° (Figure 4.2b-c) were observed indicating the hydrophilic nature of modified SNFs surface. For control experiments, glass substrates without SNFs were functionalized with carboxylic acid and amine groups using the same procedure. The purpose to functionalize bare glass substrate was to check whether high surface area of SNFs plays any role to promote fast growth of HA. Contact angle values of 56.5° ± 0.5° (Figure 4.2d) were observed on the control substrates functionalized with amine and carboxylic acid group. The value of the contact angle on functionalized glass substrates were in agreement with literature report [108]. It is worth mentioning the structural integrity of grown SNFs after amine or carboxylic acid functionalization did not change. Highly entangled nanofilament structure was still maintained after the functionalization step (Figure 4.3 & Figure 4.4).

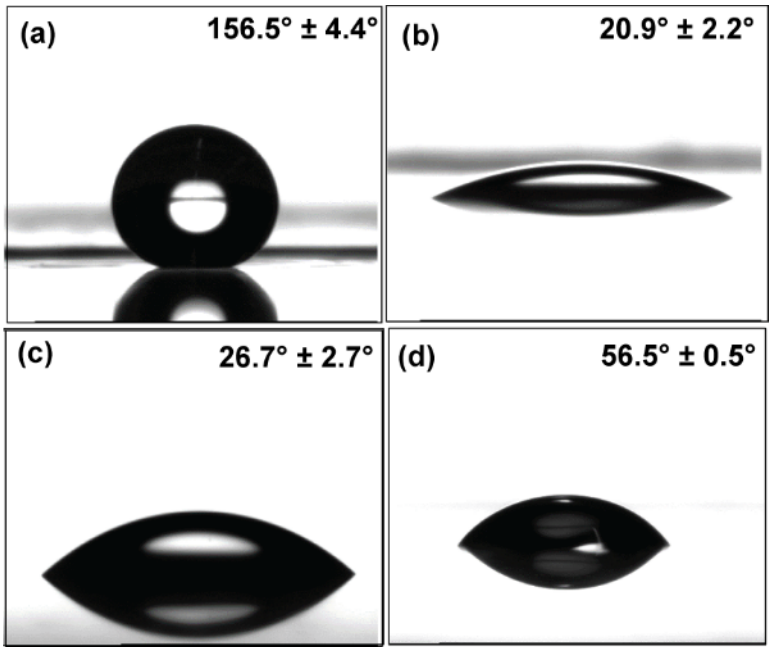

Figure 4.2. Water contact angle on (a) SNFs coated, (b) SNFs-amine functionalized, (c) SNFs-carboxylic acid functionalized, (d) amine or carboxylic acid functionalized glass substrate. Reprinted with permission from [109]

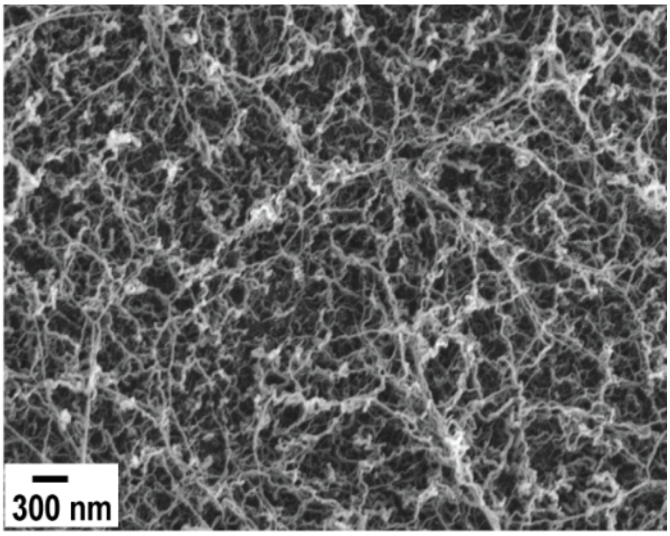

Figure 4.3. SEM of as synthesized SNFs. Reprinted with permission from [109]

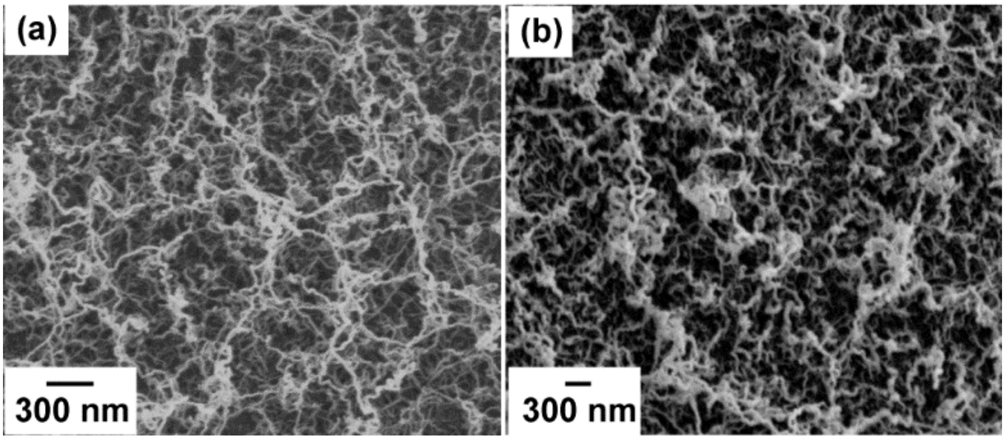

Figure 4.4. SEM SNFs after (a) amine, (b) carboxylic acid functionalization. Reprinted with permission from [109]

4.1.2 Growth of Hydroxyapatite

To study biomineralization of HA, the substrates were incubated in SBF for the duration of 4 days. After incubation washing of substrates with copious amounts of Milli-Q® was performed followed by drying under the stream of nitrogen. The glass substrates functionalized with amine or carboxylic acid are known to induce HA mineralization after 2-3 weeks of incubation in SBF. The glass substrates functionalized with amine or carboxylic acid groups did not lead to growth of HA after 4 days of incubation (Figure 4.5a-b). The same observation was made for the Deconex cleaned glass substrate (Figure 4.5c). Moreover, oxygen plasma activated SNFs substrate also did not induce any mineralization of HA (Figure 4.5d). The reason behind no HA mineralization of oxygen plasma activated SNFs could be due to low tendency of hydroxyl groups for apatite formation.

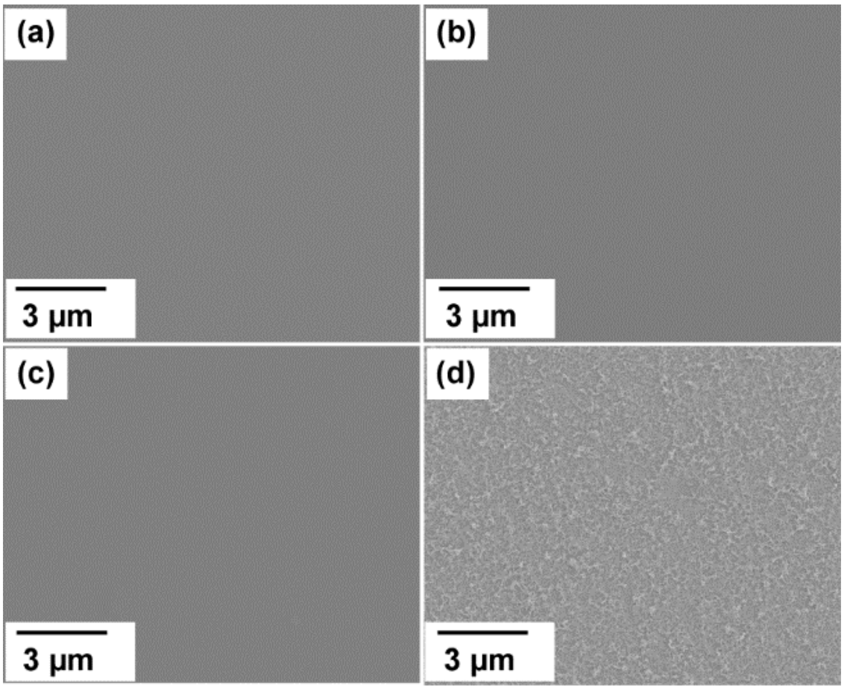

Figure 4.5. SEM of (a) amine functionalized, (b) carboxylic acid functionalized, (c) Deconex cleaned glass substrate and (d) oxygen plasma activated SNFs substrate after 4 days of incubation in SBF. Reprinted with permission from [109]

However, the SNFs functionalized with amine and carboxylic acid showed formation of HA after 4 days of incubation in SBF. After 4 days of incubation carboxylic acid functionalized SNFs showed growth of HA particles with average diameter of 2-8 µm, while larger HA particles with the average diameter of (~20 µm) were observed on amine functionalized SNFs substrates (Figure 4.6a-d). Amine functionalized SNFs induced abrupt growth of HA and within 4 days of incubation in SBF homogenous growth of HA was observed. The fast growth of HA on functionalized SNFs is most likely due to high surface area of 1D SNFs which offers large density of nucleation sites for the mineralization of HA.

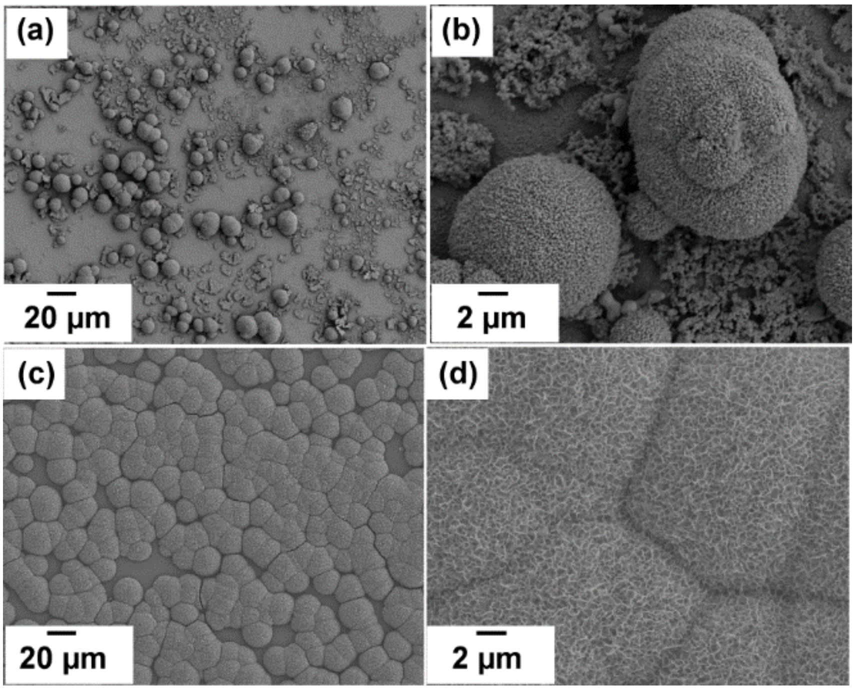

Figure 4.6. SEM of (a-b) carboxylic acid functionalized SNFs, (c-d) amine functionalized SNFs substrate after 4 days of incubation in SBF. Reprinted with permission from [109]

To check the chemical composition of HA particles, EDX analysis of HA grown on amine functionalized SNFs was performed. The EDX measurement revealed the presence of Ca and P confirming the presence of HA on the surface of the substrate (Figure 4.7). The signal from C could arise from the thick carpet of SNFs underneath HA. To confirm if SNFs still exist after incubation in SBF, SEM of amine functionalized SNFs substrate after SBF incubation was performed. SEM showed presence of SNFs in between two HA particles confirming the structural integrity of SNFs after incubation in SBF (Figure 4.8). EDX spectra of corresponding region between two HA is shown in Figure 4.8 showing C, O and Si peaks corresponding to SNFs which are essentially composed of polysiloxanes. Pt signals are due to the thin layer of platinum metal which was sputter coated to make the sample conductive. The as grown HA was highly porous in nature consisting of three dimensional interconnected channels. The high porosity shows the biological nature of as grown HA (Figure 4.9).

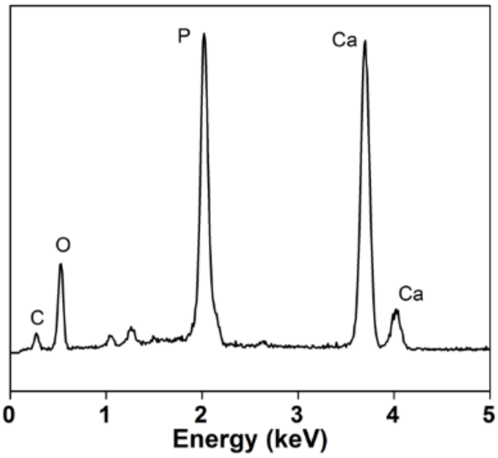

Figure 4.7. EDX analysis of amine functionalized SNFs substrate after 4 days of incubation in SBF. Reprinted with permission from [109]

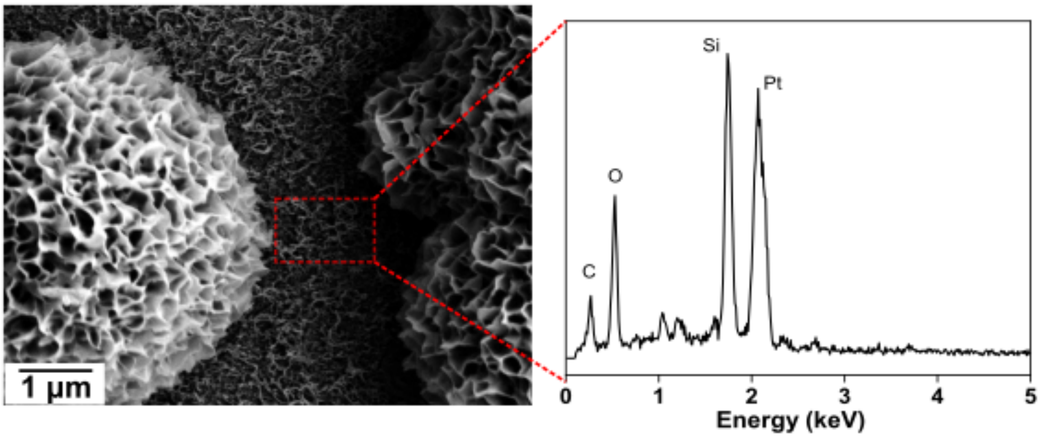

Figure 4.8. SEM of amine functionalized SNFs substrate after 4 days of incubation in SBF immersion, EDX of a respective region between two HA particles. Reprinted with permission from [109]

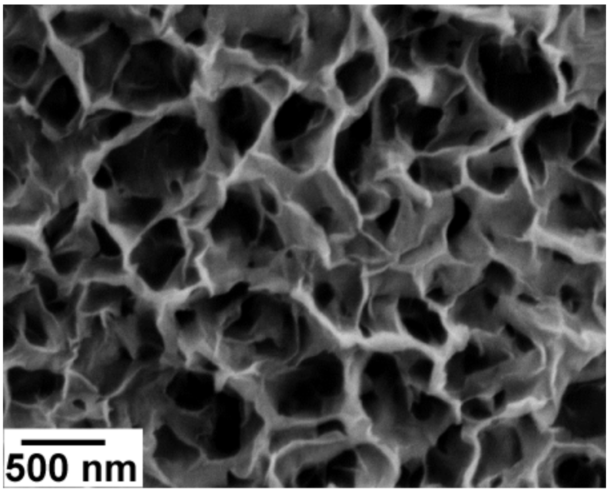

Figure 4.9. Porous structure of HA. Reprinted with permission from [109]

4.1.3 Time dependent studies of HA biomineralization

The time dependent growth of HA on functionalized SNFs was studied to gain more insight on the mineralization process. The amine functionalized SNFs substrates were incubated in SBF at 37°C for the duration of 1, 3, 5 and 7 days. After removing the substrates from SBF, substrates were washed with Milli-Q® water and dried under the stream of nitrogen. Characterization of the substrates was performed using SEM and EDX analysis. SEM revealed presence of only few scattered particulate structures after 1 day of incubation in SBF (Figure 4.10a-b). Increase in the density of particulate structures as a function of incubation time was observed. HA started to grow in the form of arrays of particles with increase of incubation period from 1 to 3 days (Figure 4.10c-d). After 5 days of incubation time thick coating of HA particles was observed (Figure 4.10e-f). 7 days of incubation lead to formation of thick layer of HA particles covering homogenously the entire surface of the substrate (Figure 4.10g-h). The thickness of HA particles layer was also monitored as a function of incubation time which gradually increased from 2.8 ± 1.5 µm (1 day) to 14.1 ± 2.9 µm after 7 days of incubation in SBF (Figure 4.11).

EDX analysis revealed the HA mineralized under different incubation times had different composition. HA particles grown at low incubation period were Ca deficient. Therefore, molar ratios of Ca and P were calculated for HA grown at different stages and plotted in Figure 4.12. Ca/P molar was ~1.2 after 5 days of incubation and increased to 1.55 after 7 days of incubation. At low incubation period amine groups on functionalized SNF promote the deposition of oppositely charged ions (phosphate ions) at the surface leading to low Ca/P molar ratio. With increase in incubation period, the surface bound phosphate ions attract calcium ions from the SBF which leads to an increase in Ca/P molar ratio in HA.

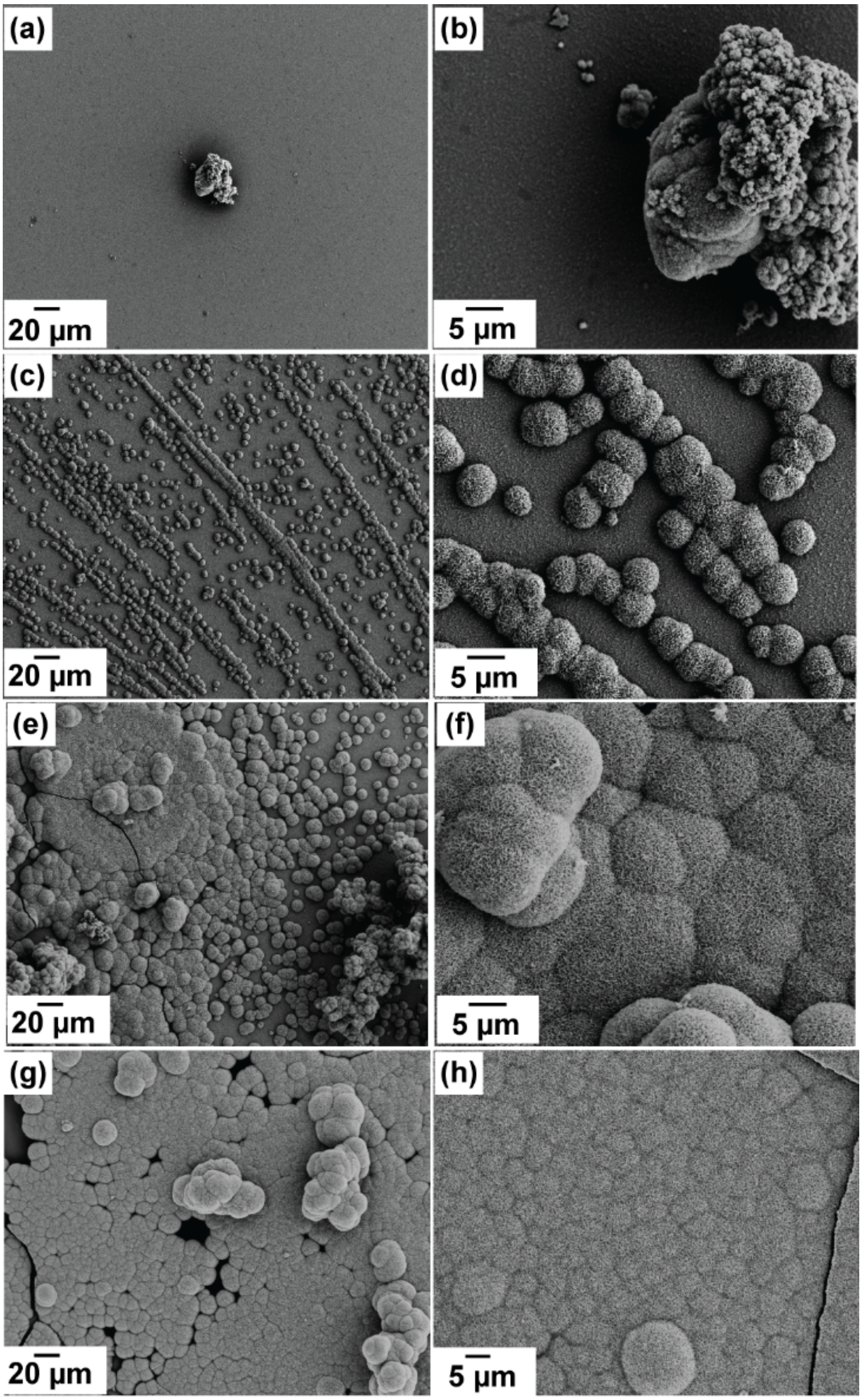

Figure 4.10. SEM of the substrates after (a-b) 1 days, (c-d) 3 days, (e-f) 5 days, (g-h) 7 days of incubation in SBF. Reprinted with permission from [109]

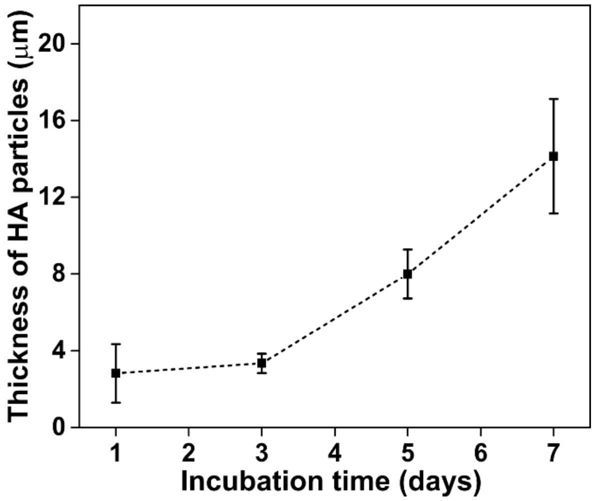

Figure 4.11. Thickness of HA particles as a function of incubation time in days. Reprinted with permission from [109]

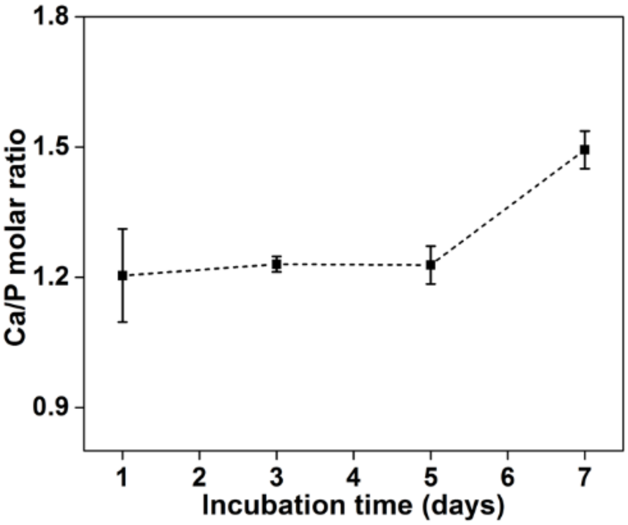

Figure 4.12. Ca/P molar ratio as a function of incubation time in days. Reprinted with permission from [109]

The mineralization of HA on functionalized SNFs was more rapid as compared with other literature reports [103]. A similar growth rate was observed in another study which involved the application of composite material e.g. poly(ε-caprolactone)/bioglass [110] as a template for the growth of HA. The synthesis of this composite material involved high temperature processing and complicated processing steps which make this material less economical. On the other hand, synthesis of SNFs involves ambient conditions (pressure and temperature) and gas phase processing without production of any liquid waste. The ease of coating substrates with SNFs which possess high surface area and are non-toxic in nature, make this methodology a unique avenue for biomineralization.

4.2 Multifunctional electrical conductive and superhydrophobic coatings

Coating is a vital step towards modifying the surface properties of the materials. The coatings inspired by nature have gained considerable attention in recent years. Superhydrophobic coatings with water contact angle above 150^o have been found useful for applications such as self-cleaning [111] [112], anti-icing [113], antifogging [114], antireflective [115], liquid transportation [116], drag reduction [117], oil/water separation [118]. The scalability and practicability of the superhydrophobic coatings is very important, moreover the chemical and mechanical stability of these coatings also plays a crucial role for real life applications. The smart superhydrophobic coatings with added features such as transparency [119], magnetism [120], antimicrobial property [121] and electrical conduction [122] are the new focus of academic and industrial research. For example, superhydrophobic coatings with electrical conduction property are used to protect complicated devices. The accumulation of charge at the surface often leads to deterioration of the coatings and influences the performance of the devices. Therefore, electrically conductive superhydrophobic coatings can improve the device reliability by removing the accumulated static charge. The multifunctional coatings with the combined superhydrophobic and conductive property are promising candidates for a wide range of applications such as smart textiles [6], electrode materials [123], electromagnetic interference shielding [124], microelectronics packaging [125] and microfluidics [126].

Superhydrophobic electrical conductive coatings are usually prepared by dispersing conductive fillers (e.g. carbon based) in the hydrophobic polymer matrix [127]. The use of expensive filler materials such as carbon nanotubes (CNTs) [128] [129] and graphene [130] is widely reported. While the fabrication of such coatings involving inexpensive carbon-based filler materials e.g. carbon nanofibers [131] or graphite [122] are rather less explored. In the next section the fabrication of superhydrophobic and conductive coatings is described by applying a facile method which involves processing at ambient conditions and use of inexpensive carbon nanofibers.

4.2.1 Fabrication of multifunctional coatings

Cleaned and plasma activated glass substrates were placed in the coating chamber and the synthesis was carried out using protocol II (described in Materials and Method section). The glass substrate coated with homogenous and dense carpet of SNFs was dip coated in the suspension of CNFs followed by washing with toluene and Milli-Q® water. Drying of substrates was performed under the stream of nitrogen. The schematics of the procedure used for the fabrication of multifunctional coatings are shown in Figure 4.13.

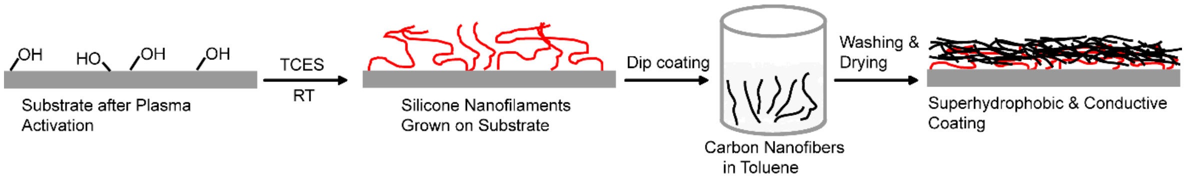

Figure 4.13. Schematics of conductive and superhydrophobic coatings preparation. Reprinted with permission from [132]

4.2.2 Microstructure of multifunctional coatings

The microstructure of the substrates was observed by SEM and the superhydrophobic characteristic of the substrates was checked by measuring the static water contact angles. Figure 4.14 shows the SEM image of the substrates after SNFs coating and dip coating in various suspensions of CNFs in toluene. Contact angles of water on corresponding substrates are shown as inset in Figure 4.14. A clear difference in the surface morphology of the substrates coated with SNFs and dip coating of SNFs coated substrates in the suspension of 0.1 and 0.25 wt. % CNFs can be observed in Figure 4.14a-c. However, the substrates prepared by dip coating in the 0.5, 0.75 and 1 wt. % CNFs suspension had the similar surface morphology (Figure 4.14d-f). The difference in surface morphology arises due to the difference in the size (diameter) of SNFs and CNFs. To confirm this the size distribution of SNFs and CNFs was calculated. CNFs deposited on carbon tape and SNFs coated substrates were observed under SEM. Size distribution was calculated by measuring at least 150 SNFs and CNFs midsections by image J® software. Size distribution of SNFs and CNFs shown in Figure 4.15 confirms CNFs are larger in size as compared with SNFs.

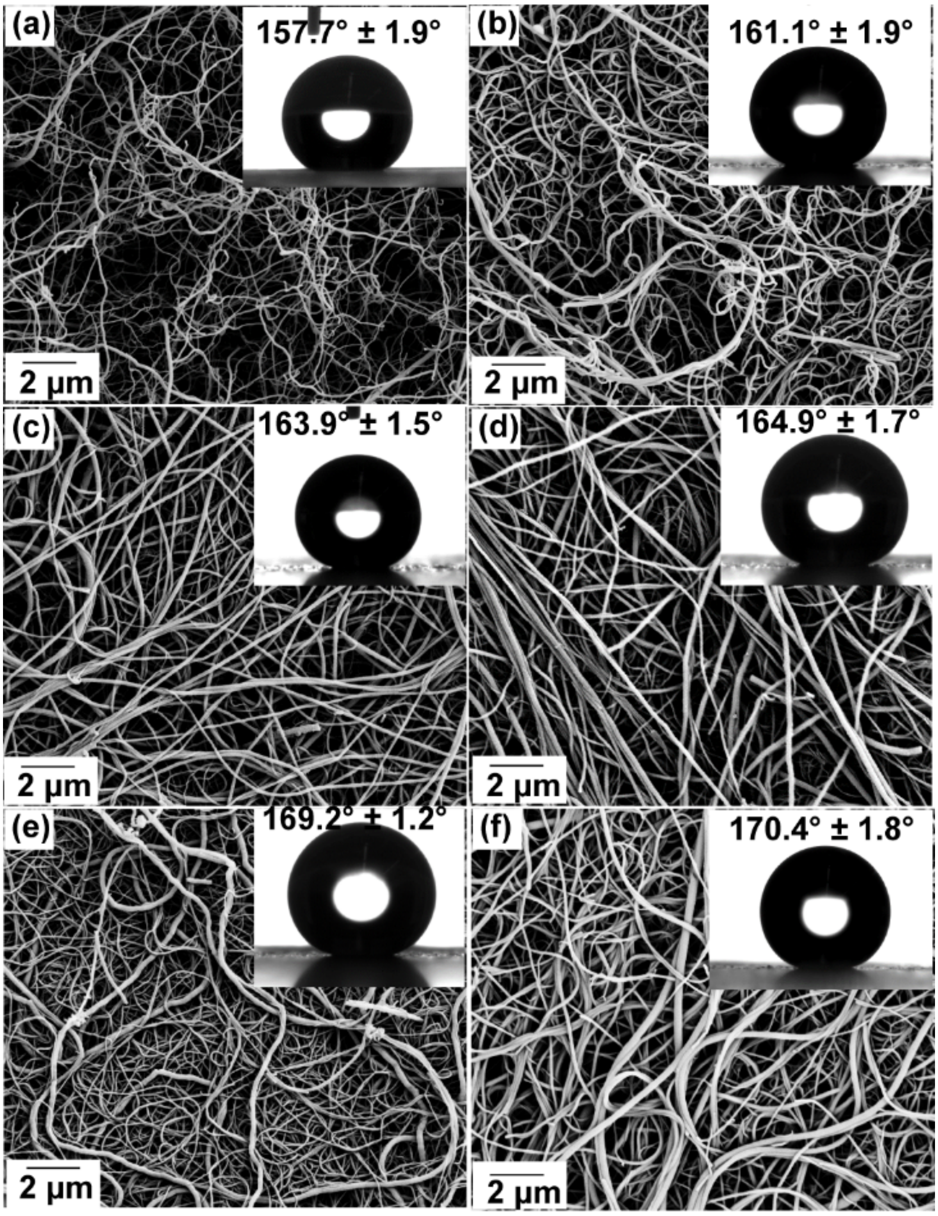

Figure 4.14. SEM image of (a) glass substrate coated with SNFs, SNFs coated glass substrate after dip coating in (b) 0.1, (c) 0.25, (d) 0.5, (e) 0.75 and (f) 1 wt. % CNFs suspension. Insets show water contact angles on corresponding coatings. Reprinted with permission from [132]

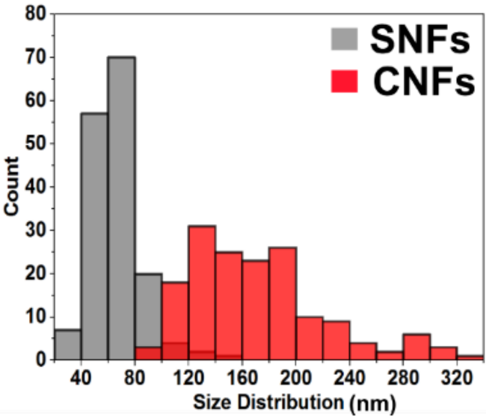

Figure 4.15. Size distribution (diameter) of SNFs and CNFs. Reprinted with permission from [132]

The compression of SNFs after dip coating in CNFs suspension was also observed. The cross-sectional SEM image of SNFs coated substrate and the substrate after dip coating in 1 wt. % CNFs suspension is shown in Figure 4.16a-b. Compression of SNFs after dip coating with CNFs can be attributed to the low stiffness of SNFs. SNFs which are silicone material and consist of polysiloxane network are less stiff as compared with carbon (CNFs) [133] [134]. Even SNFs are compressed because of CNFs, but they still provide a rough hydrophobic skeleton for CNFs deposition. EDX mapping of the coatings prepared by dip coating SNFs coated substrates with 1 wt. % CNFs confirms the presence of CNFs on the surface. The signals from the SNFs which are underneath CNFs are also detected in EDX mapping (Figure 4.16c).

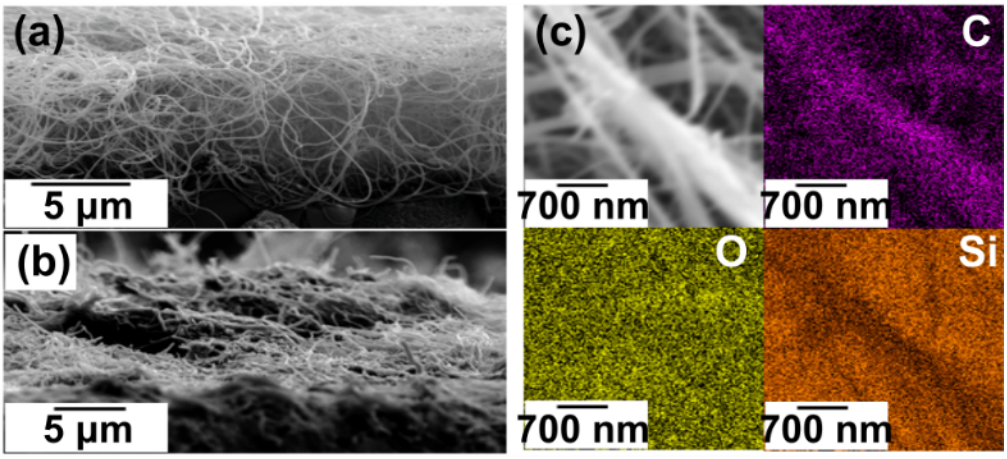

Figure 4.16. Cross-sectional view of substrate coated with (a) SNFs, (b) 1 wt. % CNFs coatings, (c) SEM image and elemental mapping performed on 1 wt. % CNFs coatings. Reprinted with permission from [132]

4.2.3 Electrical conduction and superhydrophobicity

The presence of CNFs on the surface imparts electrical conduction to the coatings. The electrical conductivity of the prepared coatings was measured in terms of sheet resistance. Figure 4.17a shows dependence of sheet resistance of the prepared coatings as a function of CNFs content in the suspension. The sheet resistance of the coatings decreased with an increase in the content of CNFs in the suspension. The decrease in sheet resistance indicates an increase in the electrical conductivity of the coatings. This can be explained by percolation theory which describes the behavior of connected clusters. Electron transport is dependent on the conductive pathways. The increase in the number of conducting paths increases electrical conductivity which in turn decreases the sheet resistance. The coatings prepared by dip coating the substrates in various CNFs suspensions have different density of CNFs at the surface which results in the change of sheet resistance as function of CNFs content. The presence of CNFs at the surface does not only improve electrical property of the coatings but it also improves the superhydrophobicity. An increase in contact angle and decrease in the sliding angle of water was observed as a function of CNFs content in the suspension (Figure 4.17b). The contact angles increased from 157.7° ± 1.9° (SNFs) to 170.4° ± 1.8° (1 wt. % CNFs). While the sliding angles decreased from 13.8° ± 1.6° (SNFs) to 4.6° ± 0.91° (1 wt. % CNFs).

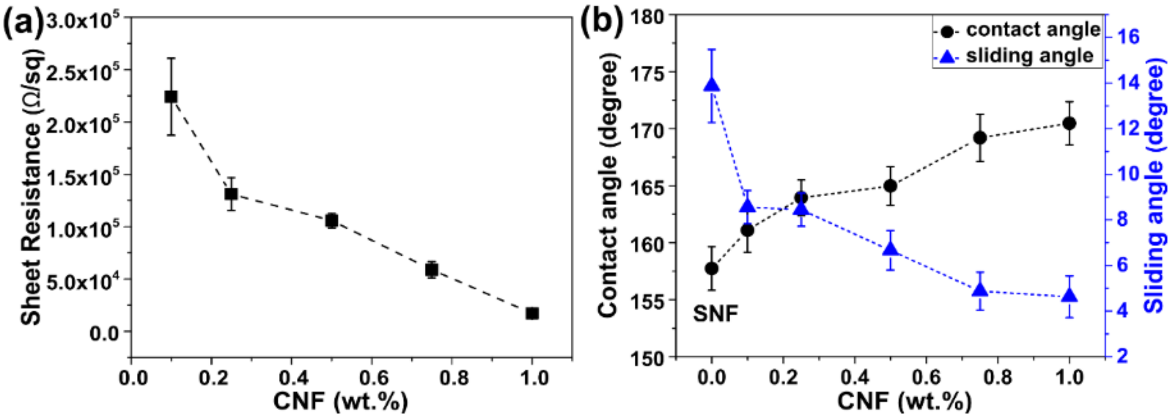

Figure 4.17. (a) Sheet resistance of the coatings, (b) contact and sliding angles of the coatings as function of CNFs content in the suspension. Reprinted with permission from [132]

In order to check whether the superhydrophobic skeleton of SNFs is necessary to bind CNFs on the substrate, control experiments were performed on the cleaned glass substrate and silane functionalized glass substrates. The cleaned and plasma activated glass substrate was immersed in anhydrous toluene (water ppm ~ 30) and functionalization was performed using trichloroethylsilane. All control substrates were dip coated in 1 wt. % CNFs suspension followed by washing with toluene and Milli-Q® water. Contact angle measurements were performed before and after the functionalization step. The cleaned and plasma activated substrates remained superhydrophilic before and after dip coating (Figure 4.18a-b). While contact angle values increased from 0° (superhydrophilic) to 77.9° ± 3.1° (after silane functionalization), which increased further to 91.6° ± 2.4° after dip coating (Figure 4.18c-d). The silane functionalized substrates did not show presence of nanofilament structures before or after dip coating (Figure 4.19). The control substrates when tested after dip coating using 4 probe did not show any electrical conduction implying a superhydrophobic network of SNFs is necessary to effectively bind CNFs on the surface of the substrate to yield superhydrophobic and conductive coatings.

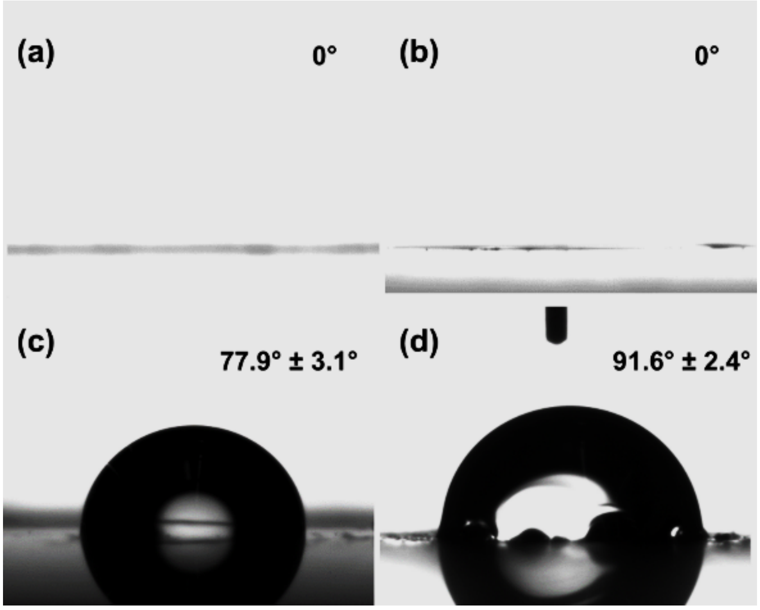

Figure 4.18. Contact angle of (a) cleaned substrate, (b) dip coated substrate (c) silane functionalized substrate, (d) dip coated silane functionalized substrate. Reprinted with permission from [132]

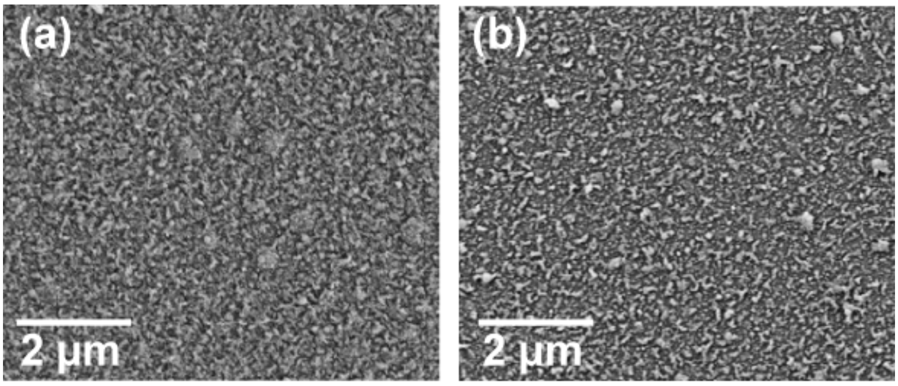

Figure 4.19. SEM image of (a) silane functionalized substrate, (b) dip coated silane functionalized substrate. Reprinted with permission from [132]

4.2.4 Optical transparency

The prepared multifunctional coatings are not only superhydrophobic and conductive in nature but they also possess optical transparency. The optical transparency of the coatings can be tuned by simply varying the content of CNFs in the suspension to yield transparent to semi-transparent coatings. Figure 4.20 shows UV-Vis transmittance spectra of the coatings scanned in the range of 300-900 nm. The glass substrates coated with SNFs showed 95.4% transmittance and uncoated glass substrate showed 91.9% transmittance at 550 nm wavelength. The high transmittance of SNFs coated substrates is due to the anti-reflective properties of SNFs [1]. A gradual decrease in the values of transmittance was observed for the coatings prepared by dip coating in CNFs suspension. The transmittance values decreased from 81.2% (0.1 wt. % CNFs) to 41.07% (1 wt. % CNFs) when compared at 550 nm wavelength. The decrease in the value of transmittance can be attributed to the light scattering which results from the hierarchical structure of CNFs on the surface. Optical micrographs of the substrates prepared with 0.1 and 1 wt. % CNFs suspension are shown as inset in Figure 4.20.

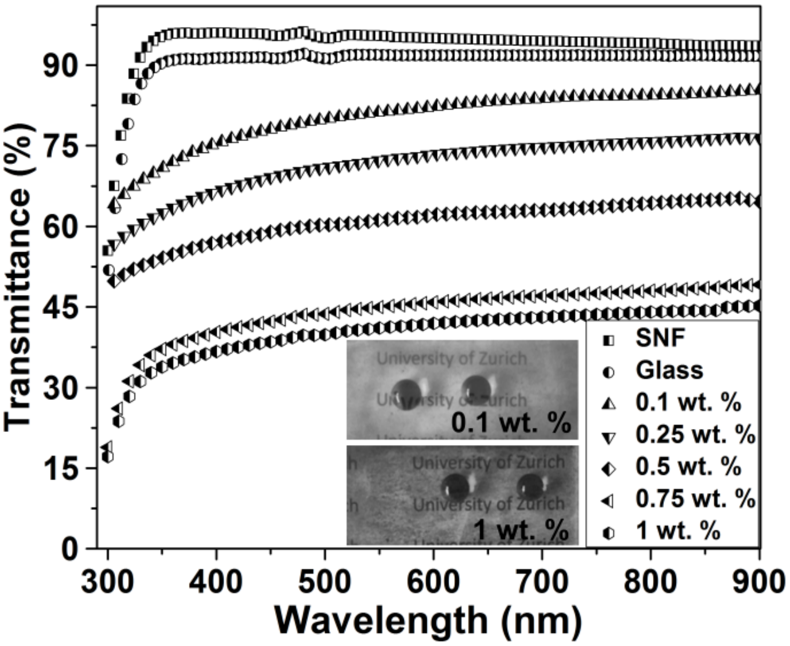

Figure 4.20. Transmittance spectra of coatings (inset show optical photographs of the substrates prepared with 0.1 and 1 wt. % CNFs). Reprinted with permission from [132]

4.2.5 Other surface properties

Other than transparency and electrical conduction, the prepared multifunctional coatings illustrate excellent self-cleaning ability. Figure 4.21a exhibits the self-cleaning property of the coatings prepared with 1 wt. % CNFs where a moving 5 μL water droplet removes sand particles from the surface. Incorporation of sand particles in the water droplet to eventually remove the particles from the surface can be clearly seen in Figure 4.21a. Figure 4.21b shows the optical micrographs of the coatings prepared with 1 wt. % CNFs where powdered chalk particles are completely removed from the surface. In addition to self-cleaning property, the prepared coatings illustrate difference in adhesion to water. Water droplet sliding was observed for all surfaces within 30 seconds of water droplet exposure. However, after prolonged exposure (3-5 minutes) to the water droplet, a difference in surface behavior was observed. After prolonged exposure water droplets were pinned at the surface of SNFs coated substrate and 0.1 wt. % CNFs substrates illustrating strong adhesion of water to the surface. This strong water adhesion can be seen in Figure 4.21c, where a syringe could not remove 5 μL water droplet from the surface of the coating prepared with 0.1 wt. % CNFs. However, the coatings prepared with 0.25, 0.5, 0.75 and 1 wt. % CNFs showed low water adhesion and sliding of water droplets was observed after prolonged exposure. Figure 4.21d shows a syringe moving towards 5 μL water droplet placed on surface of the coating prepared with 1 wt. % CNFs could easily remove the droplet due to low water adhesion. Tuning the water adhesion by simply controlling the content of CNFs in the suspension is useful for applications such as droplet transportation, collection and reactions in confined volumes.

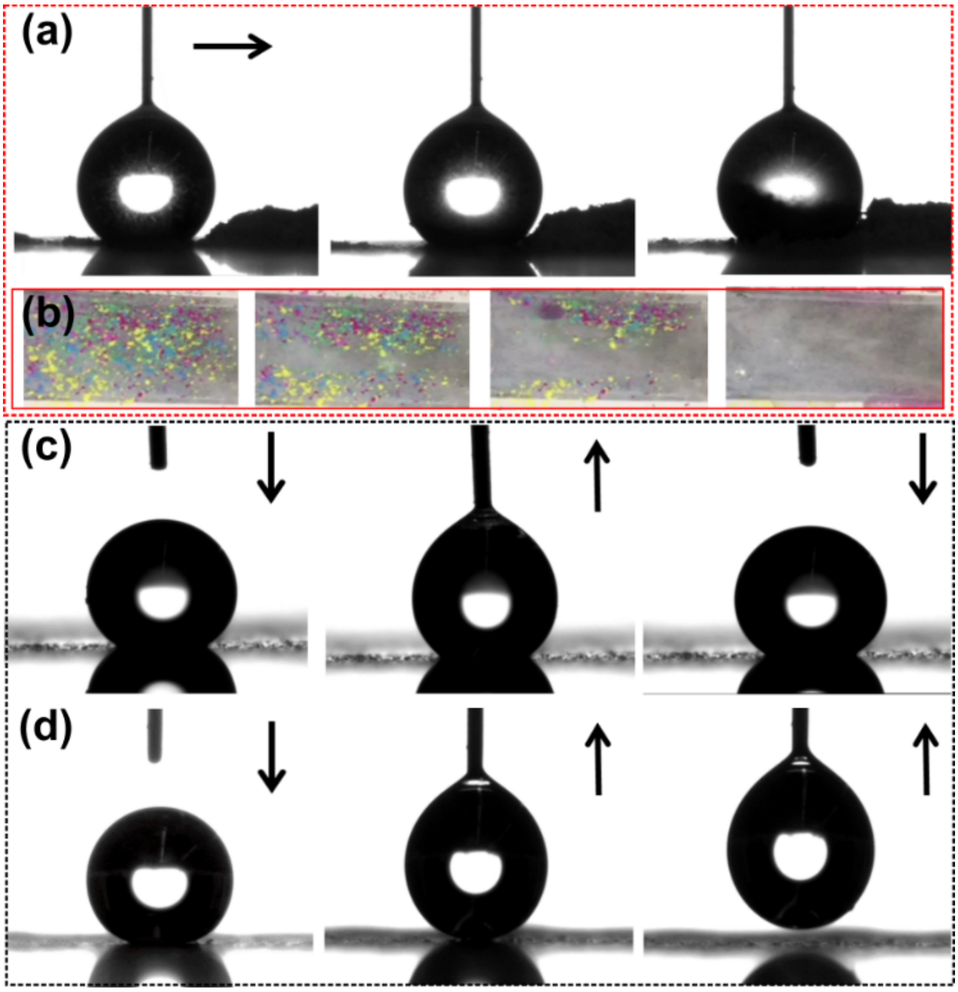

Figure 4.21. Self-cleaning ability of the coatings prepared with 1 wt. % CNFs (a) removal of sand particles, (b) optical micrograph illustrating removal of powdered chalk particles from the surface. Coatings with (c) high and (d) low water adhesion, arrows indicate the direction of syringe movement. Reprinted with permission from [132]

To demonstrate the droplet transportation a very common reaction between $CuSO_4$ and NaOH has been shown in Figure 4.22. Aqueous solutions of $CuSO_4$ and NaOH were prepared with molar concentrations of 0.1 and 0.2 respectively. Aqueous solution of $CuSO_4$ was placed on the surface prepared with 1 wt. % CNFs (low water adhesion) and aqueous solution of NaOH was placed on the surface prepared with 0.1 wt. % CNFs (high water adhesion). The droplet which contained aqueous $CuSO_4$ solution could easily be removed by a metal tip due to its low adhesion to the surface Figure 4.22a-d. Aqueous $CuSO_4$ droplet was transported to the surface with high water adhesion to merge with aqueous NaOH droplet (Figure 4.22e). When two droplets merge, precipitates of $Cu(OH)_2$ were formed due to the reaction between Cu^{2+} and OH^- ions (Figure 4.22f-h). Due to the high adhesion of the surface prepared with 0.1 wt. % CNFs, the droplet could not be removed by the metal tip. This reaction is only one example of possible application of the surfaces prepared with variable adhesion and these surfaces have a great potential in a wide range of applications such as oil pollution treatment, micro-droplet transportation and microfluidics.

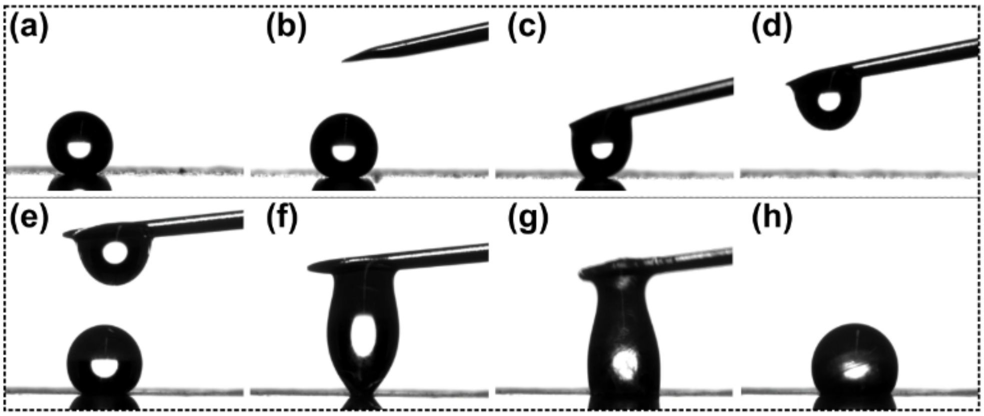

Figure 4.22. Illustration of water droplet transportation. Reprinted with permission from [132]

4.2.6 Environmental durability of the coatings

Usually environment has an impact on the properties of coatings which limits their practical applications. The stability of the coatings in humid environment or water contact is of vital significance. The durability of the coatings to humid conditions was tested by exposing the substrates to extreme humid conditions. The substrates were placed in the glass desiccator which was maintained at relative humidity of (90% ± 3%) by constant flow of humidified nitrogen. The stability of the coatings to water contact was measured by immersing the substrates in water. The coatings used for these studies were prepared by dip coating SNFs coated substrates in 0.1 and 1 wt. % CNFs suspensions respectively. The substrates were exposed to humid conditions or water immersion at room temperature for the duration of 2, 4, 6, 8 and 16 hours followed by washing with Milli-Q$^{®}$ water and drying under the stream of nitrogen. Contact and sliding angles of the coatings as a function of exposure time to different environmental conditions were measured. In addition to hydrophobic characterization, sheet resistance of the coatings was also measured to check their electrical properties. Figure 4.23a shows the contact angle, sliding angle and sheet resistance of the coatings as a function of exposure time to humid conditions, while Figure 4.23b shows the similar properties of the coatings as function of water immersion period. The coatings remained superhydrophobic even after 16 hours of exposure to humid conditions and there was no appreciable change in contact or sliding angles of the coatings. The coatings remained conductive in nature after exposure to humid conditions and a small increase in sheet resistance was observed after 16 hours of exposure. There was no significant change in superhydrophobicity of the coatings after immersion in water which shows the good resistance of coatings to water contact. Further, the coatings also remained conductive in nature with a small increase in the sheet resistance which could be due to the removal of CNFs due to water contact.

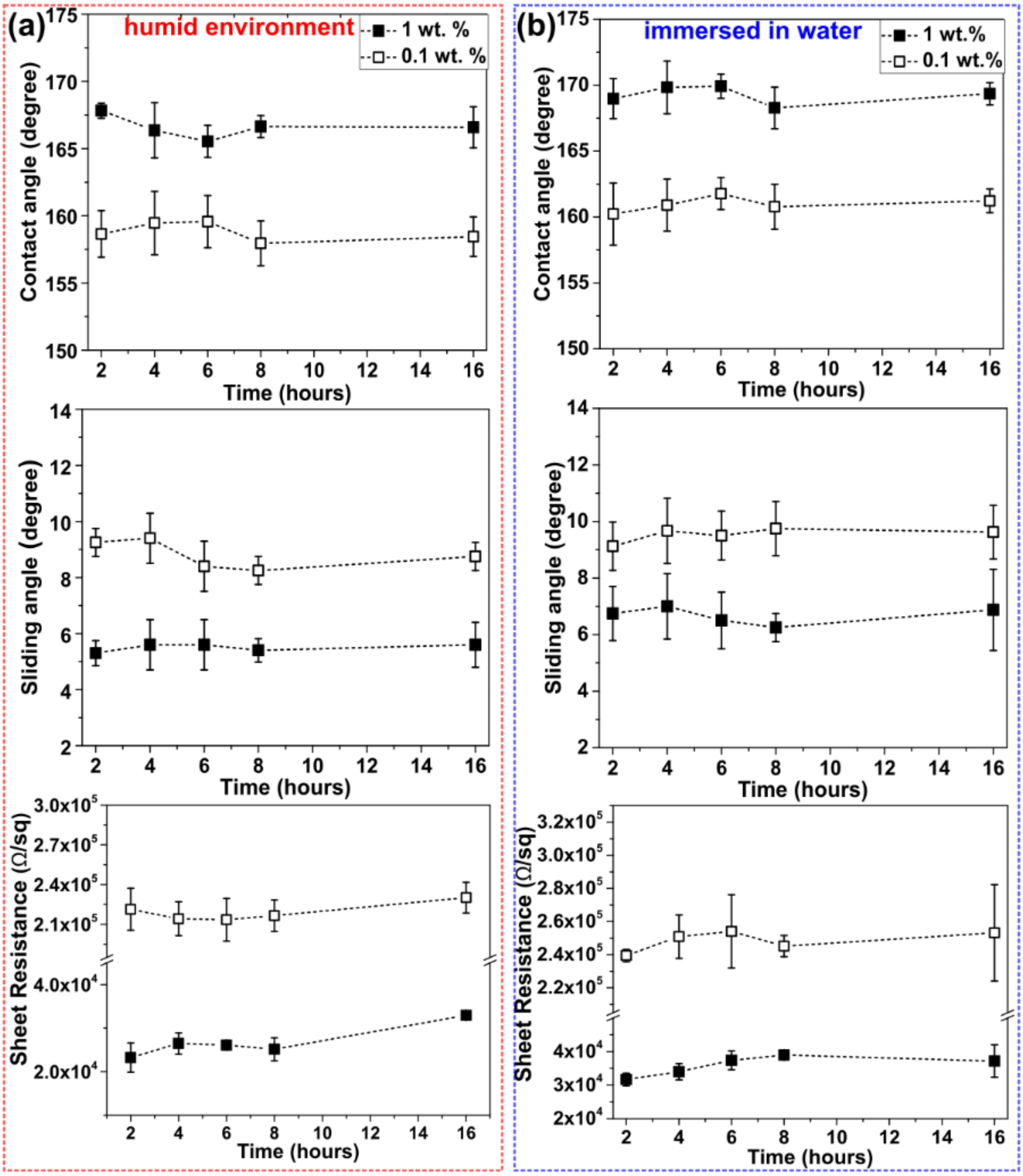

Figure 4.23. Contact angle, sliding angle and sheet resistance of the coatings as a function of exposure time to (a) humid conditions, (b) water immersion. Reprinted with permission from [132]

4.2.7 Chemical durability of the coatings

Other than humid conditions and water immersion, superhydrophobic nature of the coatings should also be preserved in acidic and basic fluids. Often etching of the surface in the presence of acidic or basic liquids results in degradation of hydrophobicity [4]. To check the chemical stability, the coatings prepared with 0.1 and 1 wt. % CNFs were dipped into aqueous solution of acidic and basic nature which were prepared by NaOH and HCl. Substrates were immersed in aqueous pH solutions for the duration of 1, 3, 5 and 7 days followed by washing with Milli-Q® water and drying under the stream of nitrogen. Hydrophobicity of the coatings was checked by measuring contact and sliding angles of water droplets on corresponding surfaces. Figure 4.24a-b illustrate contact and sliding angles of the coatings as a function of immersion time in aqueous pH solutions. The coatings dipped in aqueous acidic solutions of pH 2 exhibited good chemical resistance and remained superhydrophobic even after 7 days of immersion. A small decrease in the contact angle of the coatings was detected after immersion in acidic aqueous solutions (closed squares and circles Figure 4.24a). The sliding angles of water changed considerably after immersion in acidic aqueous solutions. The sliding angles increased for both coatings but the values of sliding angle were below 45° for both coatings after 7 days of dipping in acidic solutions (closed squares and circles Figure 4.24b).

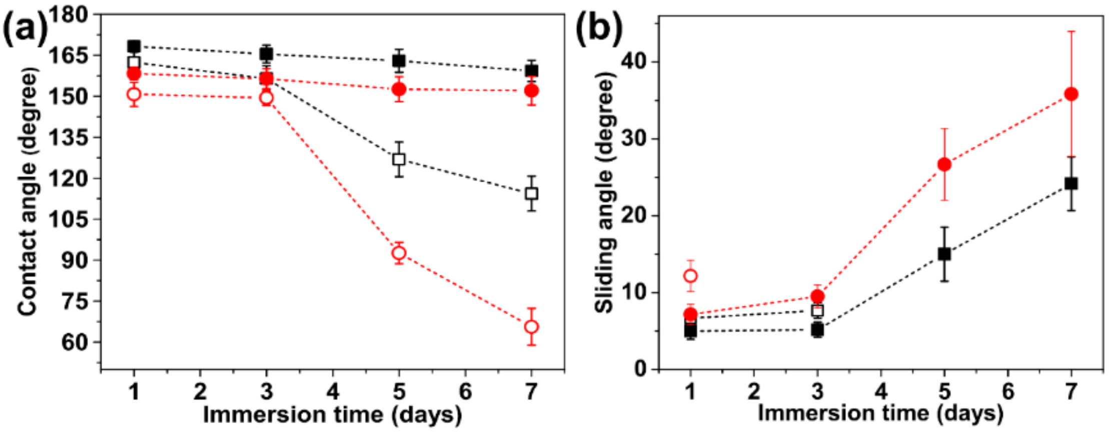

Figure 4.24. (a) Contact angles, (b) sliding angles as a function of immersion time in aqueous pH solutions. ■ 1 wt. % CNFs pH 2, □ 1 wt. % CNFs pH 14, ● 0.1 wt. % CNFs pH 2, ○ 0.1 wt. % CNFs pH 14. Reprinted with permission from [132]

However, the substrates immersed in basic aqueous solutions showed a decrease in contact angle values. The values of contact angles for both coatings changed considerably. For the coatings prepared with 0.1 wt. % the contact angle values decreased from 150.7° ± 4.5° to 65.6° ± 6.7° after 1 and 7 days of immersion respectively (open circles Figure 4.24a). The coatings prepared with 1 wt. % CNFs showed contact angle values of 162.4° ± 3.7° and 114.3° ± 6.4° after 1 and 7 days of immersion (open squares Figure 4.24a). Water droplet sliding was observed at 12.2° ± 2° for 0.1 wt. % CNFs coatings after 1 day of immersion in basic aqueous solutions (open circles Figure 4.24b). Water droplets were pinned at the surface of 0.1 wt. % CNFs coatings after 3, 5 and 7 days of immersion in basic aqueous solutions and did not slide even at inclination angle of 90°. Sliding angles of 6.6° ± 1° and 7.6° ± 1° were detected for 1 wt. % CNFs coatings after 1 and 3 days of immersion in basic aqueous solutions (open square Figure 4.24b). Water droplets were pinned at the substrates immersed for extended duration in basic aqueous solutions (5 and 7 days). The coatings prepared with 0.1 and 1 wt. % were quite stable in acidic aqueous solutions and the surface structure of the coatings remained intact (Figure 4.25a, c). But in basic aqueous solutions etching of the hierarchical structure of nanofilaments was observed after 7 days of immersion (Figure 4.25b, d).

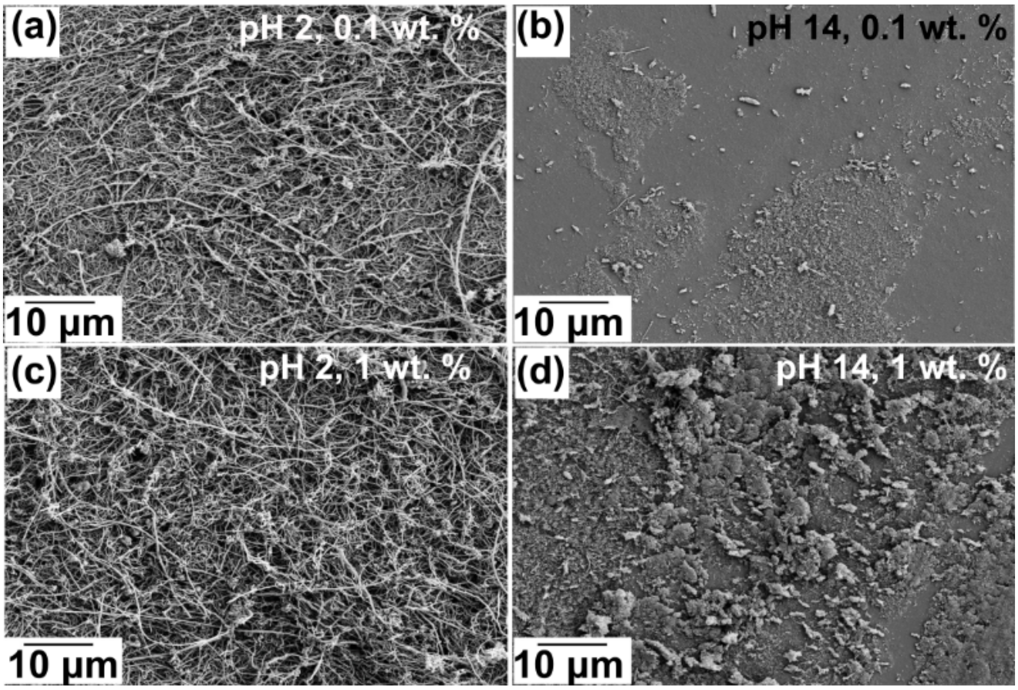

Figure 4.25. SEM image of 0.1 and 1 wt. % CNFs coatings after 7 days of immersion in acidic and basic aqueous solutions. Reprinted with permission from [132]

Multifunctional superhydrophobic/conductive coatings exhibited better resistance to acidic and basic aqueous solutions as compared with SNFs coatings. SNFs coated substrates remained superhydrophobic even after 7 days of immersion in acidic aqueous solution. The water contact angle values of ~150° were observed after 7 days of immersion, while the sliding angle values increased to ~46° (Figure 4.26). SNFs coated substrates dipped in basic aqueous solutions showed poor performance and contact angles decreased sharply. The contact angles decreased from ~25° (1 day of immersion) to ~10° (7 days of immersion). The abrupt decrease in the contact angles of SNFs coatings in basic conditions was due to the instability of polysiloxanes [4] in basic conditions which leads to etching of SNFs in basic environments (Figure 4.27a).

SNFs were still observed after 7 days of immersion in acidic aqueous solutions (Figure 4.27b). CNFs coatings show better chemical stability when compared to only SNFs; in particular basic aqueous solutions (pH 14).

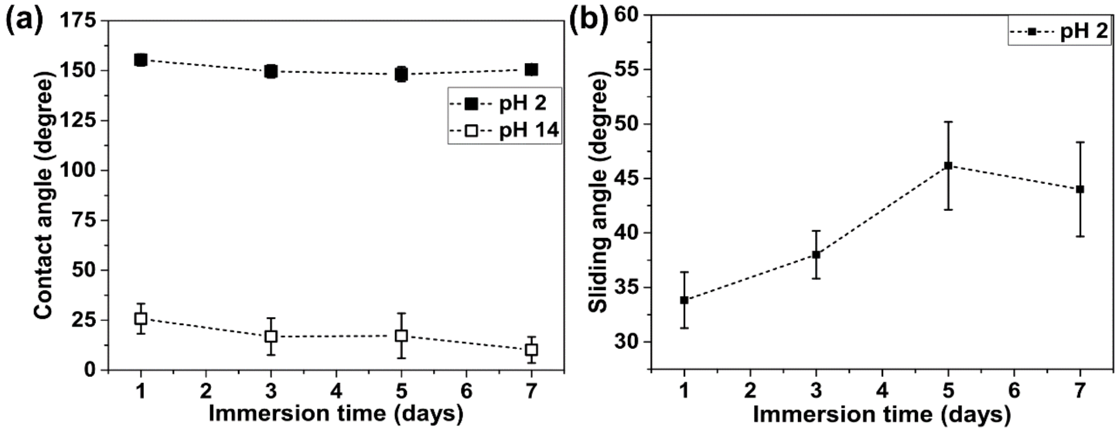

Figure 4.26. (a) Contact angles, (b) sliding angles of SNFs coated substrates as a function of immersion time in acidic and basic aqueous solutions. Reprinted with permission from [132]

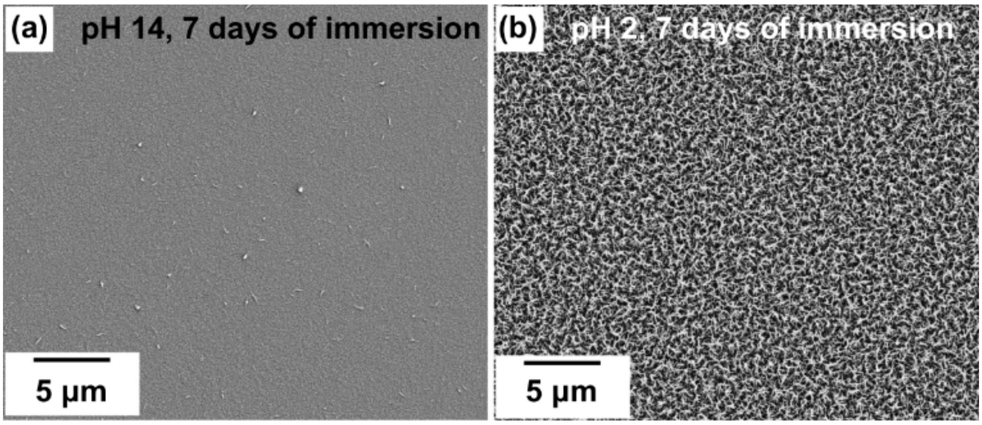

Figure 4.27. SEM image of SNFs coated substrate after 7 days of immersion in (a) basic, (b) acidic aqueous solution. Reprinted with permission from [132]

The stability of multifunctional CNFs coatings can be elucidated by the wetting phenomenon. We assume Cassie-Baxter type wetting phenomenon for SNFs/CNFs coatings [15]. The hierarchical structure generated due to SNFs and CNFs deposition leads to trap of air in the highly rough asperities. Due to the presence of air, the contact area at solid/liquid interface is reduced. The reduction in contact area leads to wetting of very small portion of the surface when dipped in aqueous pH solutions which delays corrosion of the coatings [135]. This layer of air or plastron layer was also observed when the substrates were dipped in aqueous pH solutions.

The multifunctional coatings prepared by the facile method demonstrate better performance and are easy to fabricate as compared with other coatings prepared by the addition of carbonaceous materials. The detailed comparison of the multifunctional coatings with the literature reports is shown in Table 4.1.

Table 4.1. Comparison of multifunctional coatings prepared by carbonaceous materials

Materials	**Processing conditions (method[1], temperature[2], duration[3])**	**Transparency**	**Chemical resistance**		**Reference**
			Water immersion/humid conditions	**Acidic and basic conditions**	
CNFs	Dip coating, 30°C, ~5 hours	Fully to semi-transparent	- Stable to water immersion (16 hours) - Stable in humid conditions (16 hours)	- Stable to acidic solutions (~7 days) - Stable to basic solutions (~3 days)	This work
CNFs	Spray coating, 75°C, 24 hours	Not reported	Not reported	Not reported	[94]
CNFs	Spray coating, 90°C	Not reported	Not reported	Not reported	[136], [137]
Graphite	Spray coating, room temperature, >1 hour	Non-transparent	Not reported	Stable to acidic and basic solutions (~ 24 hours)	[138]
Graphite	Drop casting, 350°C	Not reported	Not reported	Not reported	[122]
Carbon nanocapsu-les	Dip coating, 120°C, ~4 hours	Not reported	Stable in humid conditions (2 hours)	- Stable to acidic solution (~ 2 hours) - Stable to basic solutions (~ few minutes)	[139]
Carbon black	Powder treatment & pellet making, 25-200°C, >24 hours	Not reported	Not reported	Not reported	[140]

---

[1] Method used for fabrication of superhydrophobic/conductive materials

[2] Indicates maximum processing temperature used, it does not include the temperature used for the synthesis of carbonaceous fillers

[3] Indicates total duration for fabrication of superhydrophobic/conductive materials. Does not include the time for the synthesis of carbonaceous fillers

Ketjen black, Graphene, CNT	Molding, >100ºC	Not reported	Not reported	Not reported	[141]
Graphene	Polymer infiltration, 120ºC, ~12 hours	Not reported	Not reported	Not reported	[130]
MWCNT	Filtration, 40ºC, ~12 hours	Not reported	Not reported	Stable to acidic and basic solutions (~ few minutes)	[142]
MWCNT	Screen printing, 250ºC	Not reported	Not reported	Not reported	[143]
MWCNT	Spray coating, 210ºC	Fully to semi-transparent	Not reported	Not reported	[144]
MWCNT	Dip coating, 70ºC, ~90 hours	Fully to semi-transparent	Not reported	Not reported	[145]
MWCNT	Filtration, 60-80ºC, ~24 hours	Not reported	Not reported	Not reported	[146]
MWCNT	Spray coating, 125ºC, >72 hours	Transparent	Not reported	Not reported	[147]
MWCNT	Polymer infiltration, 190ºC	Not reported	- Stable to water immersion (25 hours)	Not reported	[127]
MWCNT	Drop casting, ~80ºC, ~72 hours	Not reported	Not reported	Not reported	[148]
MWCNT	Spray coating, 60ºC, ~48 hours	Non-transparent	Not reported	Not reported	[128]
MWCNT	Spray coating, >60ºC, >65 hours	Fully to semi-transparent	Not reported	Not reported	[149]
MWCNT	Spray coating, room temperature, ~24 hours	Fully to semi-transparent	Not reported	Not reported	[150]
MWCNT	Free radical polymerization, >50ºC, >48 hours	Not reported	Not reported	Stable to acidic and basic solutions (210 days)	[129]
MWCNT	Micro laser texturing, 80ºC, 3 hours	Not reported	Not reported	Not reported	[151]

4.2.8 Mechanical durability of the coatings

Other than chemical resistance, mechanical resistance of the coatings is also very important. The mechanical stability of the coatings was measured in terms of their resistance to abrasion. To check the influence of abrasion on the surface of coatings, contact angle measurements were performed after 5 abrasion cycles. The coatings prepared with 1 wt. % CNFs were tested against abrasion and their comparison was made with the substrates coated with SNFs only. Figure 4.28 shows variation of contact angle as a function of abrasion cycles. Both substrates coated with SNFs and 1 wt. % CNFs illustrated low abrasion resistance and loose superhydrophobicity in just 15 abrasion cycles. The coatings were tested against resistance to abrasion only for 20 cycles. The sharp decrease in superhydrophobic nature of both coatings suggests the damage in the surface structure of the coatings. The coatings when observed by SEM showed loss in the microstructure of the coatings due to the abrasion force. Figure 4.29a-c and Figure 4.29d-f show the surface morphology of SNFs and 1 wt. % CNFs coatings respectively. It is evident from SEM observation that due to their low mechanical stability the coatings abrade from the surface. The conductive nature of the coatings was also tested by measuring the sheet resistance after abrasion. But the coatings loose conductive property just after 5 cycles and do not remain electrically conductive. The low mechanical resistance of the coatings could be because of poor mechanical stability of SNFs and weak van der walls forces present between SNFs and CNFs.

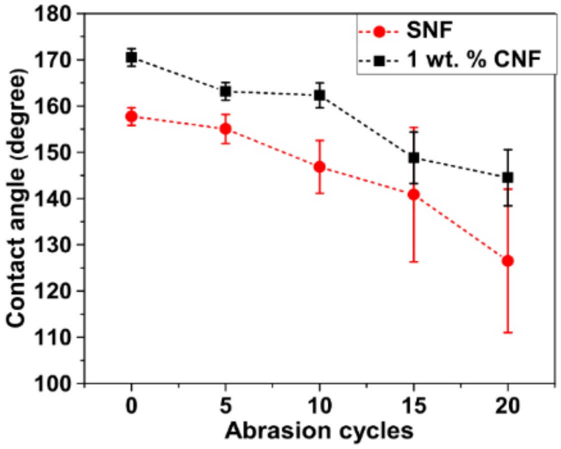

Figure 4.28. Contact angles as function of abrasion cycles observed on SNFs and 1 wt. % CNFs coated substrates. Reprinted with permission from [132]

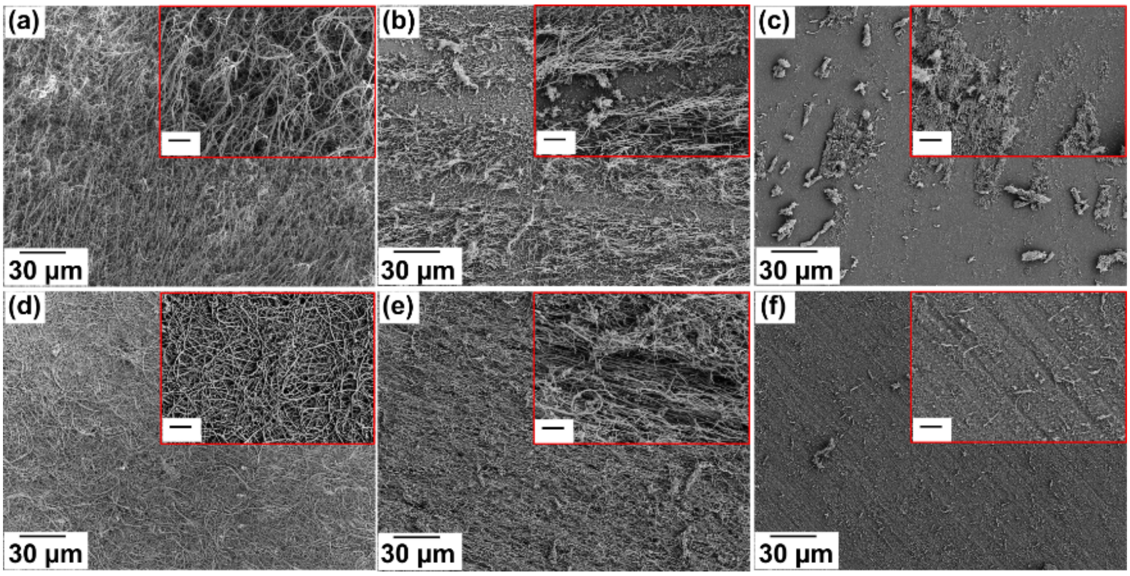

Figure 4.29. SEM image of SNFs coated substrates (a) before abrasion, (b) after 10 cycles, (c) after 20 cycles, SEM images of CNFs coated substrates (d) before abrasion, (e) after 10 cycles, (f) after 20 cycles. Insets scale bar is 5 µm. Reprinted with permission from [132]

One method to improve the mechanical stability of the coatings could be the use of polymer additive. The polymers bind effectively with hydrophobic functional groups. As SNFs have hydrophobic alkyl functional groups, the polymer may bind with hydrophobic network of SNFs and increase its mechanical durability. To confirm this, adaptation of a procedure was made which was reported by Mates et al [94]. Parafilm-M (PF) which is the most commonly used polymer in the labs was dissolved in toluene at 50°. Stirring was performed to completely dissolve PF in toluene. The prepared PF solution was mixed with CNFs suspension to yield a stable dispersion with 0.5, 0.6, 0.7, 0.8 and 0.9 wt. % PF in the final dispersion. The details of the procedure are reported in experimental part. SNFs coated substrates were dip coated in the prepared PF dispersions followed by washing with toluene and Milli-Q® water and drying in nitrogen stream. The characterization of the prepared substrates was performed using SEM, contact angle measurements and 4 probe method. Figure 4.30 shows the SEM images of the coatings prepared with addition of 0.5, 0.6, 0.7, 0.8 and 0.9 wt. % PF. The contact angles measured on corresponding coatings are presented as insets which show the superhydrophobic nature of the coatings. Due to the increase in the amount of PF in the dispersion, aggregates and agglomerates were also observed at the surface. EDX analysis of the aggregates showed they were only composed of PF and CNFs (Figure 4.31).

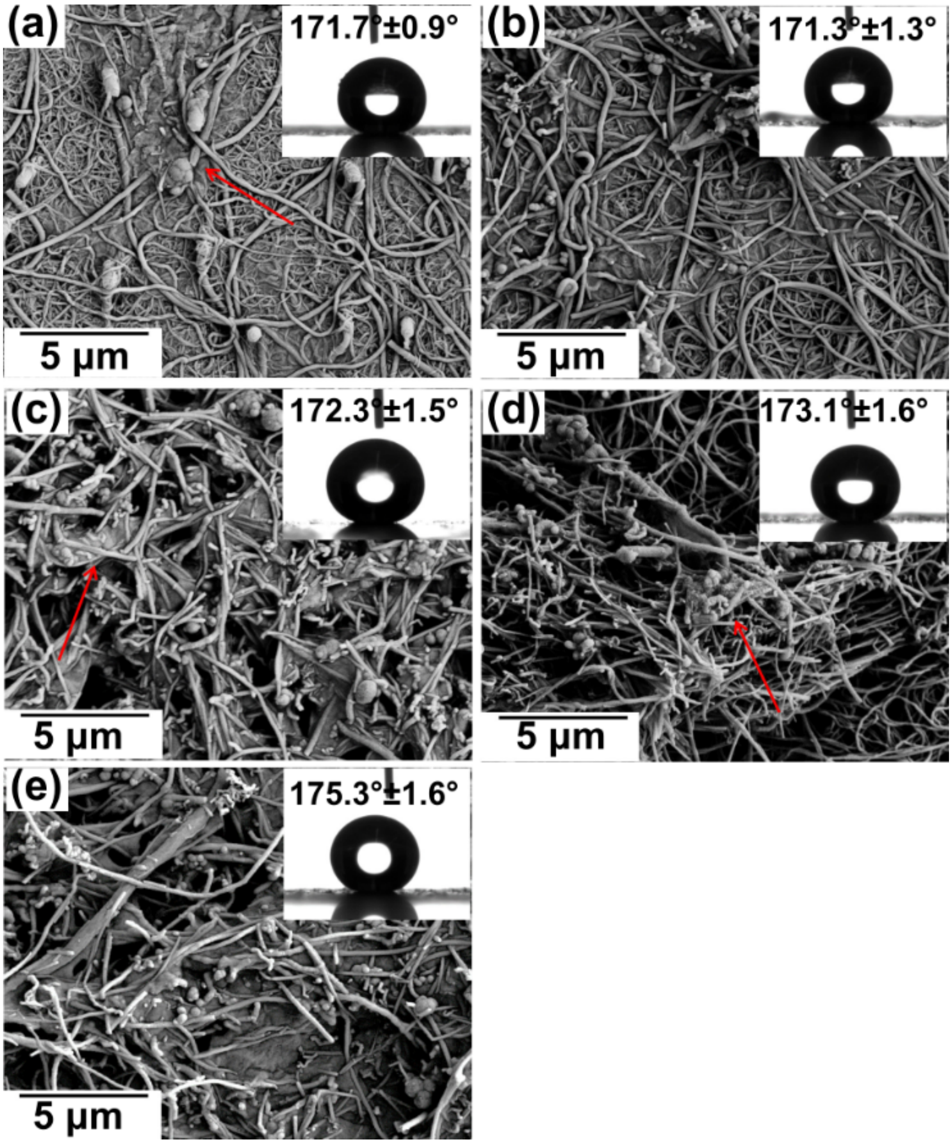

Figure 4.30. SEM images of the coatings prepared with (a) 0.5, (b) 0.6, (c) 0.7, (d) 0.8 and (e) 0.9 wt. % PF. The contact angles measured on corresponding surfaces are shown as inset. The arrows indicate the presence of agglomerates. Reprinted with permission from [132]

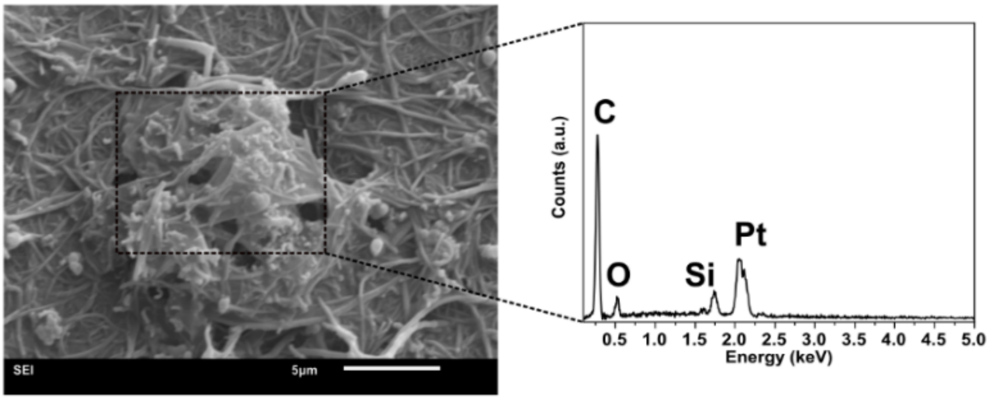

Figure 4.31. SEM image of the aggregates and EDX spectra of indicated region

The characterization of the coatings using 4 probe method revealed the conductive nature of the prepared coatings. Interestingly the sheet resistance decreased as a function of PF content (Figure 4.32a). The characterization of superhydrophobicity of the coatings revealed high value of contact angles and low sliding angle values. Figure 4.32b shows contact and sliding angles of the coatings prepared with addition of PF. The decrease in sheet resistance could be attributed to the good binding of CNFs with SNFs network due to the addition of PF which leads to increase in the thickness of the prepared coatings which in turn reduces the sheet resistance. The cross-sectional view of the coating prepared with 0.9 wt. % PF as compared with SNFs coating is shown in Figure 4.33. The thickness of the coating prepared with 0.9 wt. % PF is higher than 1 wt. % CNFs coating (Figure 4.33 & Figure 4.16). However, in contrary to the coatings prepared without PF, the addition of PF resulted in the loss of transparency of the coatings.

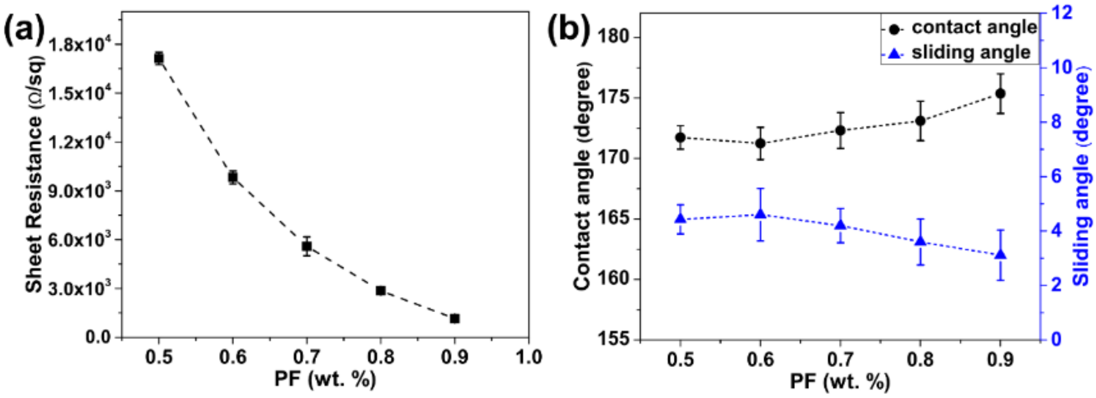

Figure 4.32. (a) Sheet resistance, (b) contact and sliding angles as a function of PF content. Reprinted with permission from [132]

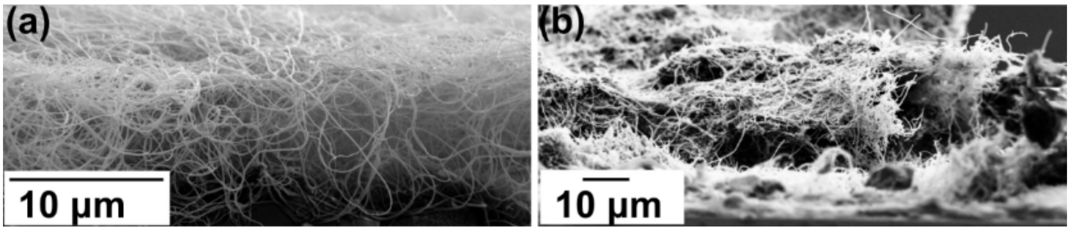

Figure 4.33. Cross-sectional view of (a) SNFs, (b) 0.9 wt. % PF coating. Reprinted with permission from [132]

The coatings prepared with maximum amount of PF were tested against abrasion force. Contact angle measurements of the coatings as a function of abrasion cycles is presented in Figure 4.34a. The addition of PF to the coatings increased the mechanical stability of the coatings and the coatings remained superhydrophobic in nature up to 35 cycles of abrasion. The values of contact angles decreased as a function of abrasion cycles and coatings transformed from superhydrophobic to hydrophobic after 50 abrasion cycles. Water droplet sliding was not observed for any of the coatings after abrasion. The coatings prepared with the addition of PF improved the mechanical stability when compared to the coatings prepared without PF which lost superhydrophobicity after 15 abrasion cycles. The improvement in mechanical durability resulted in retaining the conductive nature of the coatings. The coatings remained conductive even after 50 abrasion cycles. However, a decrease in conductivity (increase in sheet resistance) as a function of abrasion cycles was observed which is because of the wear of conductive CNFs from the surface under the abrasion force (Figure 4.34b). Wear of the coatings because of abrasion was also observed under SEM which explains the decrease in the conductivity of the coatings. The removal of coating layers from the surface under the influence of abrasion can be seen in Figure 4.35 where the damaged regions are highlighted by red lines. The damage in the surface morphology of the coatings under strong abrasion force also explains the sticking of water droplets at the surface of coatings subjected to abrasion tests.

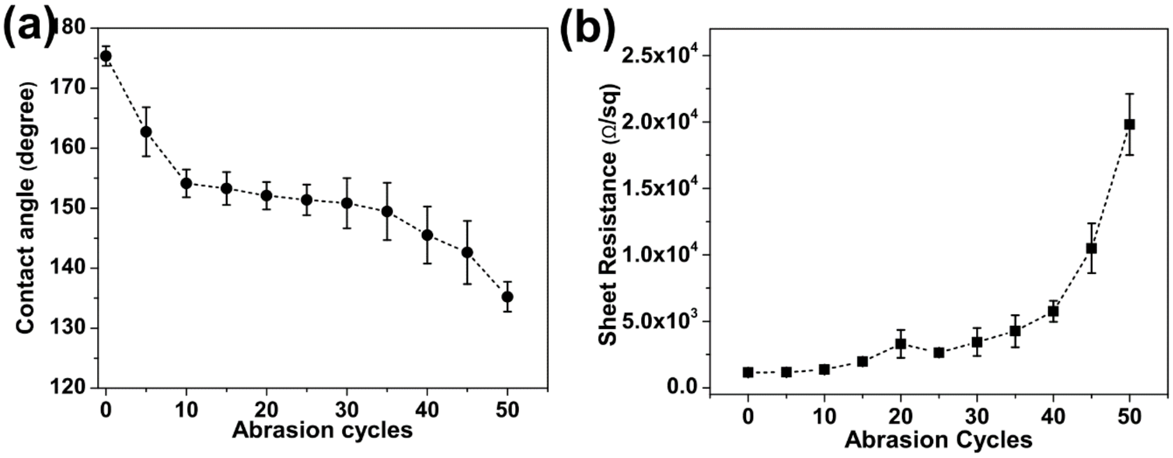

Figure 4.34. (a) Contact angle, (b) sheet resistance as a function of abrasion cycles. The coatings prepared with 0.9 wt. % PF. Reprinted with permission from [132]

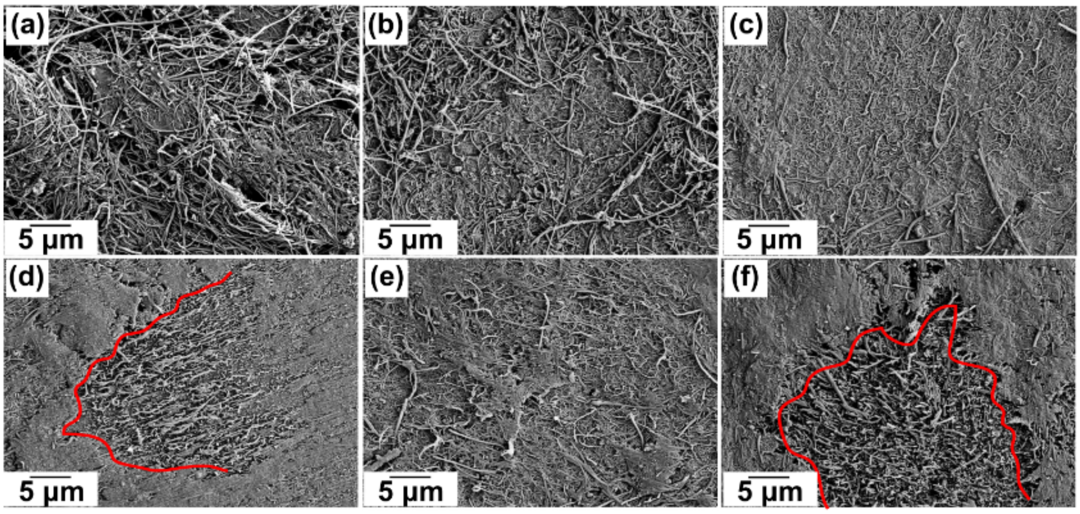

Figure 4.35. SEM images of the coatings (a) before abrasion, after (b) 10, (c) 20, (d) 30, (e) 40 and (f) 50 abrasion cycles. The coatings prepared with 0.9 wt. % PF. The red lines indicate the abraded regions. Reprinted with permission from [132]

The fabrication of multifunctional coatings using SNFs and CNFs by the facile DAGS chemistry and dip coating is a very economical, and fast method which does not involve complicated instrumentation or complex experimental set up. Furthermore, the DAGS method can be applied to a broad range of substrates to synthesize SNFs. Combining an efficient synthesis method with one-step dip coating multifunctional coatings can be fabricated which possess excellent resistance to extreme weather conditions as well as stability against aqueous liquids of varying pH. This synthesis strategy when compared to already reported studies in the literature (as presented in Table 4.1) show the prepared multifunctional coatings involve inexpensive and time efficient method to yield superior coatings than published research.

4.3 Chemical vapor deposition of Germanium oxide nanofilaments

The functionality of a material does not only depend on its chemical and inherent physical properties, but also on its shape and size. Especially, materials with dimensions in the range of nanometers often exhibit significantly different properties than objects of the same material but with micro- or macro dimensions. Therefore, nanometer size materials may possess unique mechanical, optical, electronic and magnetic properties as compared to their bulk counterparts. The key to tailor the properties and functionality of materials is to control the fabrication of materials. Bottom-up techniques for the fabrication of nanomaterials are of particular interest because of: (i) their application to a wide range of materials; (ii) the ability to achieve high structural variation; and (iii) control on the material's interfaces during nanofabrication.

1D nanomaterials in the form of nanowires, nanotube or nanofilaments are an example of materials fabricated using bottom-up techniques. These 1D nanomaterials have found useful applications in the areas of optoelectronics [152], nano-electronics [153], batteries [154], lasers [155] and surface science [156] owing to their high aspect ratio. In situ shaping of nanomaterials is rather less known and most common method for in situ shaping of 1D nanomaterials is vapor-liquid-solid (VLS) mechanism [157]. Various types of 1D nanomaterials have been synthesized using VLS mechanism. However, VLS methods often require metal catalyst particles as a template for the growth of 1D nanostructures and application of high temperature processing which yields in highly expensive and sophisticated instrumentation [158] [159]. An alternative to VLS method which does not require high temperature processing or use of sophisticated equipment, would be a preferable and economical approach. Such an approach which involves room temperature processing has been used for over a decade for the synthesis of 1D nanomaterials of silicone called silicone nanofilaments (SNFs) [1]. This method is based on Droplet Assisted Growth and Shaping (DAGS) which involves water droplets with nanometer size for shaping. These nano-droplets of water serve as reaction vessels for polymerization reactions of precursor molecules [84]. The benefits of DAGS process involve: (i) application of ambient pressure and room temperature processing, (ii) no liquid waste production as reaction is carried out in gas phase, and (iii) easy scale-up [3]. SNFs synthesized by the DAGS method have aspect ratios in the range of 200-1000 or even >1000, and they have been found to be superhydrophobic in nature with excellent chemical and thermal stability [6]. After successful application of the DAGS method for silicone nanomaterials, we have extended it to non-silicone materials such as germanium oxide.

Synthesis of 1D nanomaterials of germanium oxides by the DAGS method is an important breakthrough. 1D germanium oxides are of significant importance for opto-electronic devices due to their wideband gap and high refractive index [160] [161]. In addition, germanium oxides possess unique photo-luminescence properties [162]. Usually 1D germanium oxide nanomaterials are synthesized by various methods such as laser ablation [163], physical vapor evaporation [161], carbothermal reactions [164], and carbon nanotube confined reactions [165]. All of the above mentioned methods involve application of high temperature, catalyst support or complicated procedures which make the process cost intensive. The synthesis of 1D germanium oxide nanofilaments by the DAGS chemistry is a novel and straightforward method which involves ambient temperature and pressure conditions. The DAGS method of synthesis is very facile, involves gas phase and does not require complicated equipment.

4.3.1 Synthesis of germanium oxide nanofilaments

For the synthesis of germanium oxide nanofilaments (GNFs) by chemical vapor deposition (CVD) using DAGS chemistry, the following procedure was used. Cleaned and oxygen plasma activated glass substrates were placed in the coating chamber (glass desiccator). The humidity inside the coating chamber was maintained at the values of 35% ± 2% by flushing dry and humidified nitrogen for the duration of 1 hour. The values of relative humidity inside the coating chamber were monitored using EE23 hygrometer (E+E Elektronik). $GeCl_4$ was injected into the coating chamber with the help of a syringe and reaction was carried out for the duration of overnight at room temperature. The schematics of the synthesis procedure are shown in Figure 4.36, while the details of the synthesis procedure are described in experimental section.

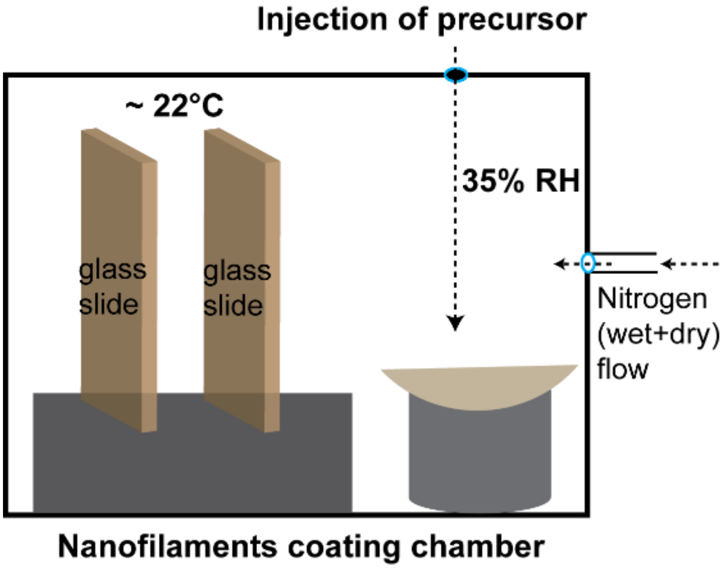

Figure 4.36. Schematics of coating procedure for the synthesis of GNFs by CVD. Reprinted with permission from [80]

The volatile germanium tetrachloride reacted with water present inside the coating chamber to yield hydrochloric acid and germanium hydroxide. Further condensation of germanium hydroxide led to the GNFs formation. The analysis of the substrates was performed under SEM which revealed the presence of dense and homogenous formation of GNFs on the substrate. Figure 4.37 show SEM images of GNFs performed at low and high magnification. SEM observation showed the presence of highly dense and highly entangled GNFs on the substrate which were 1-10 µm long.

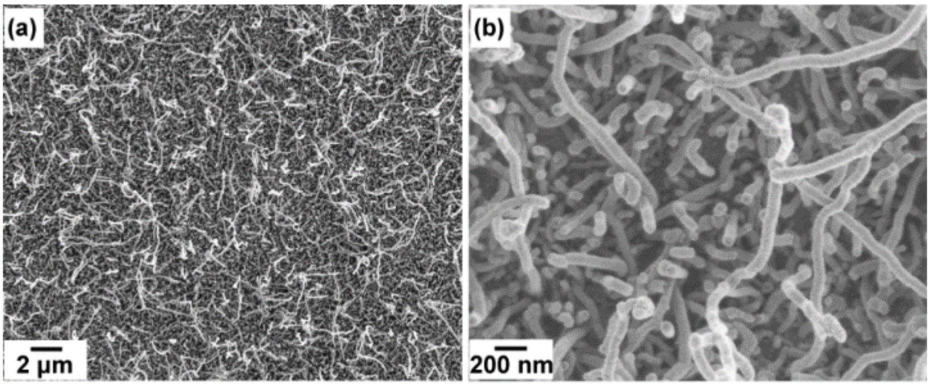

Figure 4.37. SEM images of as synthesized GNFs (a) low and (b) high magnification. Reprinted with permission from [80]

GNFs were also observed by TEM which revealed homogenous nature of GNFs (Figure 4.38a). To check whether GNFs were crystalline or amorphous in nature, selected area electron diffraction (SAED) analysis was performed at TEM which revealed the nanofilaments were amorphous in nature and did not show any diffraction pattern (Figure 4.38a inset). EDX analysis of GNFs was also performed to check the chemical composition of nanofilaments, the elemental mapping of nanofilaments shown in Figure 4.38a showed the homogenous distribution of Ge and O inside the nanofilaments. The overall EDX spectra of the maps is shown in Figure 4.38b which showed the presence of Ge, O, C and Cu. The signals from C and Cu were originated from carbon film underneath the TEM grid and Cu TEM grid respectively. EDX analysis confirmed the GNFs were only composed of two components i.e. Ge and O. The size (diameter) distribution of GNFs was calculated by measuring the diameter of at least 100 GNFs mid-sections. SEM images of GNFs were used for this purpose and size of GNFs was calculated using ImageJ® software.

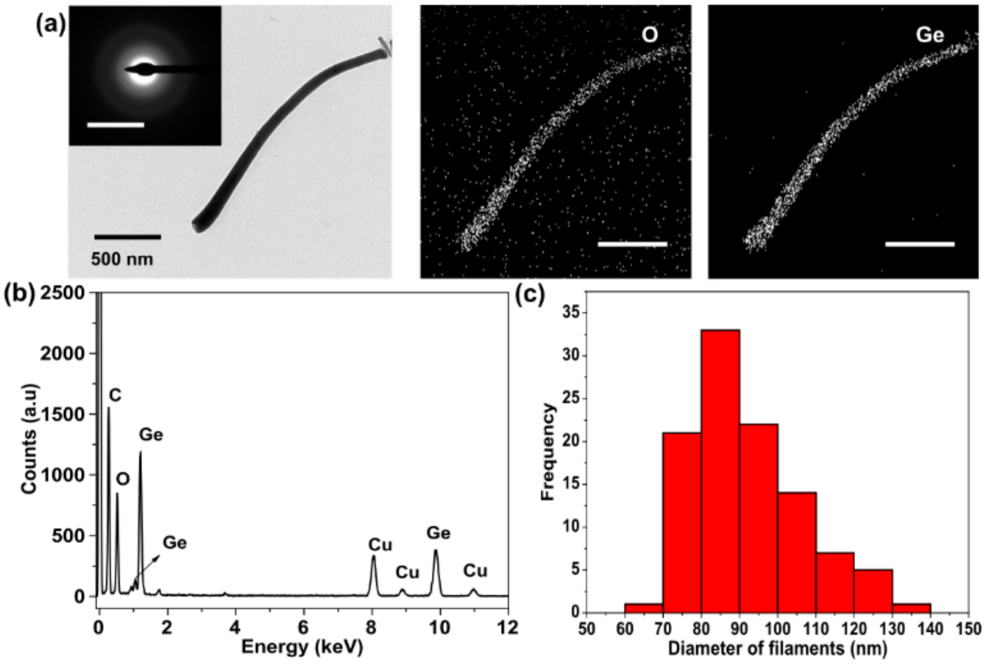

Figure 4.38. GNFs under TEM (a) TEM imaging of GNFs (SAED image as inset, inset scale 25 1/nm), EDX elemental mapping of GNFs (scale bar of maps 500 nm), (b) EDX spectra of corresponding map, (c) size distribution of nanofilaments. Reprinted with permission from [80]

The characterization of GNFs was made using FTIR and its comparison with the bare glass substrate is shown in Figure 4.39. The substrate coated with GNFs showed stretching vibrations around 850 cm^{-1} and 963 cm^{-1} which indicate the presence of G-O bonds [166] [167]. The strong signals from Si-O-Si were also observed at 750 cm^{-1} and 910 cm^{-1} which originate from the glass substrate. The wide peaks at 1600 cm^{-1} and 3600 cm^{-1} were also observed which show the presence of hydroxyl (-OH) groups on the surface. In addition to FTIR, the characterization of GNFs was also made by XPS. Spectra of Ge 3d peak originated from GNFs is presented in Figure 4.40. It is designated as experimental peak with binding energy of 32.9 eV which showed the oxidation state of Ge >0 [168]. The spectral fitting of experimental peak showed it was composed of two peaks. One peak had the binding energy of 31.6 ± 0.5 eV and the other had 32.9 ± 0.3 eV binding energy. The small peak with less binding energy (31.6 eV) can be assigned to GeO (Ge^{2+}) [169] [170], while the peak with higher binding energy (32.9 eV) was assigned to GeO_2 (Ge^{4+}) [169] [170]. Characterization of GNFs by XPS revealed that nanofilaments consisted of germanium oxide which existed in two oxidation states.

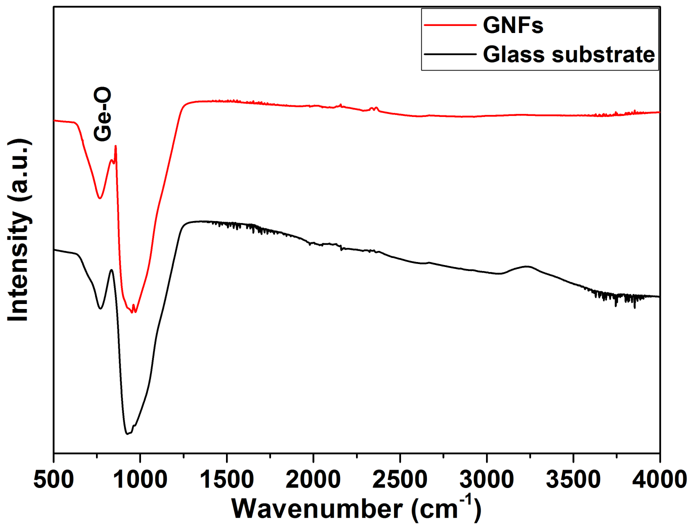

Figure 4.39. FTIR spectra of GNFs and glass substrate. Reprinted with permission from [80]

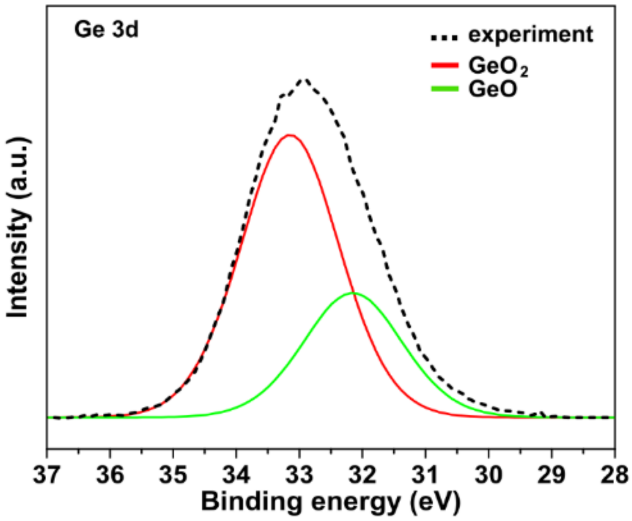

Figure 4.40. XPS spectra of GNFs showing Ge 3d peak. Spectra fitting of Ge 3d speak showing presence of two additional peaks. Reprinted with permission from [80]

4.3.2 DAGS mechanism and influence of humidity on GNFs synthesis

Synthesis of nanofilaments is highly dependent on the level of humidity present in the coating chamber. To study the effect of humidity on the synthesis of GNFs, synthesis was performed at relative humidity levels of 15% ± 1%, 30% ± 1%, 35% ± 1%, 40% ± 1%, 50% ± 1%, 70% ± 1%. All reactions were carried out for overnight duration. The successful growth of GNFs on the substrates was observed at 30% (n_{water}=2.3 mmoles), 35% (n_{water}=2.7 mmoles), and 40% (n_{water}=3.08 mmoles) relative humidity levels. Particulates or aggregated structures were observed at RH levels of 15% (n_{water}=1.1 mmoles), 50% (n_{water}=3.85 mmoles) and 70%

(n_{water}=5.4 mmoles). SEM images of the substrates after carrying out syntheses at different humidity are shown in Figure 4.41.

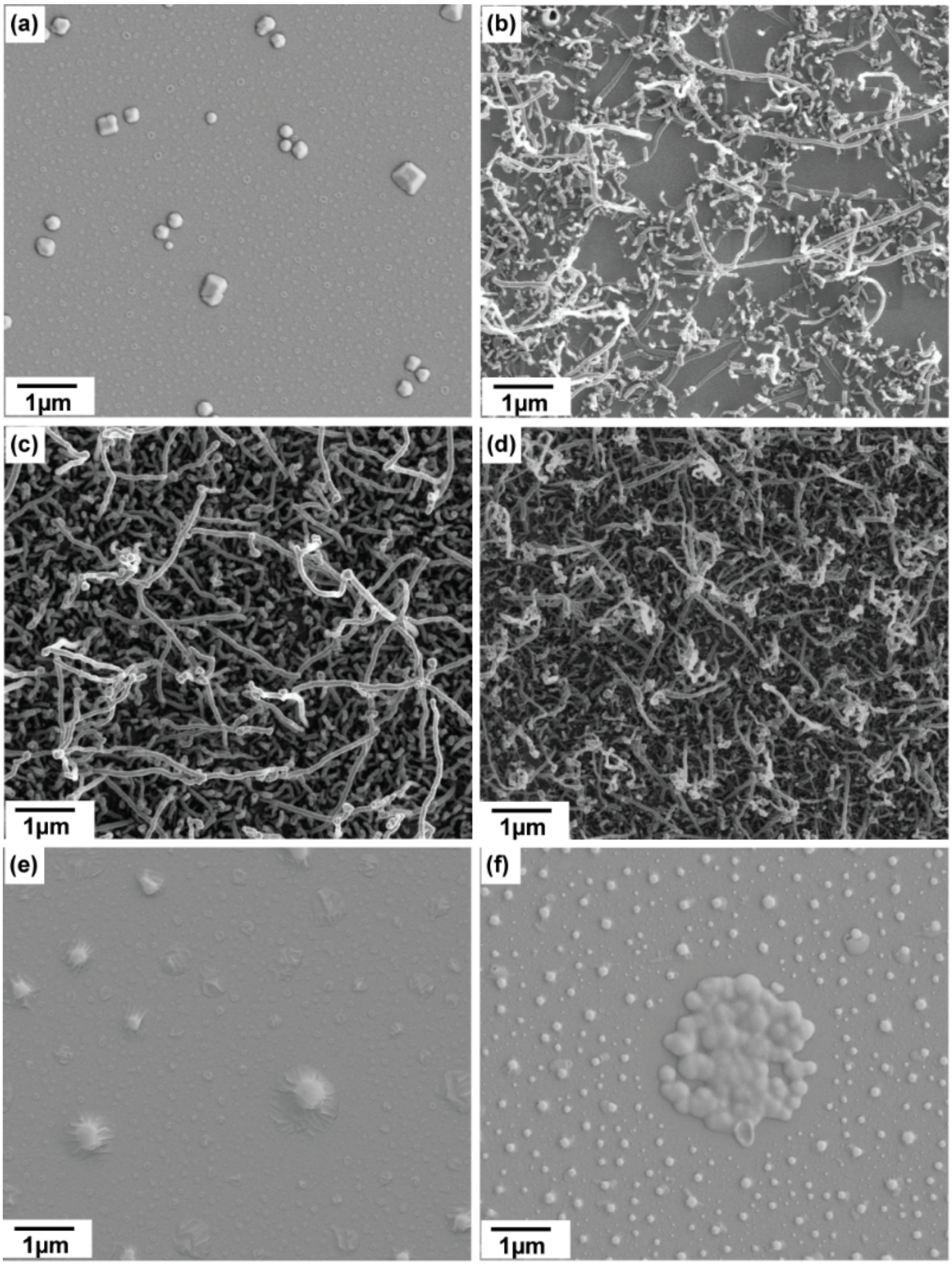

Figure 4.41. SEM images of the substrates after synthesis at (a) 15%, (b) 30%, (c) 35%, (d) 40%, (e) 50% and (f) 70% relative humidity. 8.7 mmoles of $GeCl_4$ used for all syntheses. Reprinted with permission from [80]

The synthesis of GNFs is quite similar to SNFs which have been synthesized using same reaction principle [1]. The growth of both types of nanofilaments i.e. GNFs and SNFs follow the DAGS mechanism [84]. The schematics of DAGS applied to germanium system are shown in Figure 4.42. After placing the substrates in humid conditions very small islands of water (water droplets) are formed at the surface of substrates (Figure 4.42a). The formation of water islands at the surface instead of thin and homogenous layers is due to the heterogeneity in the nature of the substrate. Inhomogeneous surface structure or chemical composition of the surface leads to heterogeneity in the nature of the substrate [92]. In addition to surface roughness and chemical composition, relative humidity also plays a crucial role in water droplet formation [84]. The water droplets formed at the surface act as reactors with confined volumes. When germanium tetrachloride is injected into the coating chamber, it vaporizes due to its high vapor pressure (VP= 69 mm Hg). The vapors of germanium tetrachloride react with water droplets to yield germanium hydroxide and hydrochloric acid (Figure 4.42b). The as formed HCl is water soluble and plays the role of a catalyst. Due to the further hydrolysis of germanium tetrachloride, more germanium hydroxide moieties are formed. Due to the presence of HCl, hydrolysis and condensation reactions proceed and germanium hydroxides undergo condensation reactions to produce germanium oxide (Figure 4.42c). The presence of HCl, germanium hydroxide and germanium oxide in the water droplet reduces the activity of water droplet. When the activity of water droplets drops below the surrounding humidity, water molecules from the surrounding gas are supplied to carry out hydrolysis and condensation reactions. The as formed germanium oxide is deposited at the solid-liquid interface due to its less solubility in water droplets and grows in one dimension (Figure 4.42c-d).

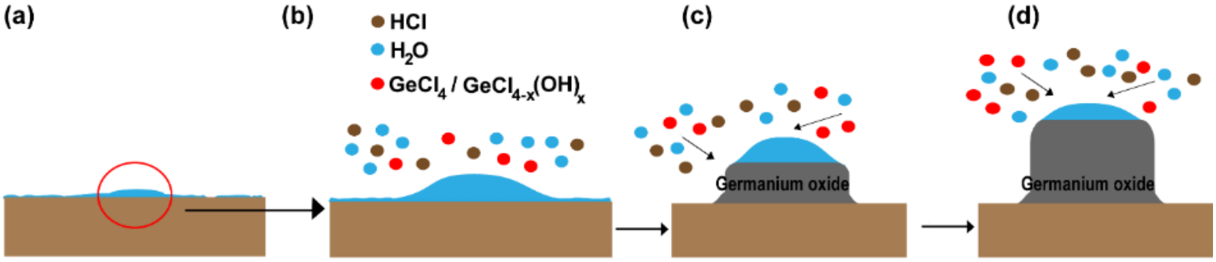

Figure 4.42. DAGS mechanism for the synthesis of GNFs. Reprinted with permission from [80]

When the relative humidity is very low (<15%), the sufficient hydrolysis of germanium tetrachloride does not take place to sustain the reaction. As a consequence, only few particulate structures grow instead of filament growth. While at high relative humidity i.e. 50% or 70% highly abundant water present in the coating chamber results in the formation of thin water layer at the surface of the substrate which results in rapid and uncontrolled hydrolysis of germanium tetrachloride. This uncontrolled hydrolysis yield in formation of particles or aggregates as observed in Figure 4.41e-f.

4.3.3 Time dependent growth of GNFs

The time dependent growth of GNFs was studied by performing the synthesis for varying duration and observing the substrates under SEM. The reactions for growth studies were carried out for the duration of 1 hour, 2 hours, 4 hours and overnight duration. SEM images of the substrates after different reaction times are shown in Figure 4.43. Very few island or particulate structures were observed after 1 hour of reaction (Figure 4.43a). Filaments growth from the island structures was observed after 2 hours of reaction (Figure 4.43b). With the increase in reaction time, more filament structures were observed at the surface (Figure 4.43c). Eventually, after overnight reaction homogenous and dense growth of GNFs was observed (Figure 4.43d).

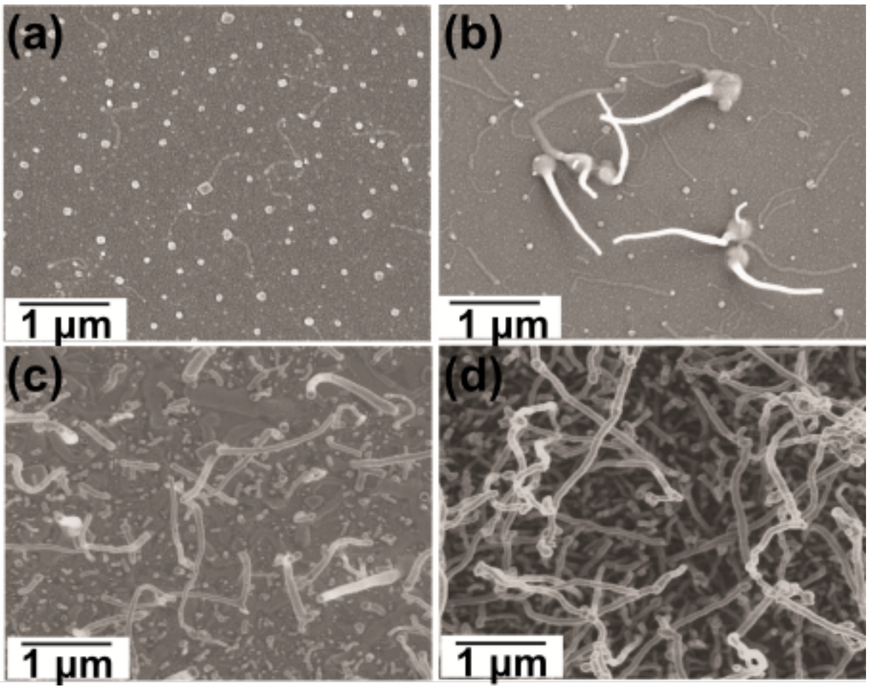

Figure 4.43. SEM images of substrates after (a) 1 hour, (b) 2 hours, (c) 4 hours, (d) overnight reactions. Reprinted with permission from Wiley [80]

The morphology of GNFs is comparable to SNFs in terms of size (length and diameter), but the growth kinetics of GNFs are noticeably slow. In earlier studies reporting the growth kinetics of SNFs, homogenous and dense growth of SNFs was observed just after 20 minutes of precursor trichloromethylsilane (TCMS) introduction [171]. The slower growth kinetics of GNFs could be explained by observing the reaction principle. As the reaction in both cases is carried out in the gas phase and reaction proceeds by the evaporation of precursors in the gas phase, so the vapor pressure of the precursor plays an important role. Precursors which high vapor pressure vaporize fast as compared with precursors with low vapor pressure. The fast evaporation of a precursor which hydrolyses to produce monomers undergoing condensation to yield in formation of filaments is highly dependent on the vapor pressure of the precursor. As germanium tetrachloride has a vapor pressure of (VP= 69 mm Hg) at room temperature and trichloromethylsilane has a vapor pressure of (VP= 150 mm Hg), the growth kinetics of GNFs are supposedly slower than SNFs. It is evident from the experiment where we have used phenyltrichlorogermane as a precursor for the synthesis of GNFs but it did not yield successful growth of filaments due to its low vapor pressure (VP= 0.1 ± 0.4 mm Hg). We observed only particles on the substrate after overnight reaction (Figure 4.44) and we could still find some liquid precursor inside the coating chamber after the reaction.

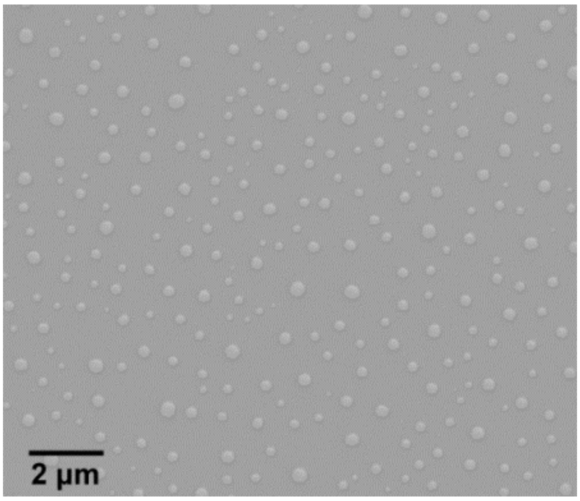

Figure 4.44. Synthesis performed using phenyltrichlorogermane. Reprinted with permission from [80]

4.3.4 Thermal stability of GNFs

Thermal stability of GNFs was checked by annealing the substrates coated with GNFs. The substrates were annealed in air at 300°C, 400°C, 500°C, 600°C for the duration of 4 hours followed by cooling inside the furnace. Subsequently, the substrates were investigated by SEM. The nanofilaments were stable up to 500°C but degradation of nanostructures was observed at 600°C (Figure 4.45). The decomposition of GNFs at high temperatures suggests the presence of less thermally stable phase which results in degradation of GNFs. XPS analysis of GNFs shown in Figure 4.40 showed they were composed of GeO and GeO_2. GeO is known to be thermally unstable [172] and vaporizes at comparably lower temperature than GeO_2 which also explains the low thermal stability of GNFs. To check the influence of annealing on the morphology or amorphous nature of GNFs, TEM and SAED analyses of GNFs were performed. We did not observe any change in the morphology or amorphous nature of GNFs after annealing (Figure 4.46, Figure 4.47, and Figure 4.48).

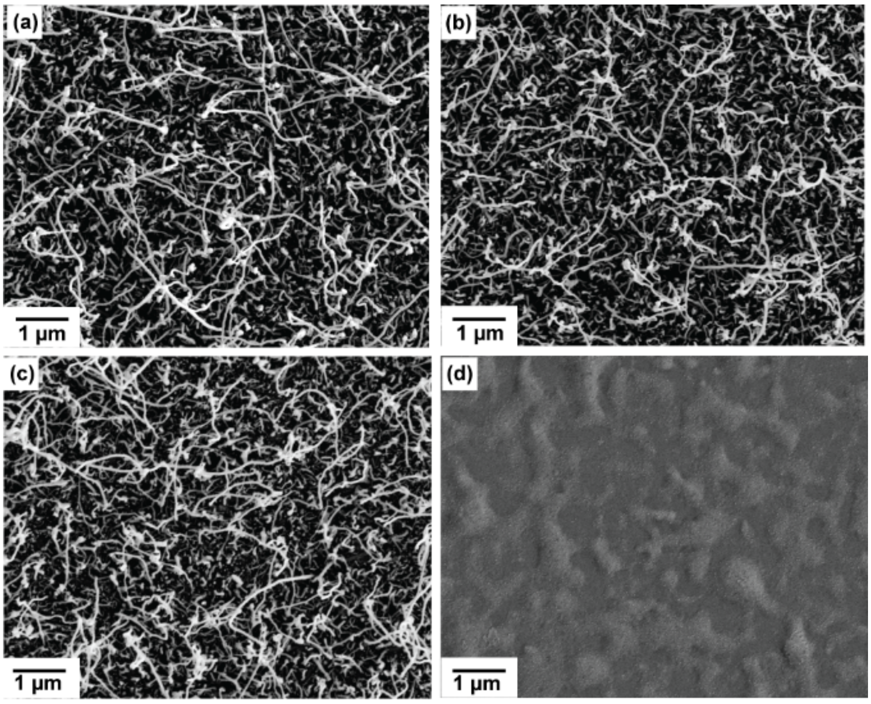

Figure 4.45. SEM images of GNFs after annealing at (a) 300ºC, (b) 400ºC, (c) 500ºC, (d) 600ºC

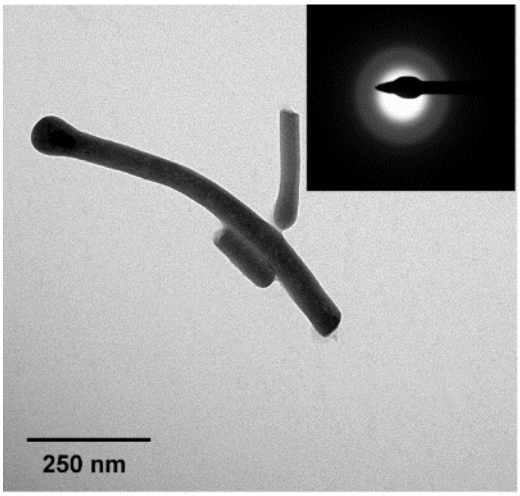

Figure 4.46. TEM image of GNFs after annealing at 300ºC, inset shows SAED image

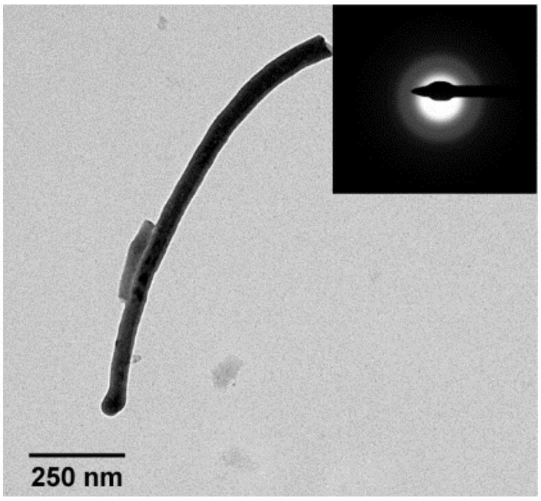

Figure 4.47. TEM image of GNFs after annealing at 400ºC, inset shows SAED image

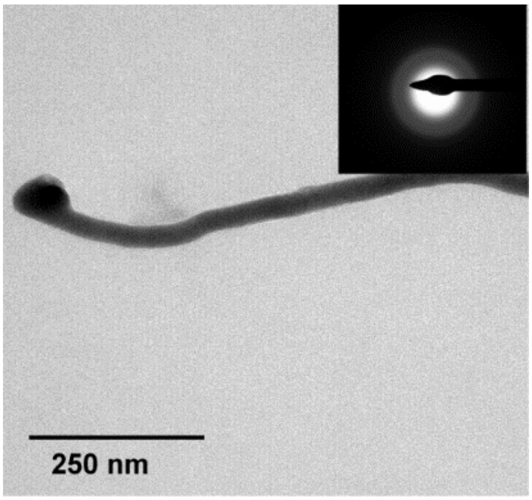

Figure 4.48. TEM image of GNFs after annealing at 500ºC, inset shows SAED image

4.3.5 Photoluminescence spectra of GNFs

GNFs which are essentially composed of germanium oxide can be of potential use in optical devices such as optical wave guides due to intrinsic dielectric nature of germanium oxide. Especially, the one dimensional germanium oxides in the shape of wires or filaments may be found useful for 1D optoelectronic devices due to their photoluminescence in ultraviolet and blue region. To check the photoluminescence of GNFs Fluorolog® spectrometer was used. The source for excitation was Xenon laser with the excitation wavelength of 314 nm. The peaks from GNFs were observed at 370 nm and 444 nm illustrating the emission in ultraviolet and light blue regions (Figure 4.49). The ultraviolet and light blue emission are known for germanium oxide materials. These emissions are assigned to oxygen deficient luminescence centres and germanium-oxygen vacancies [164] [167] [173].

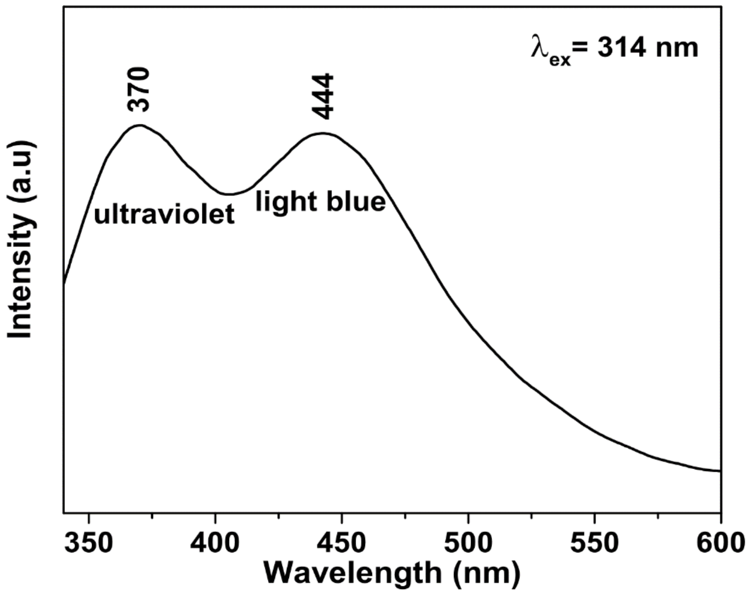

Figure 4.49. Photoluminescence spectra of GNFs. Reprinted with permission from [80]

4.3.6 Application of GNFs for superhydrophobicity

The highly entangled network of 1D GNFs can be useful for applications where high surface roughness is of significant importance. For instance, the surface roughness and surface chemistry play a vital role in superhydrophobicity and self-cleaning applications. GNFs which provide high surface roughness are hydrophilic in nature, changing the surface chemistry of GNFs by hydrophobic molecules can induces hydrophobicity to the surface. To confirm this the surface of GNFs was treated with trichloromethylsilane molecules to make a superhydrophobic structure. The change in surface properties was observed using contact angle measurements. A substantial difference in contact angle of GNFs before and after silane treatment was observed. The water contact angle values of 0° were observed on un-treated GNFs (superhydrophilic), while contact angle of 155.6° ± 2.4° was observed on silane treated GNFs. SEM images of GNFs before and after silane treatment are represented in Figure 4.50a-b, while the water contact angles on corresponding surfaces are shown as inset in Figure 4.50a-b. Considerable change in the surface morphology of GNFs before or after silane treatment was not observed under SEM. But, at some areas degradation in nanofilament structures was detected. The reduction in the density of GNFs also describes high sliding angle values (10° ± 2°) observed on silane treated GNFs. Degradation of GNFs can be attributed to oxygen plasma step which was performed prior to silane treatment. The SEM images of GNFs before and after oxygen plasma step are shown in Figure 4.51. The decrease of the density of GNFs after oxygen plasma step is clearly visible in Figure 4.51. The treatment of GNFs with oxygen plasma prior to silane functionalization is an important step as it creates abundant hydroxyl (-OH) groups at the surface of GNFs which act as anchor groups for silane molecules attachment. To check whether oxygen plasma step is necessary or not, GNFs were treated with silane molecules without plasma oxidation. The measurements after silane treatment showed the contact angle values of 145.1° ± 2° (Figure 4.52a), confirming oxygen plasma step is necessary to fabricate a superhydrophobic surface. To demonstrate the influence of surface roughness on hydrophobicity, functionalization of cleaned and plasma activated bare glass substrate with silane was also performed. The resulting contact value is presented in Figure 4.52b which shows the water contact angle values of 117° ± 7°. The surface of GNFs was also treated with 1H, 1H, 2H, 2H-perfluorodecyltriethoxysilane which resulted in a rather high contact angle values 162.4° ± 6.5° (Figure 4.52c shows water contact angle).

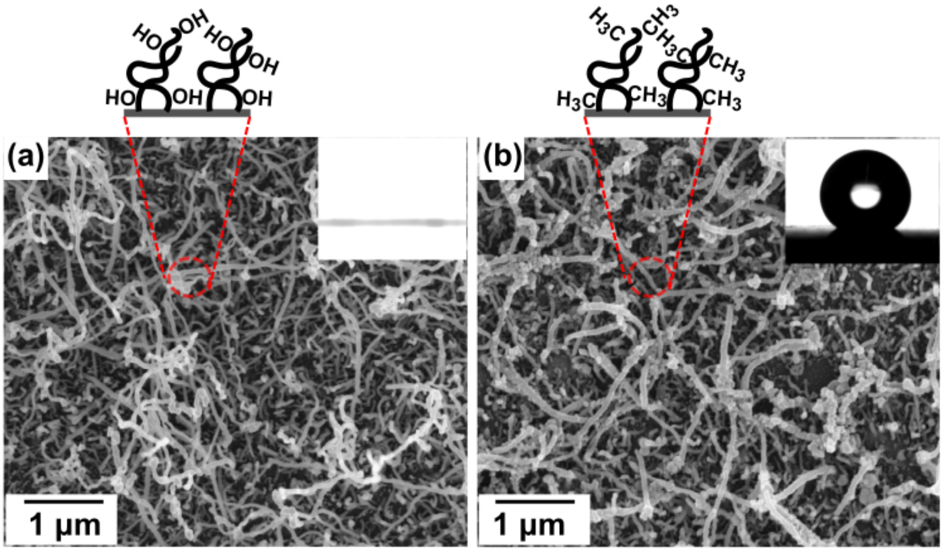

Figure 4.50. SEM images of GNFs (a) before and (b) after silane treatment. Insets show the water contact angles. Reprinted with permission from [80]

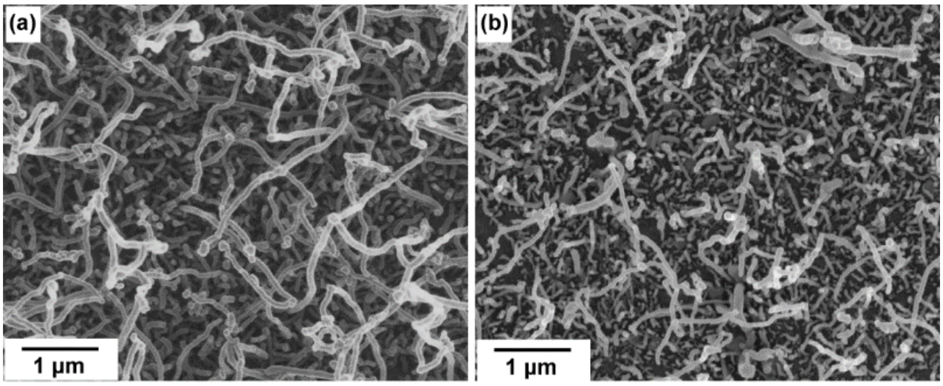

Figure 4.51. SEM images of GNFs (a) before and (b) after oxygen plasma treatment. Reprinted with permission from [80]

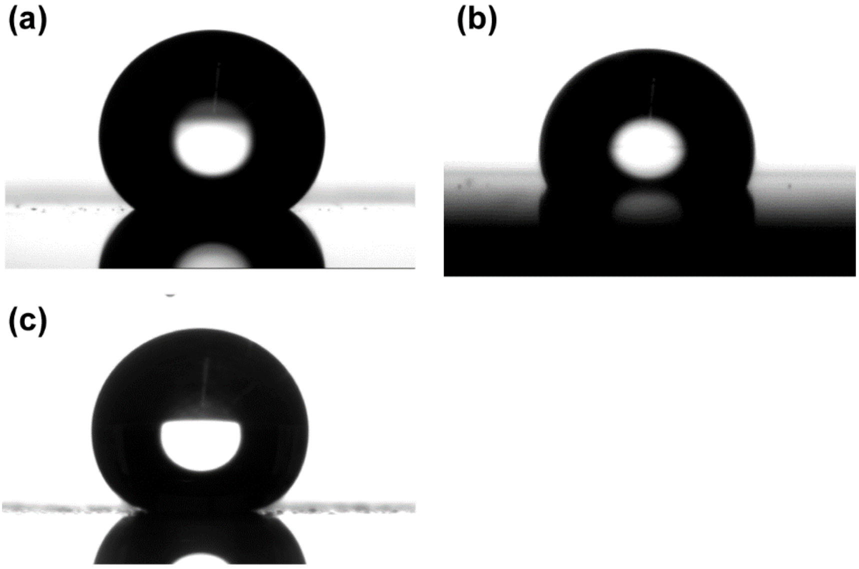

Figure 4.52. Water contact angles on (a) silane functionalized GNFs without oxygen plasma treatment, (b) silane functionalized bare glass substrate, (c) 1H, 1H, 2H, 2H-perfluorodecyltriethoxysilane functionalized GNFs. Reprinted with permission from [80]

Utilizing the high surface roughness of germanium oxide nanofilaments and one step treatment with silane molecules to make a water repellent surface is an elegant approach, given the fact germanium oxide is water soluble. A SEM image of germanium oxide nanofilaments substrate after few minutes of immersion in water is shown in Figure 4.53 where nanofilaments are completely desorbed from the surface.

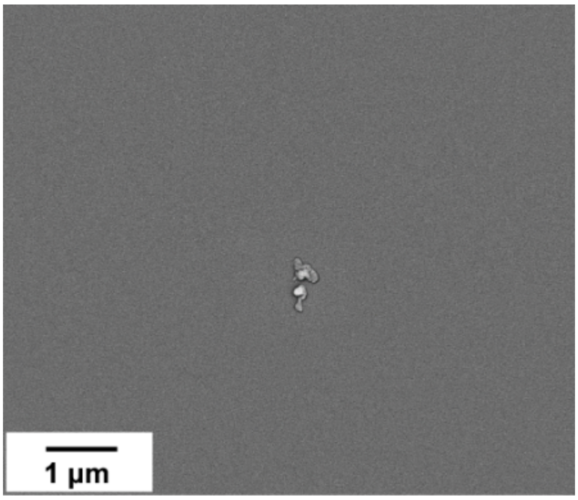

Figure 4.53. SEM image of GNFs after dipping in water

Even the rolling of water droplets on silane treated GNFs was observed at high sliding angles, macro-sized water droplets remained completely spherical when placed on silane treated GNFs substrate (Figure 4.54a). Water droplet was dyed with Trypan blue stain. Rolling of macro-sized droplets was observed at low sliding angles as well. Rolling of macro-sized droplets was observed on silane treated GNFs surface when exposed to water stream. The behavior of water rolling was recorded using a high speed camera and photographs were taken from the video. The photographs taken from high speed camera video are represented in Figure 4.54b where rolling of water droplets on the surface inclined at 10° is shown. One photograph represents time span of 5 milli-seconds while the arrow indicates the roll off direction of water droplets.

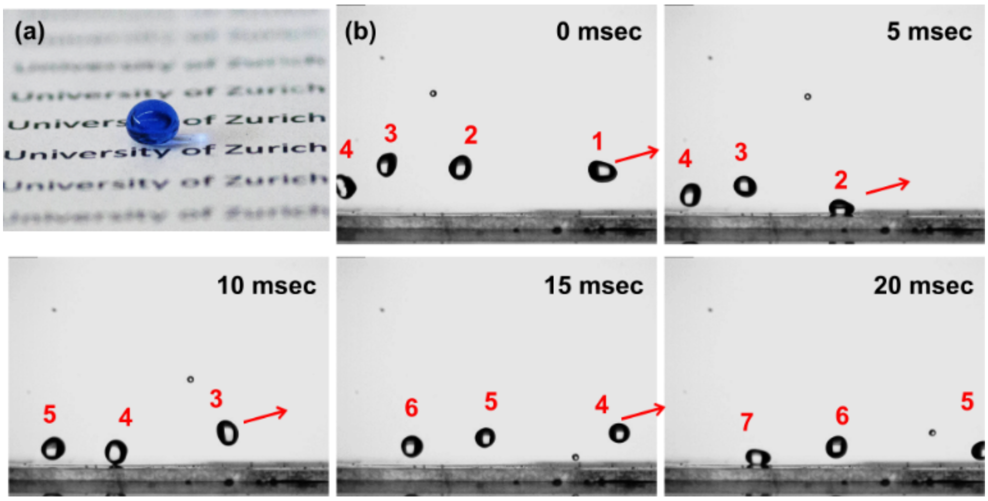

Figure 4.54. (a) Formation of spherical water droplets on superhydrophobic GNFs (water colored with Trypan blue stain), (b) rolling of water droplets on superhydrophobic GNFs. Reprinted with permission from [80]

Self-cleaning properties of silane treated GNFs is represented in Figure 4.55a. The water droplet completely removes the sea-sand particles from the surface showing self-cleaning property of silane treated GNFs. To observe the performance of superhydrophobic GNFs against chemicals with various pH values, water contact angles of different pH solutions were measured. Aqueous solutions with pH varying from 2-14 were prepared using NaOH and HCl. The short-term chemical resistance of silane functionalized GNFs to various chemicals is presented in Figure 4.55b. The surfaces exhibited good chemical resistance to all pH solutions (pH 2-12) and remained superhydrophobic (contact angle > 150°). However, the contact values decreased for highly basic solutions (contact angle: 148° ± 10°). Similar observations were for silane treated bare glass substrates.

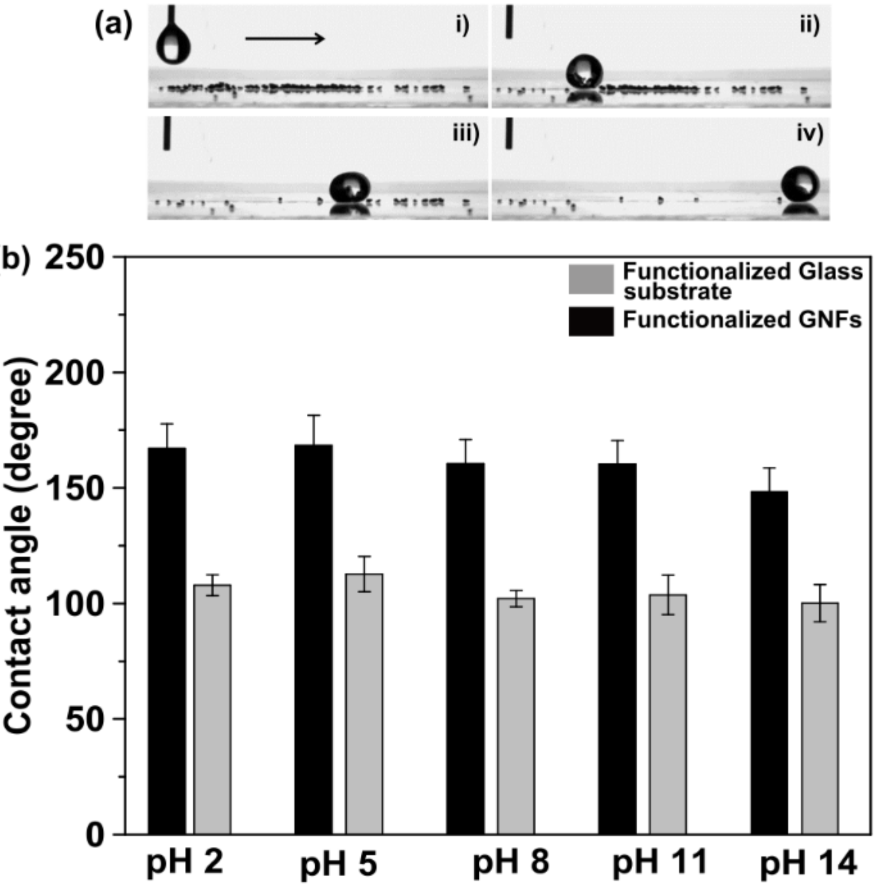

Figure 4.55. (a) Self-cleaning property of superhydrophobic GNFs, (b) water contact angles of various pH aqueous solutions on silane treated bare glass and GNFs substrate. Reprinted with permission from [80]

Even the silane treated GNFs exhibit good chemical resistance to pH solutions, but these studies are not sufficient because the surfaces are exposed to these solutions for a short period of time (~ 30 seconds). Furthermore, very small volumetric amounts of pH solutions came in contact with the surfaces which do not replicate the real-life conditions where rather large amounts of pH solutions come in contact with surfaces for a prolonged period. Therefore, the chemical stability of surfaces should be tested by dipping the substrates in acidic (pH 2) and basic pH (pH 14) solutions for a longer duration. The contact angles observed on substrates after immersion in acidic or basic solutions are shown in Figure 4.56. The contact angles on the substrates dipped in basic solutions decreased abruptly. The contact angle values of $128.6^{o} \pm 14^{o}$ were observed after 1 hour of immersion in basic solutions which decreased to $117.3^{o} \pm 10.3^{o}$ (after 2 hours) and $33.4^{o} \pm 7.3^{o}$ (after 3 hours). After 24 hours of immersion in basic solution contact angle values of $13.3^{o} \pm 4.7^{o}$ were observed. The silane treated GNFs showed good chemical resistance to acidic solutions and remained superhydrophobic (contact angle $>150^{o}$) after 3 days of immersion. The values of contact angles decreased for the substrates immersed for 5 days in acidic solutions and the surfaces changed from superhydrophobic to hydrophobic. A further decrease in contact angle was observed for the substrates immersed for 7 days in acidic solutions. Water droplets did not slide for any of the substrates.

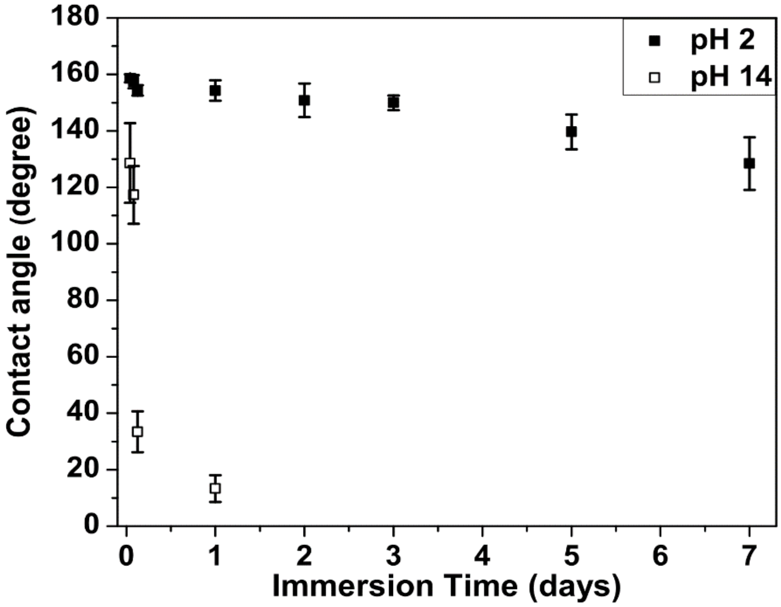

Figure 4.56. Contact angle values observed on silane treated GNFs as function of immersion time in acidic or basic solutions. Reprinted with permission from [80]

The analysis of the immersed substrates under SEM showed that silane treated GNFs were etched completely just after 1 day of immersion in basic solutions (Figure 4.57a-b). The complete etching of nanofilaments from the surface explain the abrupt decrease in the contact angles. The reason behind poor performance of silane treated GNFs in basic solutions is because of instability of polysiloxanes to basic conditions [4]. However, in acidic solutions nanofilaments retained their structure even after 7 days of immersion. Degradation and etching of filaments at some regions was observed after 7 days of immersion in acidic solutions (Figure 4.57c-d).

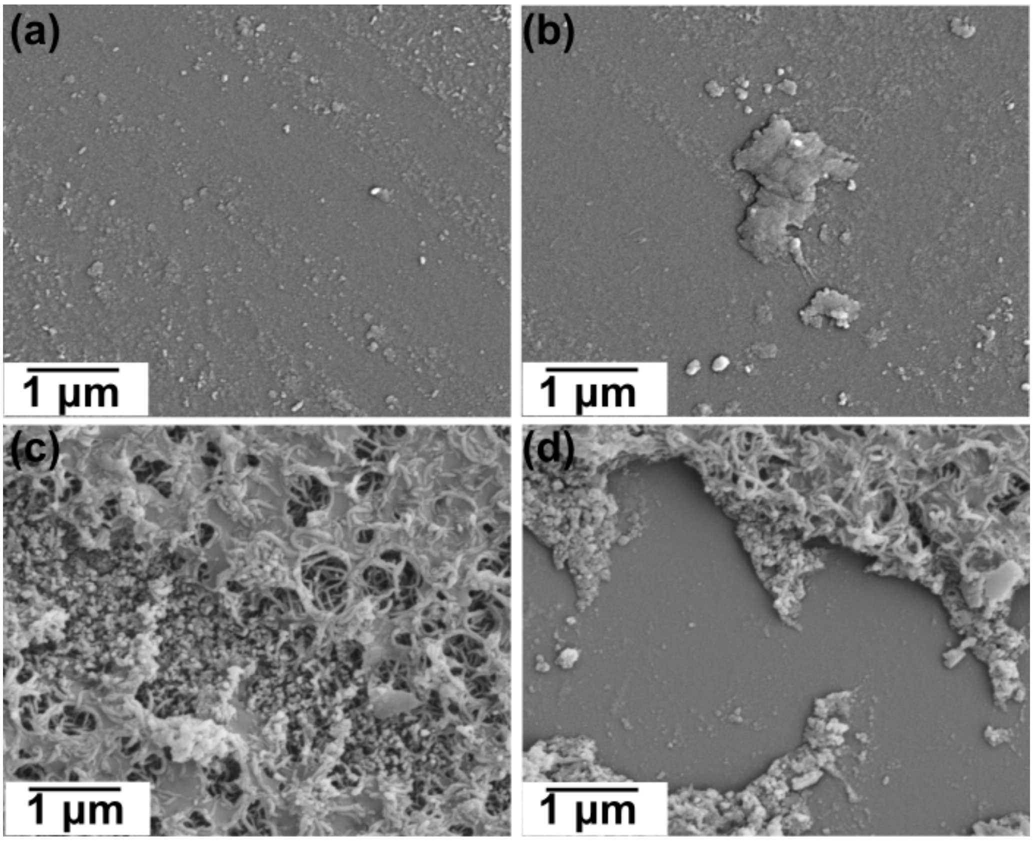

Figure 4.57. SEM images of silane treated GNFs after (a-b) 1 day of immersion in basic solution, (c-d) after 7 days of immersion in acidic solution. Reprinted with permission from [80]

With this method we have presented an elegant and unique approach towards synthesis of germanium oxide nanostructures using ambient processing condition i.e. room temperature and ambient pressure by applying DAGS chemistry. We have shown that DAGS method of synthesis not only limited to silicone systems but it can be extended to germanium system to synthesize nanostructures. The GNFs synthesized using DAGS chemistry were 80-100 nm in diameter and 1-10 µm in length. The relative humidity which plays an important role in the DAGS method has been adjusted at various values to study its influence on GNFs synthesis. We have shown that GNFs can be synthesized in a wide window of humidity i.e. 30-40% which gives the flexibility in terms of synthesis conditions.

4.4 Chemical vapor deposition of Aumina and mixed Alumina-Silicone based nanostructures

The synthesis of nanomaterials using DAGS chemistry by chemical vapor deposition technique has been successfully applied to silicone and germanium-based systems. Subsequently, we have extended the application of the DAGS method to alumina (Al) and mixed alumina-silicone (Al-Si) systems as well. Usually 1D nanomaterials of Al or Al-Si are synthesized using hydrothermal methods [174] [175] or chemical vapor deposition [176]. However, most of these methods either require liquid phase synthesis or application of high processing temperature which is not environment friendly or energy efficient. The synthesis of 1D nanostructure of Al and Al-Si by the DAGS method using room temperature processing is therefore, facile and economical.

4.5 Synthesis of alumina nanostructures

For the synthesis of alumina nanostructures using the DAGS method, the same synthesis technique was used which was applied for the synthesis of silicone nanofilaments and germanium oxide nanofilaments. Si wafers were used as substrate which were dipped in acetone for the duration of 30 minutes to remove organic impurities. Washing of the wafers was performed in Milli-Q® water. To generate hydroxyl groups at the surface of the wafers, activation of the wafer surface was performed in oxygen plasma chamber followed by washing with Milli-Q® water. After drying the wafers in the stream of nitrogen gas, they were introduced in the coating chamber which was maintained at the relative humidity of 35% ± 1%. After 1 hour of flushing the coating chamber with humidified nitrogen, trimethylaluminum (TMA) precursor was introduced into the chamber. Due to high reactive nature of TMA, it was handled in the glove box maintained at the O_2 and H_2O level below 1 ppm. TMA was transferred from the glove box in an air tight glass vial and introduced into the coating chamber with a syringe. After 4 hours of reaction duration, the wafers were taken out and observed under SEM. SEM investigation revealed the growth of 1D nanostructures at the substrate. SEM image of the nanostructures is shown in Figure 4.58a-c, the high magnification image illustrates that the 1D nanostructures were composed of particles assembled in the shape of a necklace. EDX analysis of these 1D nanostructures revealed the presence of Al, O, Si and C elements where the signals from Si and C arise from the Si wafer and carbon tape respectively. The further characterization of the 1D nanostructures was performed using selected area electron diffraction (SAED) which indicated that particles were amorphous in nature. To check the distribution of elements inside the 1D nanostructures EDX mapping was also performed. TEM image and corresponding EDX mapping of the 1D nanostructures is presented in Figure 4.59 which revealed the presence of O and Al inside the 1D nanostructures. It is probable that nanostructures were free of C as we did not observe any carbon contrast in EDX mapping. The full EDX spectra of the map is presented in the Figure 4.60, the signals from Cu and C are from the TEM grid and carbon tape below the TEM grid.

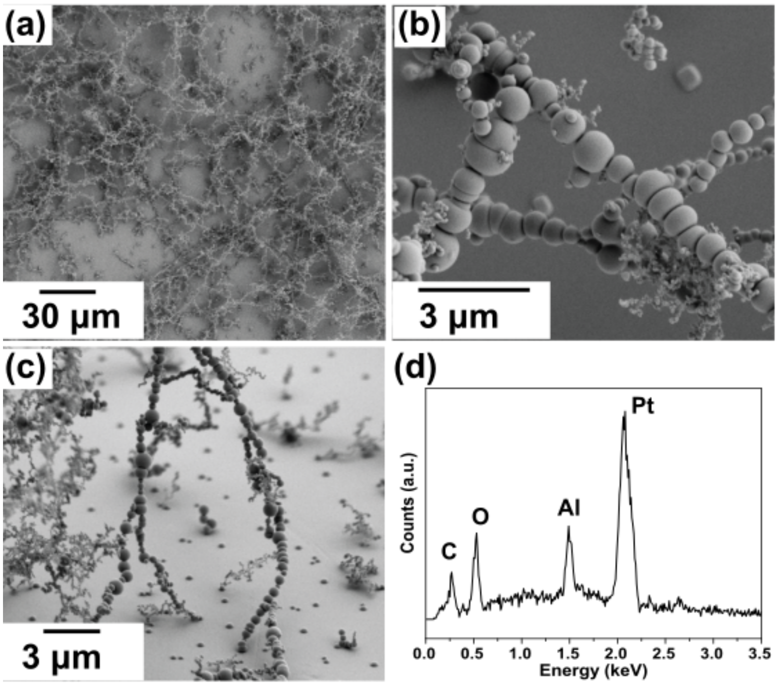

Figure 4.58. SEM image of alumina nanostructures (a-c), (d) EDX spectra of alumina nanostructures. Reprinted with permission from [177]

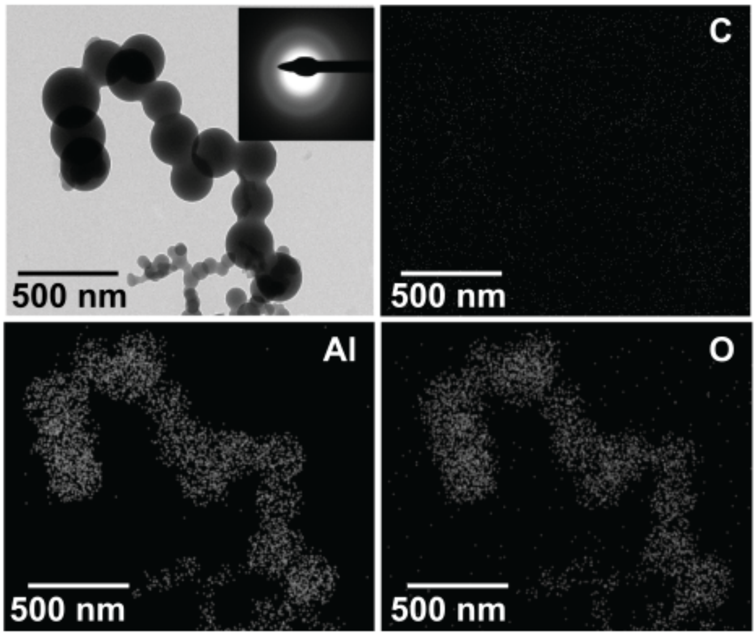

Figure 4.59. TEM image of alumina nanostructures (inset shows SAED image) and EDX mapping of corresponding nanostructures. Reprinted with permission from [177]

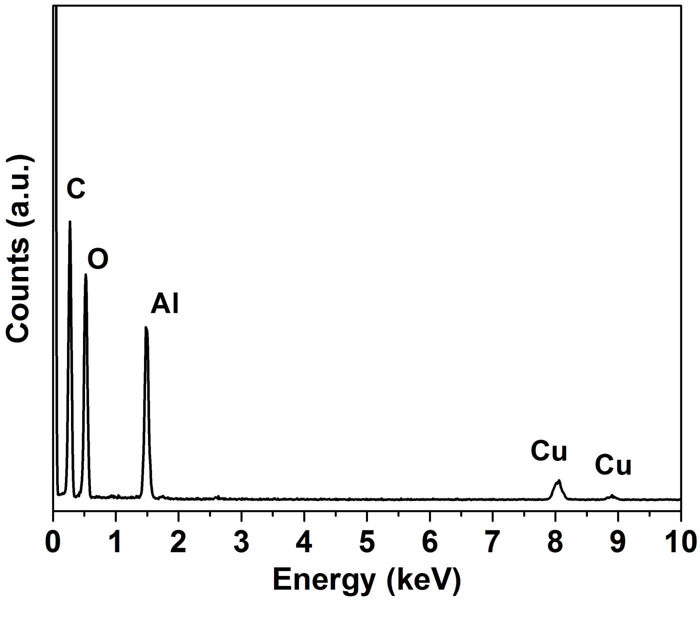

Figure 4.60. EDX spectra of the elemental mapping of alumina nanostructures. Reprinted with permission from [177]

4.5.1 The influence of relative humidity and reaction time

The 1D nanostructures of alumina described earlier were synthesized at relative humidity of 35% ± 1%. The level of humidity at which synthesis is performed carries significant importance in DAGS method. To check the effect of humidity on the synthesis, reactions were carried out at the relative humidity of 2% ± 1%, 17% ± 1%, 50% ± 1% and 70% ± 1%. The analysis of the substrates after the reaction was performed by SEM. When the level of humidity was very low i.e. 2% few particles were observed at the surface of the substrate (Figure 4.61a). The density of nanostructures increased with an increase in the level of relative humidity. However, at very high humidity values such as 50% and 70% aggregated structures were also observed along with 1D nanostructures (Figure 4.61c-f). As discussed earlier, the humidity plays an important role in DAGS method. When the substrates are placed in humid environment nano water droplets in the form of islands are formed at the surface. The formation of water islands occurs due to inhomogeneous physical or chemical nature of the surface. The precursors when inserted into the coating chamber vaporize due to its high vapor pressure and react with the water droplets which act as confined reaction vessels. At very low humidity levels, the possibility for the formation of water droplets at the surface decreases which leads to decrease in the growth of nanostructures. While at high levels of humidity high abundance of water is present at the surface of substrate in the form of islands or thick layers which leads to the formation of aggregated structures.

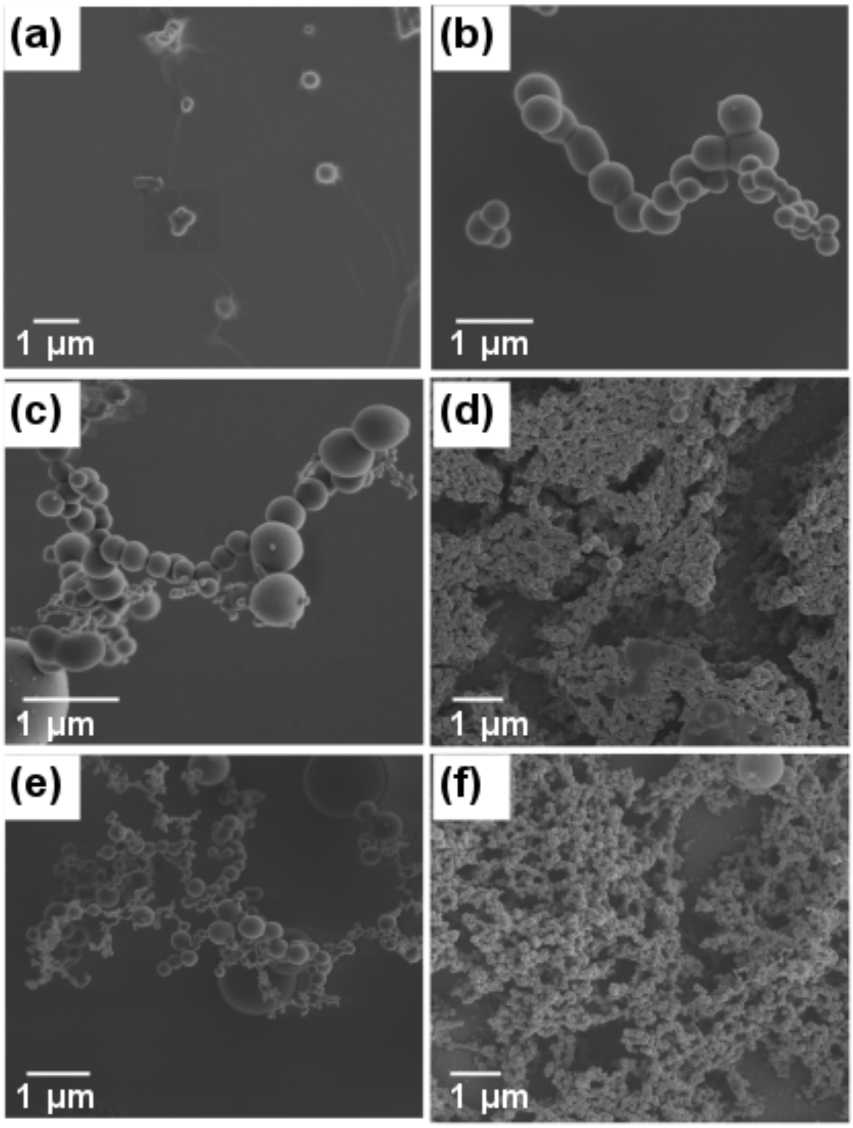

Figure 4.61. SEM images of 1D alumina nanostructures synthesized at (a) 2%, (b) 17%, (c-d) 50%, and (e-f) 70% relative humidity. Reprinted with permission from [177]

Time dependent growth of alumina nanostructures was performed by stopping the reaction after 15 and 30 minutes of TMA introduction into the coating chamber. After 15 minutes of reaction small particulate structures were observed at the surface. After 30 minutes of reaction duration particulate structures grew into 1D nanostructures (Figure 4.62a-d).

We also performed the synthesis using another precursor, for that purpose triethylaluminum (TEA) was used. Synthesis was carried out at 35% ± 1% relative humidity for the duration of 4 hours. The analysis of substrate under SEM showed the presence of small particles at the surface with very low density (Figure 4.63). The reason behind no growth of nanostructures using TEA can be ascribed to low vapor pressure of TEA (1mm Hg at 62.2ºC).

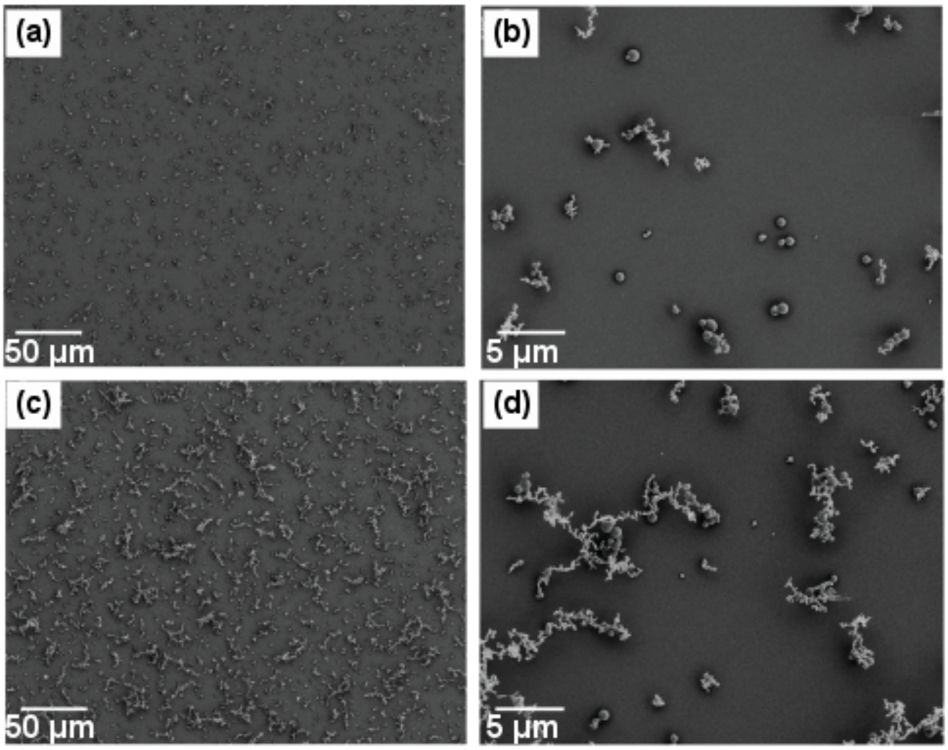

Figure 4.62. SEM images of alumina nanostructures after (a-b) 15, and (c-d) 30 minutes of reaction duration. Reprinted with permission from [177]

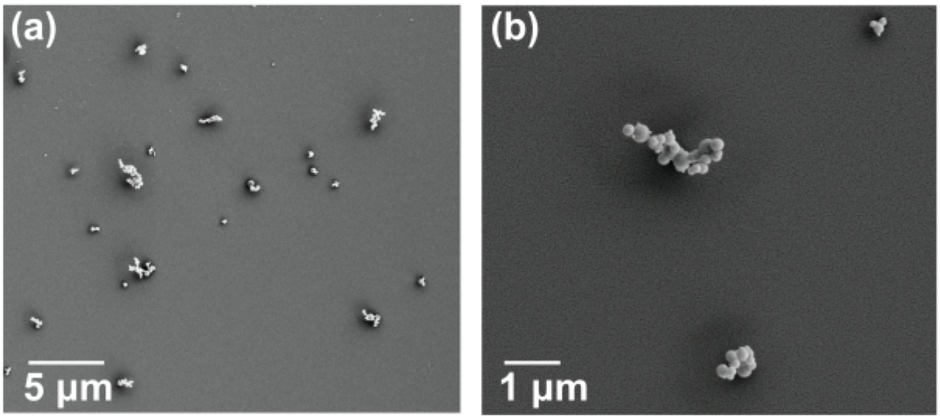

Figure 4.63. SEM image of alumina nanostructures synthesized using TEA. Reprinted with permission from [177]

4.5.2 Thermal stability studies

The stability of 1D alumina nanostructures against high temperature was tested by annealing the coated Si wafers in air inside the muffle furnace. The substrates were annealed at 300°C, 400°C, 500°C and 600°C respectively with the heating rate of 10°C/minute. The dwell time of 4 hours was used for all samples followed by overnight cooling inside the furnace. The substrates were observed under SEM after annealing. The SEM images of the annealed substrates are shown in Figure 4.64.

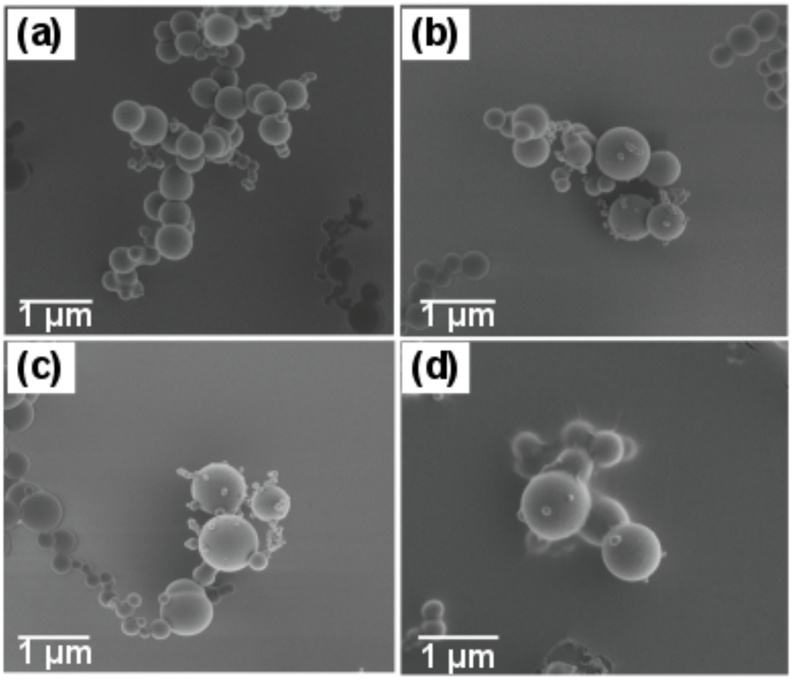

Figure 4.64. SEM images of 1D alumina nanostructures after annealing at (a) 300°C, (b) 400°C, (c) 500°C, (d) 600°C. Reprinted with permission from [177]

SEM investigation show with the increase in the annealing temperature aggregation and sintering of nanostructures was observed (Figure 4.64). The nanostructures remained amorphous after annealing when tested using SAED. TEM images and respective SAED images of the annealed nanostructures is represented in Figure 4.65. The elemental composition of the nanostructures as a function of annealing temperature was also determined using EDX mapping which did not show any change in the distribution of elements in the nanostructures.

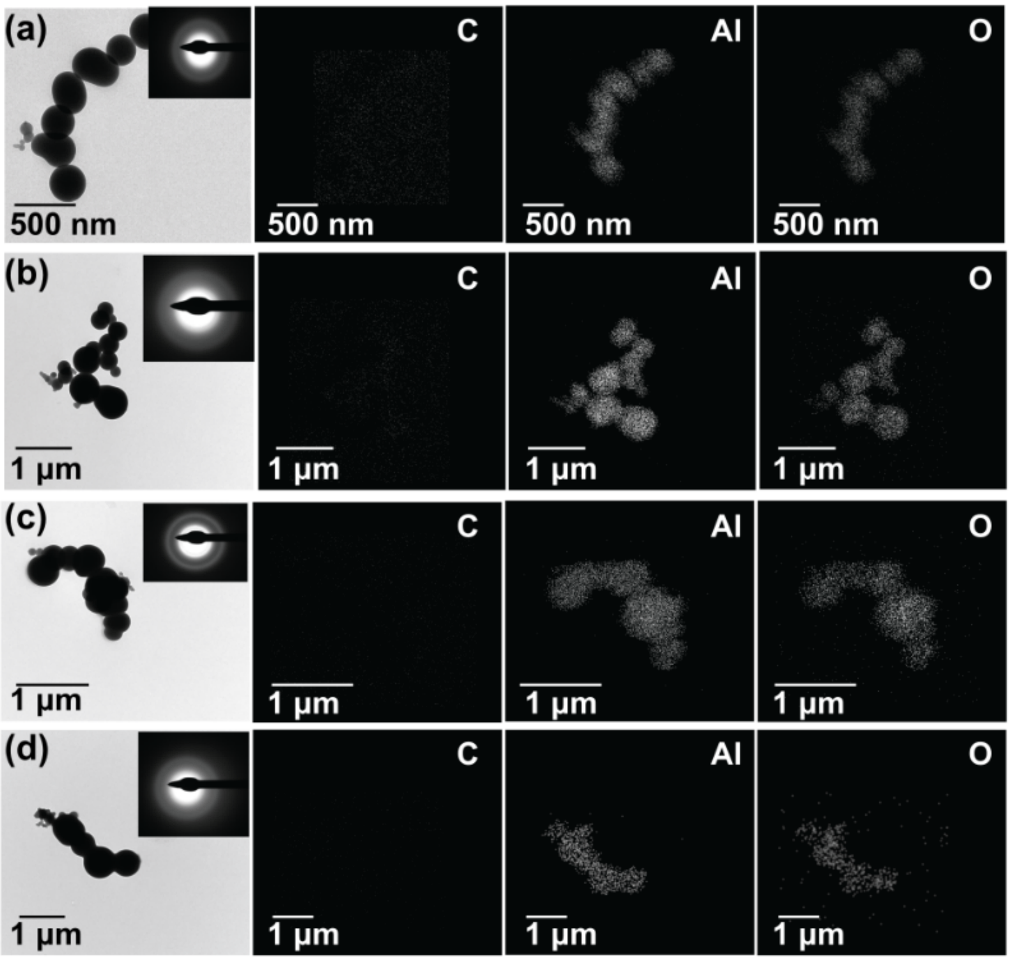

Figure 4.65. TEM images and EDX mapping of 1D alumina nanostructures after annealing at (a) 300ºC, (b) 400ºC, (c) 500ºC, (d) 600ºC. Insets show the SAED image of corresponding nanostructures. Reprinted with permission from [177]

4.6 Synthesis of mixed alumina-silicone nanostructures

As described in earlier, when trimethylaluminum (TMA) is used for DAGS reaction it leads to the synthesis of alumina nanostructures. On the other hand, only trichloromethylsilane (TCMS) employed in the DAGS method yields in the formation of silicone nanofilaments (SNFs). To observe the effect of combining these two precursors on the growth of nanostructures, synthesis was carried out by mixing 0.4 mmoles of TMA and 0.8 mmoles of TCMS. The precursors were mixed inside the glove box which was maintained at H_2O and O_2 levels below 1 ppm. The air tight glass vial was used to transport the precursors, and inserted into the coating chamber using a syringe. Cleaned and activated Si wafers were placed inside the coating chamber which was maintained at the relative humidity of 35% ± 1% by the constant flow of dry and humidified nitrogen. The precursors were injected into the coating chamber after 1 hour of equilibration. After 4 hours of reaction duration, the coating chamber was opened and the analysis of the wafers was made. SEM and TEM observation showed the presence of 1D nanostructures composed of nanoparticles arranged in the form of a necklace or beads (Figure 4.66a-b). These nanostructures were very similar to the nanostructures synthesized using only TMA precursor. SAED showed the nanostructures were amorphous in nature. EDX analysis of the nanostructures showed the peaks of C, Al, O, Si and Cl elements, indicating the mixed alumina-silicone structure. The elemental mapping of the alumina-silicone nanostructures is shown in Figure 4.67, which shows homogenous distribution of elements inside the nanostructures. The carbon signal is originated from the methyl groups of TCMS. Due to the presence of carbon film underneath, the contrast in carbon map is very low.

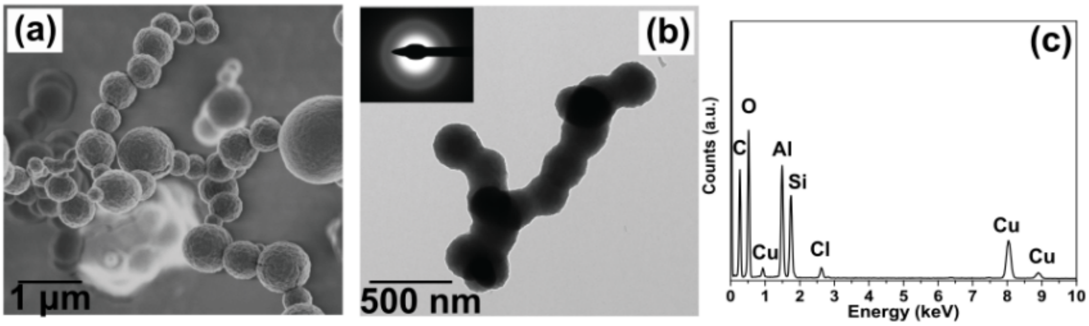

Figure 4.66. SEM (a), TEM (b) image of nanostructures (inset SAED image), (c) EDX spectra of nanostructures. Reprinted with permission from [177]

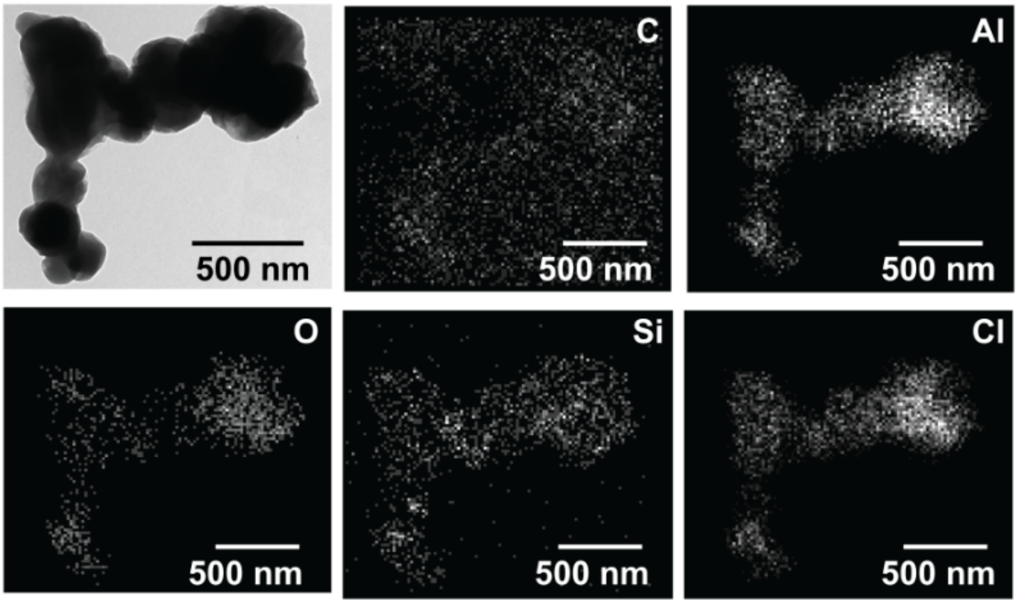

Figure 4.67. Elemental mapping of mixed alumina-silicone nanostructures. Reprinted with permission from [177]

The origin of Cl can be ascribed to grease which is used to seal the coating chamber or TCMS. EDX analysis of the grease was performed using EDAX system coupled with SEM and is represented in Figure 4.68. But EDX analysis showed grease was only composed of C, O and traces of Si.

The presence of Cl was not found in the nanostructures synthesized only from TMA. When only TCMS precursor is used for the synthesis, SNFs are obtained and they do not show presence of Cl (as observed in elemental mapping Figure 4.69 and EDX spectra shown in Figure 4.70). When TCMS is used for the synthesis complete hydrolysis of silane occurs forming HCl. However, when the mixture of TCMS and TMA is used for the synthesis supposedly complete hydrolysis of TCMS does not occur and that is why Cl is still detected in the nanostructures.

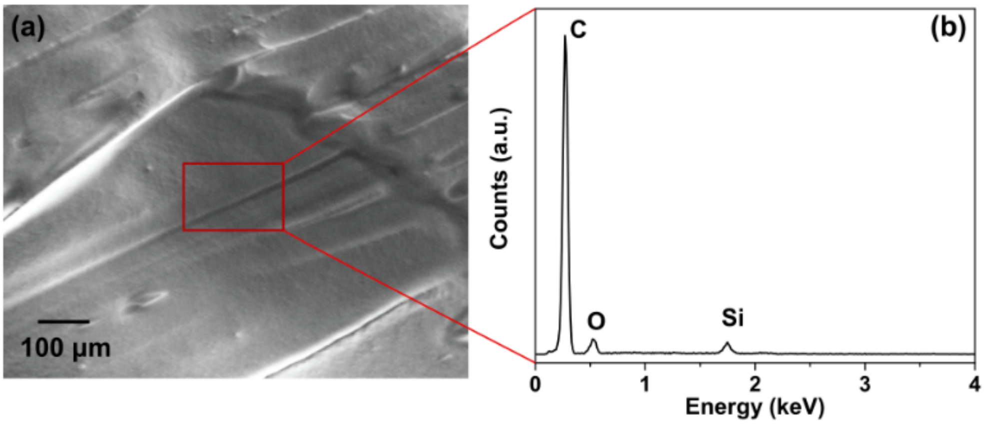

Figure 4.68. SEM image of grease and corresponding EDX spectra. Reprinted with permission from [177]

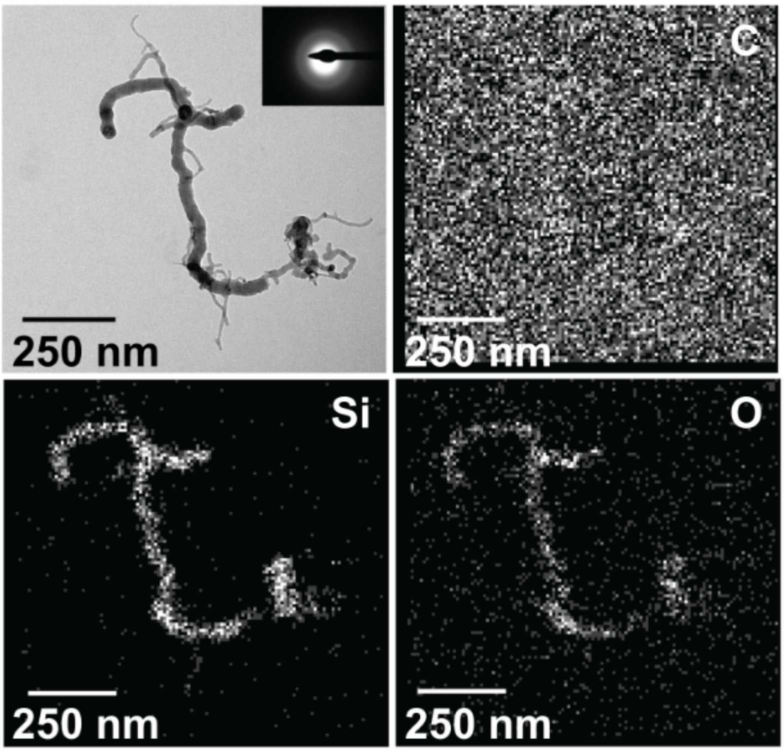

Figure 4.69. TEM image and elemental mapping of SNFs (inset show the SAED image). Reprinted with permission from [177]

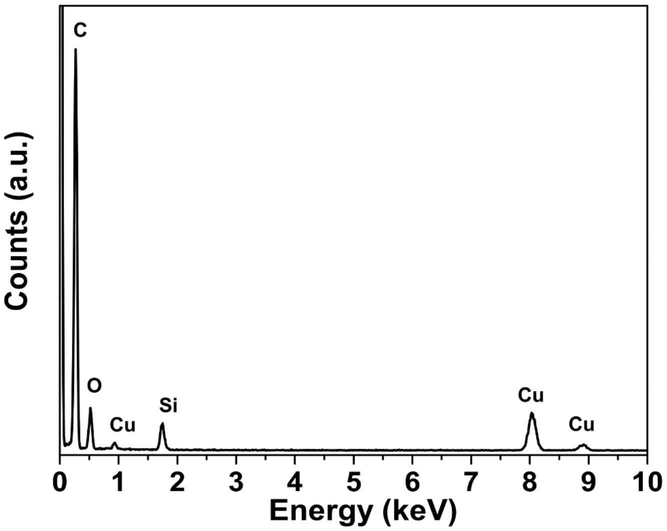

Figure 4.70. EDX spectra of SNFs. Reprinted with permission from [177]

The characterization of nanostructures synthesized using TMA and mixtures of TMA and TCMS precursors was also performed using infrared spectroscopy. To eliminate the possibility of signals originating from Si-O-Si bond, syntheses were carried out on germanium wafers. FTIR spectra of nanostructures is shown in Figure 4.71. In all spectra the signals from the substrate located at 840 cm^{-1} were detected which showed the presence of Ge-O-Ge [167]. In addition to the signals from the substrate indicating presence of Ge, the presence of other elements was also detected. The substrate coated with nanostructures synthesized using TMA only, showed the peaks located at 600 cm^{-1} and 965 cm^{-1} indicating Al-O-Al stretching [178]. The presence of hydroxyl groups (-OH) was also detected with the peaks located at 1600 cm^{-1} and 3300 cm^{-1}. The substrate coated using mixture of TMA and TCMS showed the presence of new peaks in addition to the Ge-O-Ge, Al-O-Al, -OH peaks. The comparison of this spectra was made with the substrate coated with only TCMS precursor. The comparison revealed the presence of Si-O-Si on both substrates. The signals originating from Si-O-Si vibration and stretching were observed at 787 cm^{-1} and 904 cm^{-1} for both substrates [179]. The presence of methyl groups was also observed in both nanostructures with the peaks located at 1270 cm^{-1} and 3000 cm^{-1} indicating the existence of Si-CH_3 and –CH_3 stretching [180] [181]. The substrate coated with only TCMS precursor showed Si-O-Si stretching at 1020 cm^{-1} and 1125 cm^{-1}. These Si-O-Si stretching were slightly shifted for the substrate coated with mixture of TMA and TCMS. This shift is highlighted in the Figure 4.71, which shows the shift of the peaks from 1020 cm^{-1} to 1036 cm^{-1} and 1125 to 1132 cm^{-1}. This shift of Si-O-Si peak shows the presence of Al in the surrounding and has been reported in literature for aluminosilicates [182]. However, the shifts in Si-O-Si due to the presence of Al do not provide a strong proof of the existence of Al-O-Si bond.

To get more information about the existence of bonding present in the nanostructures synthesized using mixture of TMA and TCMS, solid state NMR measurements were performed. ^{29}Si NMR spectra of the nanostructures is presented in Figure 4.72. The spectra show three peaks for mixed alumina-silicone nanostructures and silicone nanofilaments. For mixed alumina-silicone, the peaks were located at -48.95, -59.0 and -68.93 ppm, while for silicone nanofilaments the peaks at -48.28, -59.0 and -68.68 ppm were observed. These peaks show the typical silane peaks which are also called T region [183]. The peaks located at -48 ppm show one fold Si-O bonding in silicones, while peaks at -59 ppm and 68 ppm show two and three fold Si-O bonding in silicones [183] [184] [185] [186]. The spectra show T region peaks for both nanostructures with slight shifts indicating the similar surrounding of Si. Typically, the addition of Al into the network of Si leads to a chemical shift of 5-6 ppm as observed by Lippmaa [187] and others [188]. However, in the synthesized nanostructures such a strong shift in the peaks is not observed which provides a concrete evidence of the presence of mixed structures instead of Al-O-Si bonding in the nanostructures.

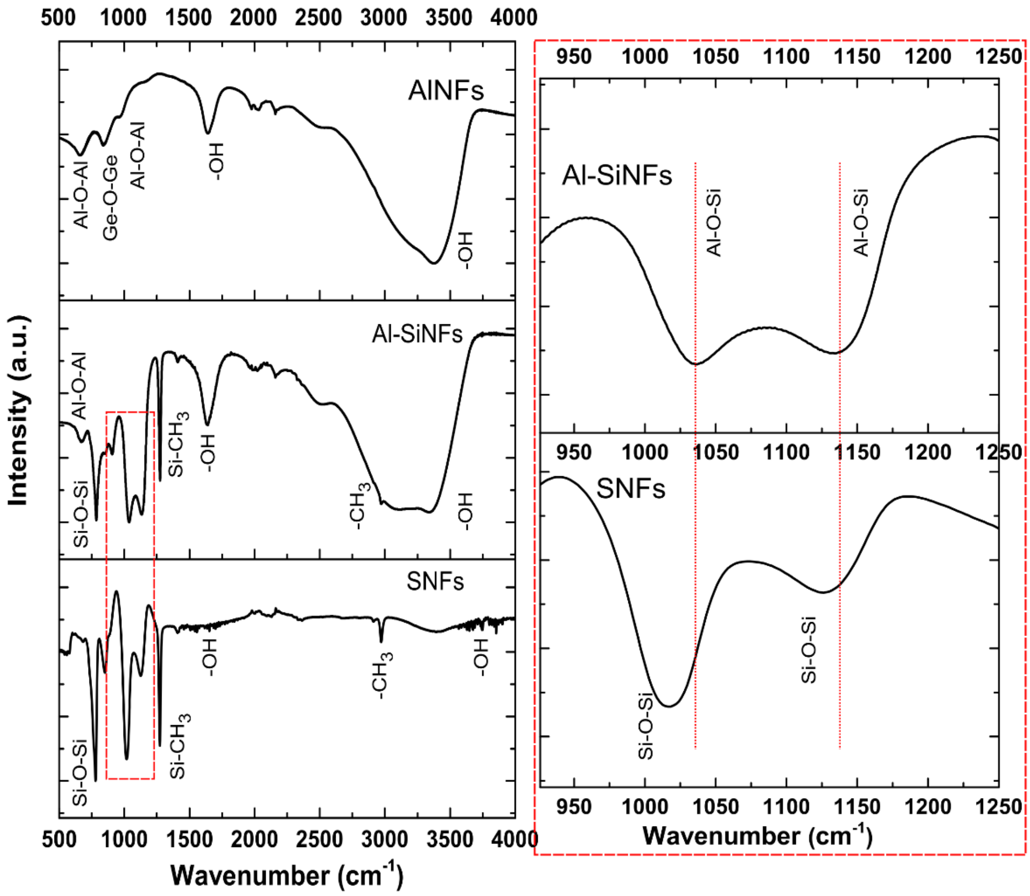

Figure 4.71. FTIR spectra of alumina nanostructures, mixed alumina-silicone nanostructures and silicone nanofilaments. Reprinted with permission from [177]

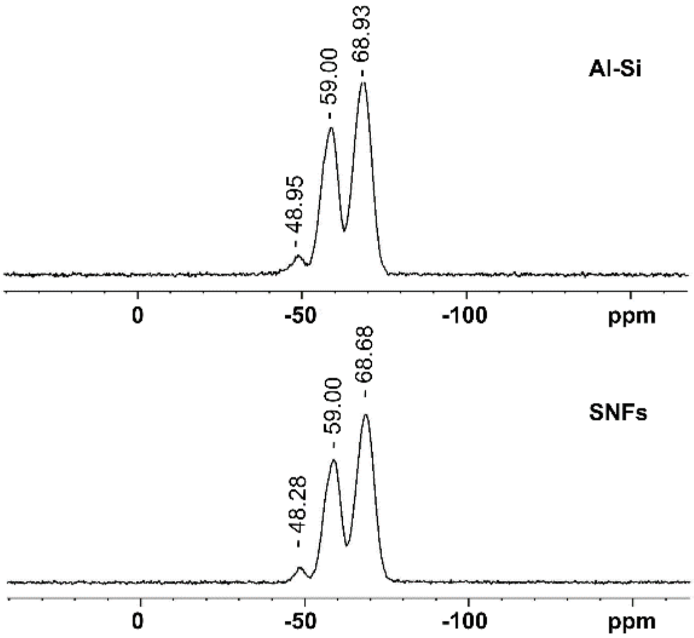

Figure 4.72. ^{29}Si NMR spectra of mixed alumina-silicone nanostructures and silicone nanofilaments. Reprinted with permission from [177]

4.6.1 Influence of relative humidity and reaction time

To observe the influence of relative humidity syntheses were performed at relative humidity of 2% ± 1%, 17% ± 1%, 50% ± 1%, and 70% ± 1%. At very low level of humidity i.e. 2%, growth of nanostructures was not observed. However, at high humidity levels the growth of nanostructures was observed and with the increase of relative humidity particulate and aggregated structures were observed instead of 1D nanostructures. The SEM images of nanostructures synthesized is shown in Figure 4.73a. At 17% relative humidity 1D nanostructures were observed while at high levels of humidity such as 50% and 70% short ordered and aggregated structures were observed (Figure 4.73b-c). The indefinite shapes of the nanostructures at high levels of humidity were because of reaction of silane precursor at high humidity leading to deformed or irregular shaped particles.

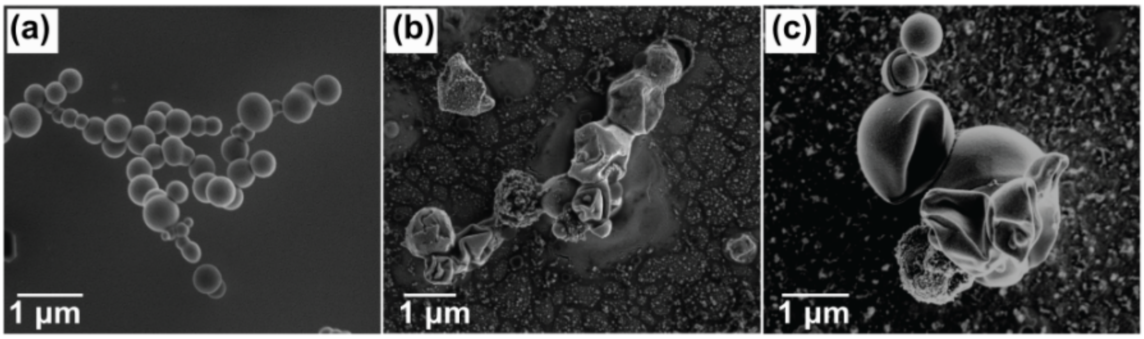

Figure 4.73. SEM images of mixed alumina-silicone nanostructures synthesized at (a) 17%, (b) 50%, and (c) 70% relative humidity. Reprinted with permission from [177]

The analysis of the nanostructures was also made using TEM and EDX mapping, which highlighted that at high humidity deformed or irregular shaped particles were observed (Figure 4.74). The elemental mapping showed the distribution of elements inside the nanostructures and a contrast in the carbon map was also observed which showed the presence of carbon in the nanostructures. The EDX mapping also showed that at relative humidity of 50% or 70%, the distribution of elements inside the nanostructures was not homogenous. The inhomogeneous distribution of elements in the nanostructures was due to uncontrolled reaction of TMA and TCMS at high levels of humidity.

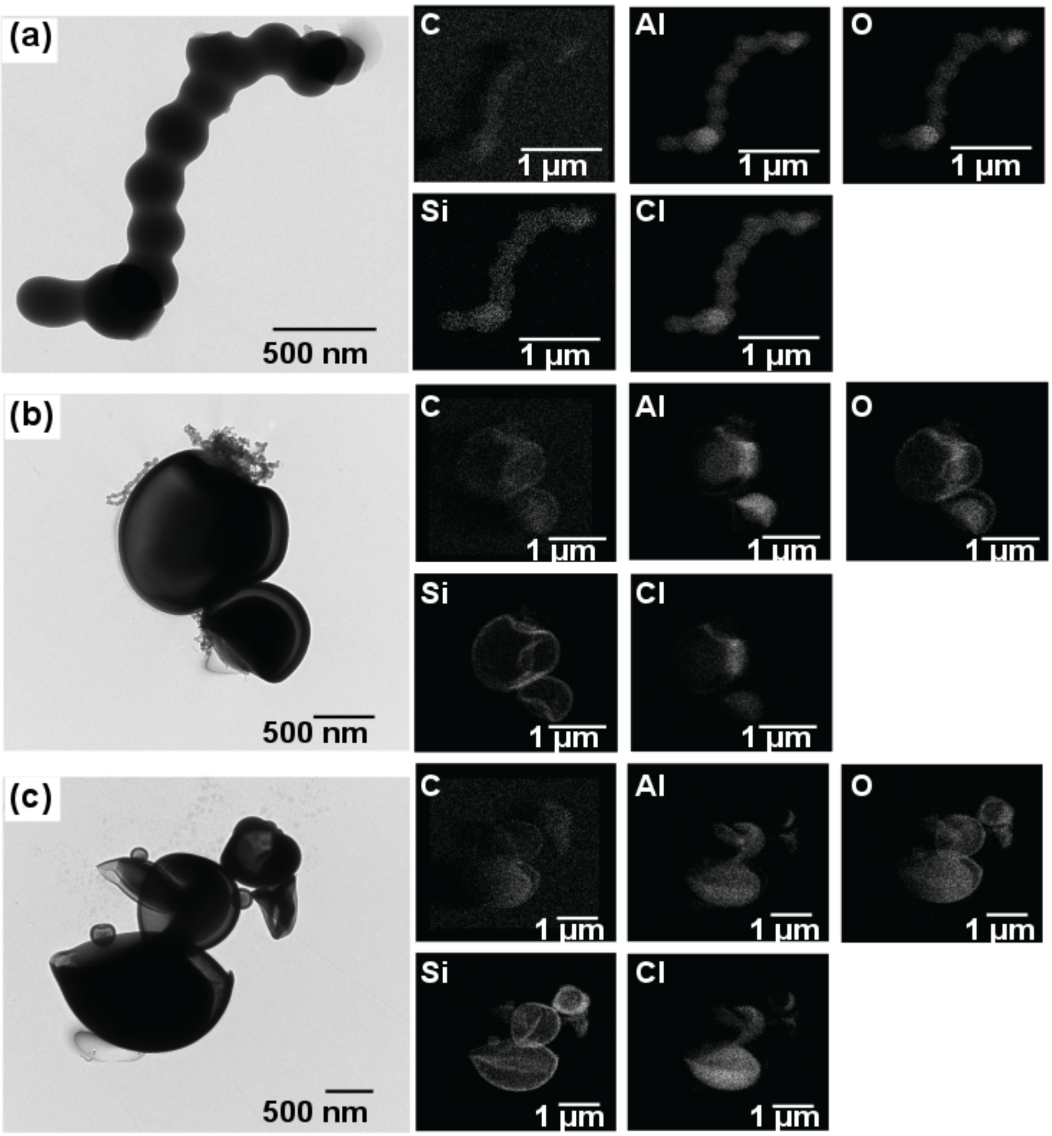

Figure 4.74. TEM images and elemental mapping of mixed alumina-silicone nanostructures synthesized at (a) 17%, (b) 50% and (c) 70% relative humidity. Reprinted with permission from [177]

The growth of nanostructures as function of reaction time was studied by carrying out the reaction for the short duration of 15 and 30 minutes. Initially small particle structures were observed with protrusions at the surface and after 30 minutes of reaction duration particle structures grew into the necklace type arrangement (Figure 4.75). The further analysis of the nanostructures was made using TEM and EDX. The protrusions were also observed at the surface of the particles after 15 minutes of reaction duration (Figure 4.76a). The elemental mapping indicated that the particles were composed of Al and the protrusions were made of Si. This suggests due to high reactivity of TMA particles of Al are formed at initial stages and the silane molecules react at the surface of particles and protrusions are formed. With the increase of reaction duration i.e. 30 minutes, the precursors react further which lead to necklace type structures.

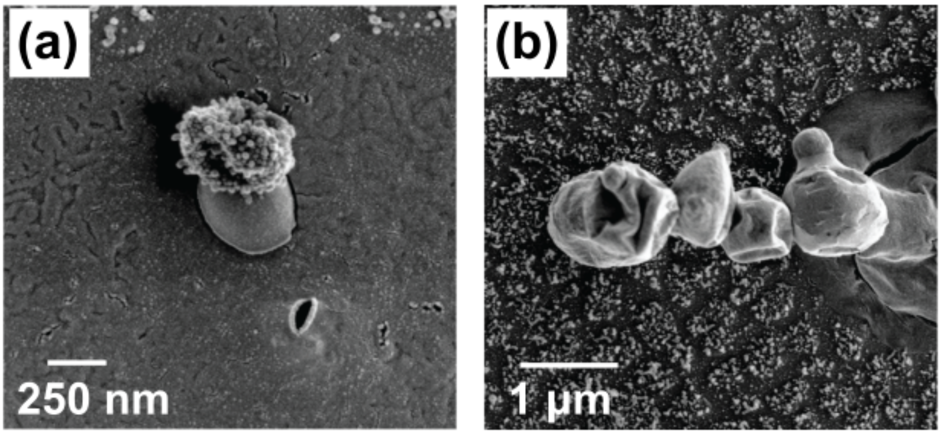

Figure 4.75. SEM images of mixed alumina-silicone nanostructures synthesized after (a) 15 minutes, (b) 30 minutes of reaction duration. Reprinted with permission from [177]

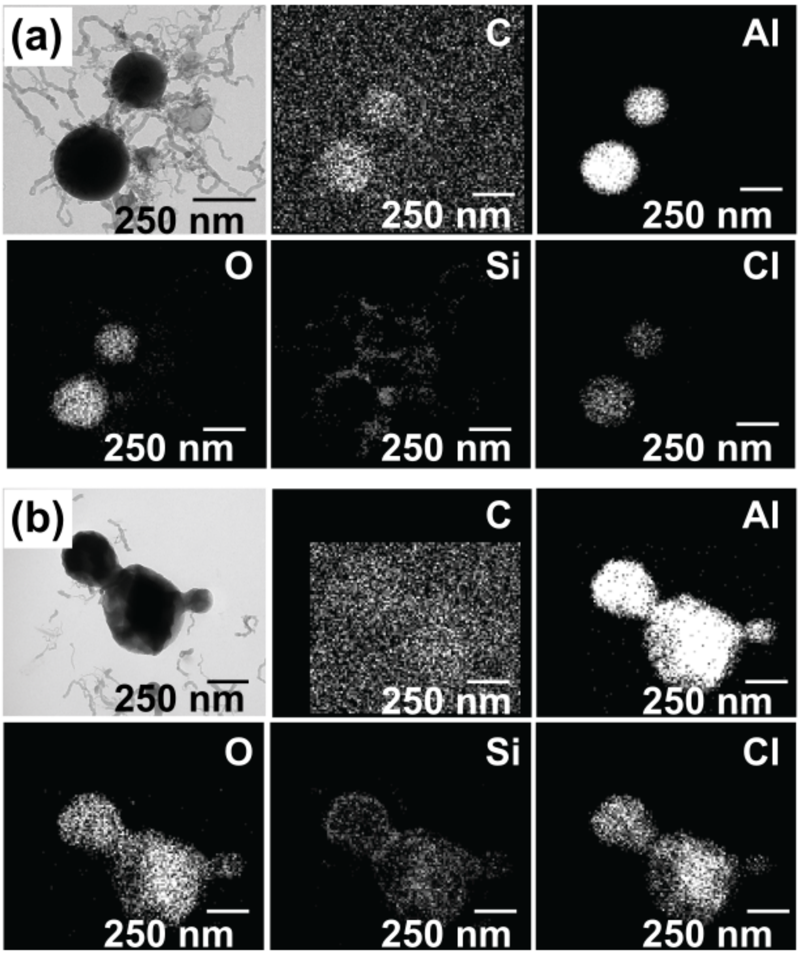

Figure 4.76. TEM images and elemental mapping of mixed alumina-silicone nanostructures synthesized after (a) 15 minutes, (b) 30 minutes of reaction duration. Reprinted with permission from [177]

In addition to the relative humidity and reaction time, the molar ratio of the precursors was also varied to check whether synthesis of mixed structures occurs or not. For this purpose syntheses were carried out for TMA/TCMS molar ratio of 0.25, 0.75 and 1. The characterization of the synthesized nanostructures was made using TEM and EDX mapping to confirm the formation of mixed structures. As observed in Figure 4.77, Figure 4.78, and Figure 4.79, the change of molar ratio also lead to the synthesis of mixed alumina-silicone nanostructures.

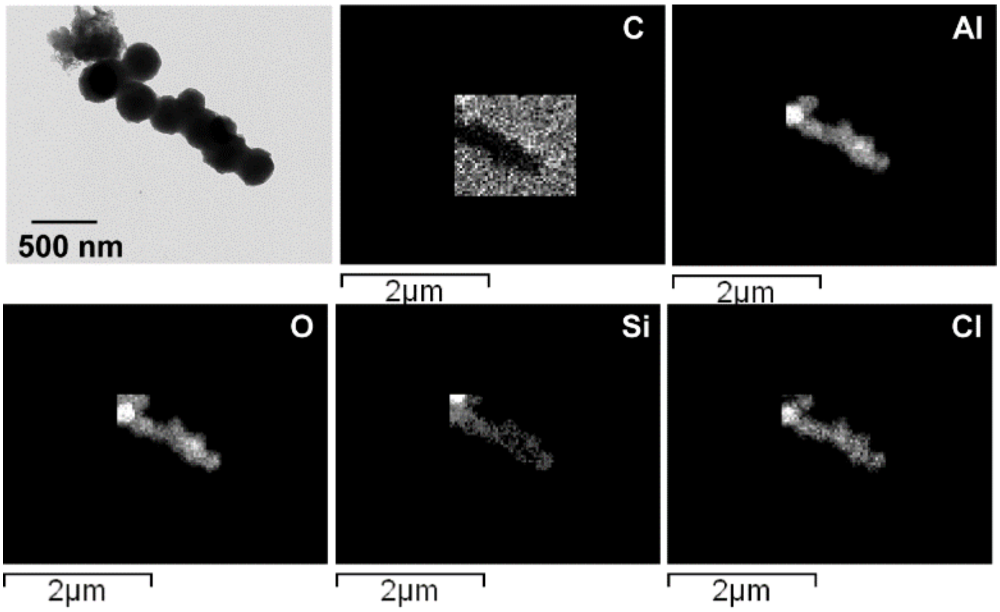

Figure 4.77. TEM image and elemental mapping of mixed alumina-silicone nanostructures synthesized at TMA/TCMS ratio 0.25

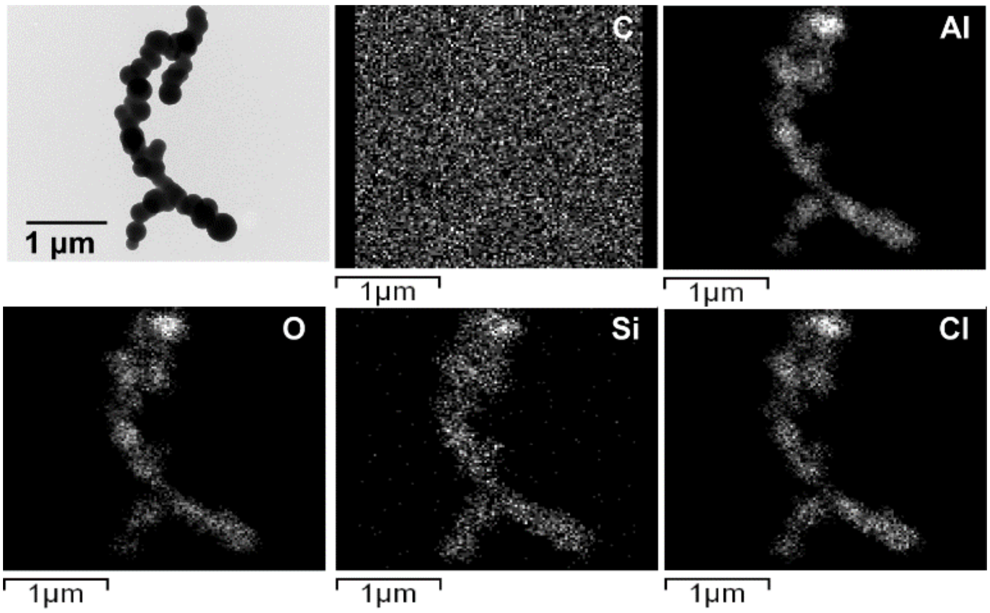

Figure 4.78. TEM image and elemental mapping of mixed alumina-silicone nanostructures synthesized at TMA/TCMS ratio 0.75

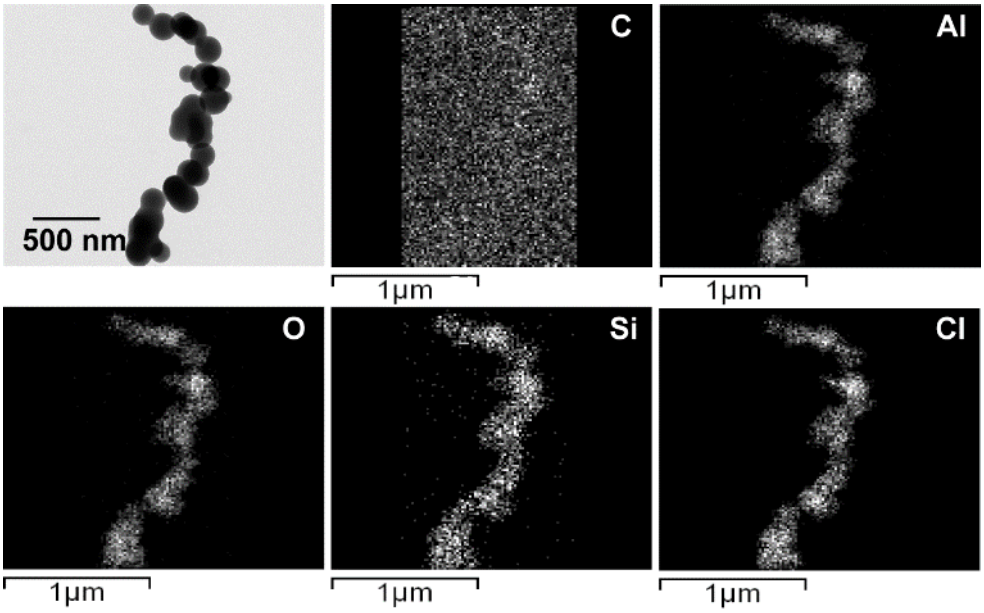

Figure 4.79. TEM image and elemental mapping of mixed alumina-silicone nanostructures synthesized at TMA/TCMS ratio 1

4.6.2 Thermal stability studies

The thermal stability of mixed alumina-silicone nanostructures was checked by performing annealing in air. The substrates were heated at the temperatures of 300ºC, 400ºC, 500ºC and 600ºC followed by overnight cooling inside the furnace. The heating rate of 10ºC/minute was used, while the dwell time of 4 hours was used for all samples. SEM investigation showed the degradation and aggregation of necklace structure with the increase in the annealing temperature (Figure 4.80).

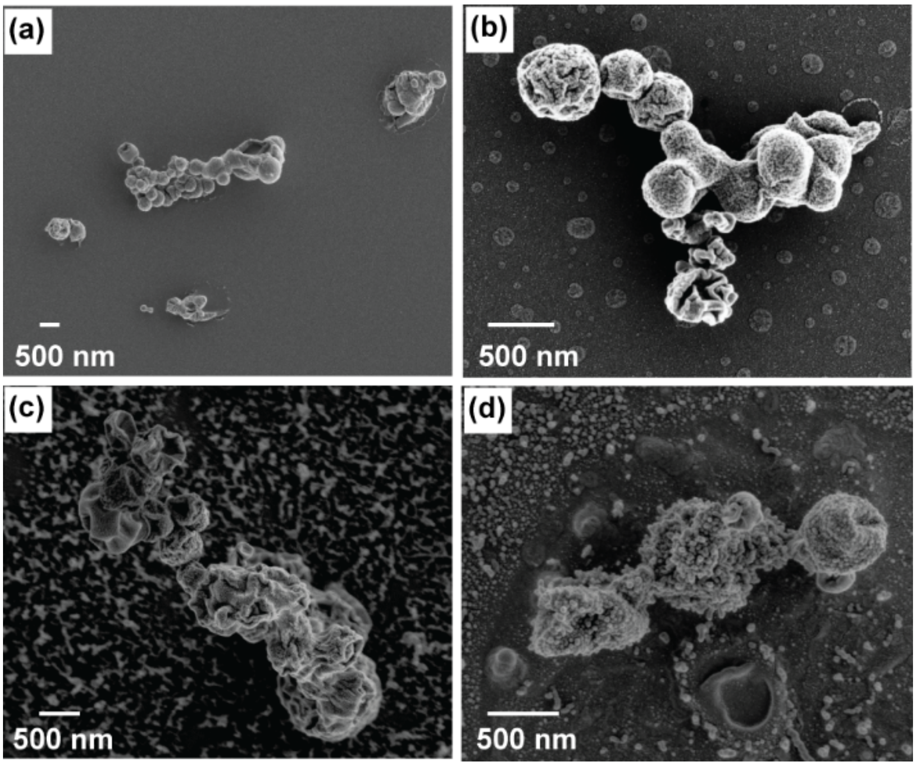

Figure 4.80. SEM images of mixed alumina-silicone nanostructures after annealing at (a) 300ºC, (b) 400ºC, (c) 500ºC, (d) 600ºC. Reprinted with permission from [177]

Aggregation of necklace structures was also observed when samples were analyzed under TEM. TEM images and elemental mapping of nanostructures annealed at various temperatures are shown in Figure 4.81 & Figure 4.82. Elemental mapping of the nanostructures revealed that after annealing the distribution of Al and Cl inside the nanostructures was inhomogeneous. The degree of inhomogeneity increased with an increase in the annealing temperature. The elemental distribution of O and Si remained homogenous even after annealing. It can also be observed that the nanostructures became hollow with an increase in annealing temperature. This suggests the thermal degradation of nanostructures.

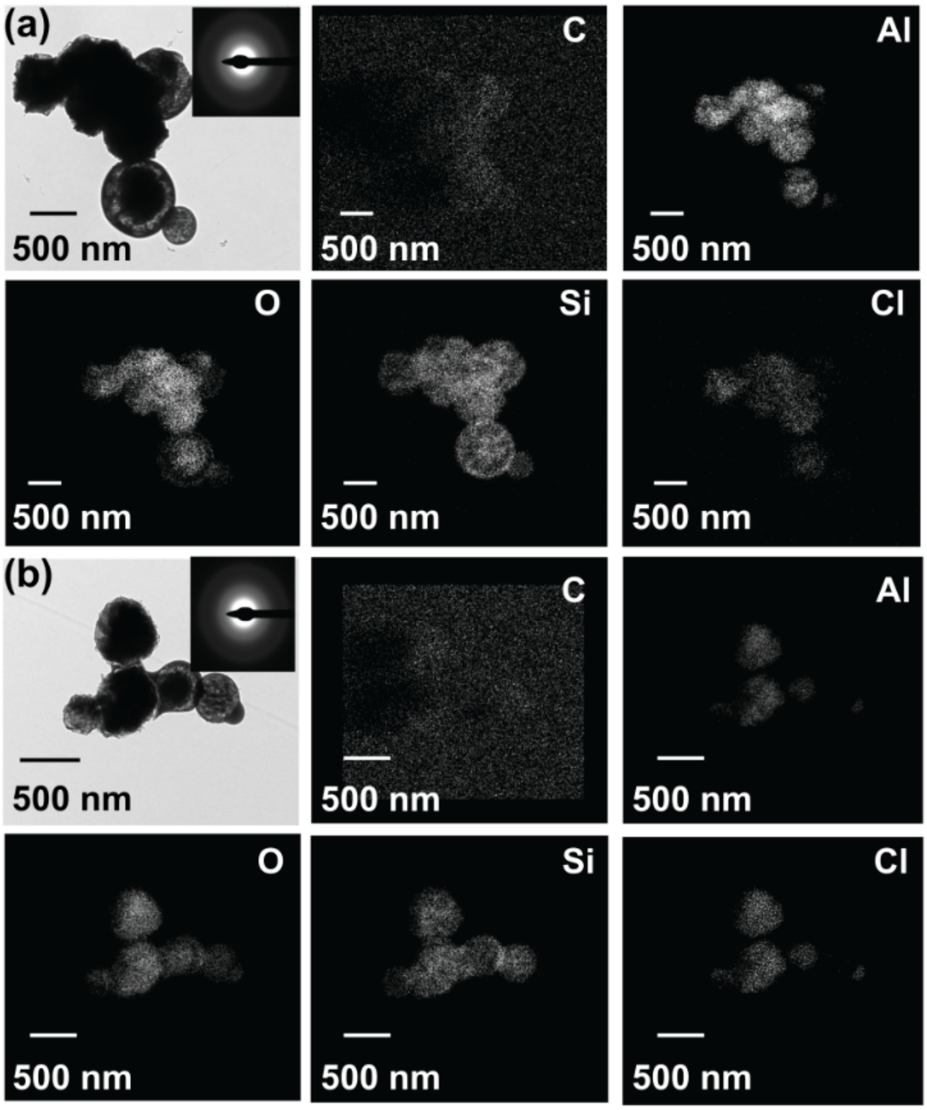

Figure 4.81. TEM images and elemental mapping of mixed alumina-silicone nanostructures annealed at (a) 300°C and (b) 400°C. Reprinted with permission from [177]

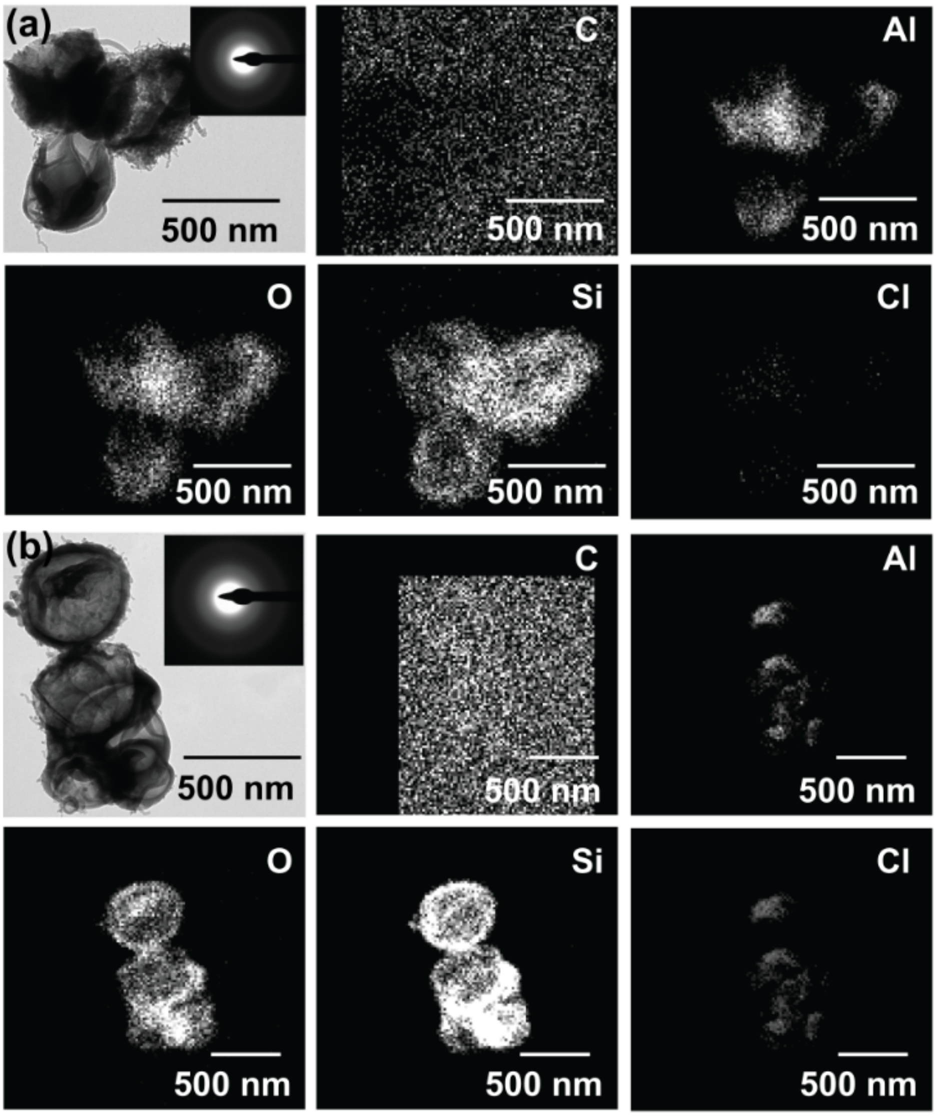

Figure 4.82. TEM images and elemental mapping of mixed alumina-silicone nanostructures annealed at (a) 500°C and (b) 600°C. Reprinted with permission from [177]

Annealing of mixed alumina-silicone nanostructures at 600°C was performed in air for a short duration of time such as 30 minutes and 1 hour and nanostructures were analysed using TEM and elemental mapping (Figure 4.83 & Figure 4.84). Degradation of nanostructures was still observed but due to short annealing duration the distribution of Al and Cl was quite homogenous inside the nanostructures and complete hollow structures were not observed.

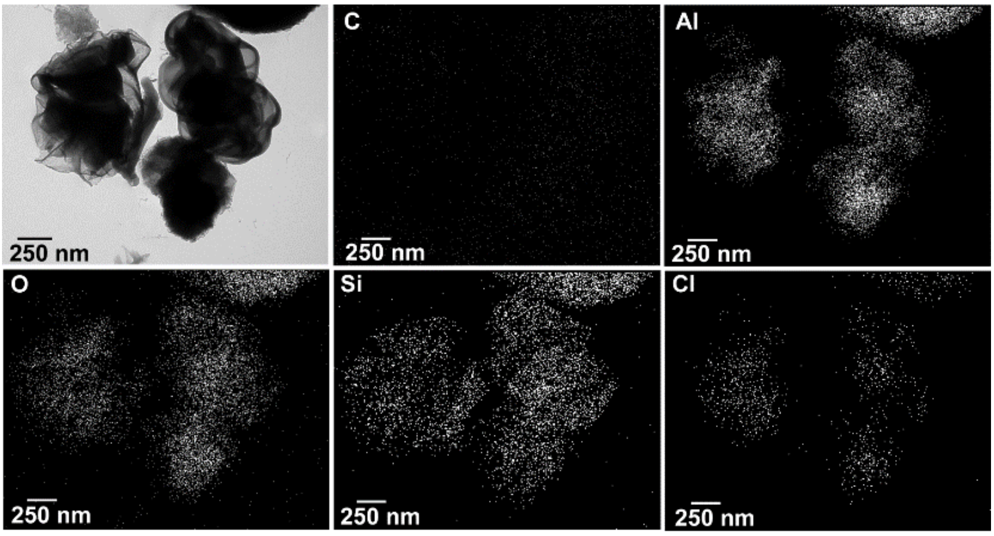

Figure 4.83. TEM image and elemental mapping of mixed alumina-silicone annealed at 600°C in air for the duration of 30 minutes

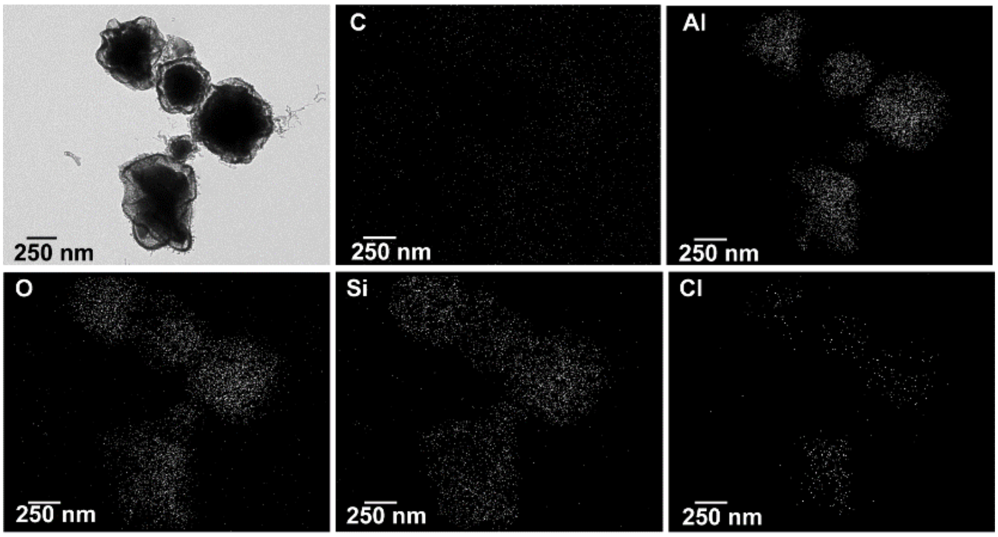

Figure 4.84. TEM image and elemental mapping of mixed alumina-silicone nanostructures annealed at 600°C in air for the duration of 1 hour

In summary, we have applied the DAGS method to synthesize various 1D nanomaterials using ambient conditions of temperature and pressure. The applicability of DAGS to silicone and non-silicone systems, ease of the procedure, less complicated instrumentation and use of liquid free handling are the important features of DAGS which make it to stand out from other conventional methods of synthesis for the production of 1D nanomaterials. The application of the DAGS method for the synthesis of alumina and mixed alumina-silicone nanostructures is very unique. However, it requires further investigations to understand in detail the degradation mechanism of these structures.

5. Summary and outlook

The ability to tailor the shape of growing materials at nanoscale is of vital importance as structures with different shapes and sizes exhibit considerably diverse properties as compared to their bulk counterparts. Especially, 1D nanostructures show remarkable properties due to their high aspect ratios. Therefore, the synthesis method employed to engineer various structures at nanoscale carries significant importance.

The droplet assisted growth and shaping (DAGS) method is an example of such elegant synthesis technique which has been applied for over a decade to synthesize various 1D silicone nanostructures called silicone nanofilaments (SNFs). The application of SNFs synthesized using the DAGS method has been widely explored for superhydrophobicity, superoleophobicity, oil/water separation, protein adsorption, catalysis and bacterial disinfection over couple of years research. The DAGS method differs considerably from conventional synthesis methods in terms of its unique synthesis approach and ease in execution. Instead of comprising metal catalyst particles to grow 1D nanostructures (as used in widely known VLS method), the DAGS method involves formation of water droplets at the substrate surface which act as reaction vessel and determine the shape of growing structures. Furthermore, this method gives the flexibility to carry synthesis at room temperature rather involving high processing temperature to generate reactive vapors. The facile processing using DAGS chemistry which involves less complicated and inexpensive instrumentation, and requires room temperature is a smart and economical synthesis technique. By keeping these characteristics of DAGS method in mind, this work focuses on the synthesis of 1D nanostructures using the DAGS method, characterization and application of nanostructures for various surface science applications.

The first part of this work focuses on classical SNFs which have been synthesized using DAGS chemistry. The as synthesized SNFs have been used for a rather new application, i.e. biomineralization. Due to the non-toxic nature of SNFs (as they consist of polysiloxanes), their high surface area has been explored to study the biomimetic growth of hydroxyapatite (HA) to check their potential use in orthopaedic implantation applications. HA is a major component of bone which comprises of over 60% of bone tissues, that is why this material has been extensively studied for bone tissue engineering, and efforts are made to innovate new economically affordable materials which enhance fast growth of HA. To study this, surface of SNFs has been functionalized with amine and carboxylic acid groups and submerged in simulated body fluid which has composition similar to human blood plasma. The fast growth of HA on functionalized SNFs has been observed as compared to non-SNFs coated substrates which demonstrate the high surface area of SNFs enhances the mineralization process and promotes fast growth. The facile, inexpensive and room temperature synthesis of SNFs using DAGS chemistry and ability to generate highly entangled network of 1D SNFs with high aspect ratios has shown its potential for biological applications. SNFs have revealed promising results for bone mineralization and they require further investigation to study their influence on the growth of human osteoblast cells to realize SNFs for *in vivo* applications.

The second part of this work also emphases on SNFs which have been employed to fabricate multifunctional coatings. By utilizing elegant DAGS chemistry to generate SNFs and combining it with inexpensive carbon nanofibers (CNFs) using one-step dip coating process, smart multifunctional coatings have been realized which possess superhydrophobicity, electric conductivity with tuneable water adhesion and optical transparency. By varying content of CNFs, the coatings exhibiting high contact angles up to $170.4^{o} \pm 1.8^{o}$ and low sliding angles $4.6^{o} \pm 0.91^{o}$ have been prepared. In addition, it has been demonstrated the coatings show excellent resistance to harsh environmental conditions such as extreme humidity and water immersion. Furthermore, the coatings showed high chemical resistance to fluids of varying pH after prolonged exposure. These exceptional properties of the prepared surfaces showed their potential for real life application where they can perform satisfactorily without appreciable deterioration. Another important aspect of such coatings is their resistance to mechanical forces such as abrasion or scratch which is often neglected. In this work, the attention has also been paid to improve the mechanical stability to these coatings. To tackle this, a rather uncommon polymer material has been utilized. Instead of using complex and time-consuming polymer synthesis strategies, a readily available Parafilm-M has been used to improve mechanical stability of the coatings. The coatings prepared by the addition of Parafilm-M showed enhanced resistance to abrasion forces and showed appreciable electric conductivity even after 50 abrasion cycles. The efficient DAGS synthesis approach combined with one step dip-coating is far better strategy in terms of i) ease in processing, ii) degree of complexity, iii) economics, and iv) time consumption when compared to already documented studies to generate such coatings. Furthermore, the coatings presented in this work exhibit superior properties in comparison to studies published earlier.

The facile DAGS method which has demonstrated its immense potential in the shaping of silicone required further research to generate nanostructures from other class of materials. The third part of this work focuses on the strategies which have been employed to extend the DAGS method to non-silicon system to demonstrate that applicability of this versatile method goes beyond silicone chemistry. The DAGS method of synthesis has been successfully applied to synthesize 1D nanostructures of germanium oxide referred as germanium oxide nanofilaments (GNFs). Germanium tetrachloride has been used as a precursor for the synthesis of GNFs which resulted in highly dense and homogenous growth of nanofilaments over the entire substrate surface. As the DAGS method utilizes formation of water droplets at the surface of substrate which is highly dependent on the relative humidity, the influence of relative humidity on the growth of GNFs has also been discussed in this work. It has been demonstrated that the formation of GNFs occurs at relative humidity levels of 30%, 35% and 40%, while very low e.g. 15% or very high humidity levels e.g. 50% and 70% did not result in formation of GNFs. It is worth to mention that despite of the fact, the synthesis is highly dependent on relative humidity, the synthesis of GNFs can be carried out in the humidity range of 30-40% providing a flexible window of operation. The characterization of as synthesized GNFs using X-ray photoelectron spectroscopy revealed, the nanofilaments exist as GeO and GeO_2 highlighting germanium tetrachloride undergoes hydrolysis to yield germanium hydroxide which polycondensates to germanium oxide. The high surface roughness of the substrate due to the presence of GNFs can be of potential use in the applications where high surface area or roughness can be of significant importance. To demonstrate this, the surface of GNFs has been functionalized using silane molecules to yield superhydrophobic and self-cleaning surfaces. It must be mentioned even though GNFs are soluble in water but after polysiloxane monolayer formation, GNFs show excellent resistance to water. The as synthesized high surface area GNFs using DAGS chemistry can find numerous applications in addition to anti-wetting (as presented here). The high aspect ratio of GNFs can be used to immobilize nanoparticles for catalytic application and they can also be used in the fabrication of opto-electronic devices. This work focused on extending the facile DAGS method to synthesize 1D nanostructures of germanium oxide, however to discover the broad spectrum of potential applications of this material additional studies are needed.

The final part of this work also involves shaping of nanostructures and it demonstrates the extension of DAGS method far beyond silicon or germanium systems. In this section of the work, the DAGS method has been applied to aluminum, to synthesize 1D necklace or bead type nanostructures of alumina. In addition, for the first time DAGS method has been applied to synthesized mixed alumina-silicone 1D nanostructures. Usually, the 1D nanostructures of alumina and mixed alumina-silicone are synthesized using CVD or hydrothermal approach employing high processing temperatures. The straightforward DAGS synthesis strategy presented here provide an alternative method to realize such structures at room temperature.

The characterization of as synthesized nanostructures revealed they are also dependent on the relative humidity and by changing humidity short or long range 1D structures can be obtained. One of the important point to be discussed here is the type of bonding existing in nanostructures. The spectroscopic techniques revealed the alumina nanostructures consist of Al-O-Al and alumina-silicone nanostructures consist of mixed Al-O-Al and Si-O-Si nanostructures instead of Al-O-Si. The successful extension of the DAGS method to synthesize germanium oxide, alumina and mixed alumina-silicone nanostructures show the universality and applicability of this synthesis method to a wide range of material systems.

Currently, the DAGS method has been successfully applied to only few materials and but its application can go beyond this. Given the facts this procedure involves energy efficient processing, is easy to perform, does not involve sophisticated instrumentation or produce liquid waste, show its potential in shape-controlled synthesis of nanomaterials. These traits make the DAGS method commercially and economically feasible procedure and require further studies to extend its spectrum to other material systems such as Ti, In, C, Sn to synthesize new types of nanostructures.

Finally, as the scope of this work focuses on the synthesis of nanostructures using the DAGS method and their application for various surface science applications, emphasis has been made on extending this facile synthesis strategy to various material systems to successfully synthesize 1D nanostructures. DAGS chemistry which has been widely applied for silicone nanofilaments synthesis has been for the first time extended to fabricate 1D nanostructures of various materials including germanium oxide, alumina and mixed alumina-silicone. In addition to synthesis and characterization of nanostructures using various material and surface characterization tools, this work also demonstrates area of application of nanostructures can be further expanded. The expansion in application spectrum has been demonstrated by utilizing SNFs as biomineralization support for orthopaedic applications and multifunctional coatings for smart surfaces. However, these are just few examples of the applications where 1D nanostructures can be used. With the given knowledge in surface science and ability to engineer the shape of materials at nanoscale using DAGS method, this can prove to be an exciting field of research for future work.

References

[1] G. R. J. Artus, S. Jung, J. Zimmermann, H.-P. Gautschi, K. Marquardt, S. Seeger, *Adv. Mater.* **2006**, *18*, 2758–2762.

[2] J. Zhang, L. Li, B. Li, S. Seeger, *RSC Adv.* **2014**, *4*, 33424–33430.

[3] G. R. J. Artus, S. Seeger, *Ind. Eng. Chem. Res.* **2012**, *51*, 2631–2636.

[4] J. Zimmermann, G. R. J. Artus, S. Seeger, *Appl. Surf. Sci.* **2007**, *253*, 5972–5979.

[5] J. Zimmermann, G. R. J. Artus, S. Seeger, *J. Adhes. Sci. Technol.* **2008**, *22*, 251–263.

[6] J. Zimmermann, F. A. Reifler, G. Fortunato, L.-C. Gerhardt, S. Seeger, *Adv. Funct. Mater.* **2008**, *18*, 3662–3669.

[7] G. R. J. Artus, S. Seeger, *Adv. Colloid Interface Sci.* **2014**, *209*, 144–162.

[8] J. Zimmermann, M. Rabe, G. R. J. Artus, S. Seeger, *Soft Matter* **2008**, *4*, 450–452.

[9] H. Gau, S. Herminghaus, P. Lenz, R. Lipowsky, *Science (80-.).* **1999**, *283*, 46 LP-49.

[10] G. R. Meseck, R. Kontic, G. R. Patzke, S. Seeger, *Adv. Funct. Mater.* **2012**, *22*, 4433–4438.

[11] A. S. M. Meier, S. Seeger, *Small* **2017**, *13*, 1601072.

[12] J. Zimmermann, M. Rabe, D. Verdes, S. Seeger, *Langmuir* **2008**, *24*, 1053–1057.

[13] T. Young, *Philos. Trans. R. Soc.* **1805**, *95*.

[14] R. N. Wenzel, *Ind. Eng. Chem.* **1936**, *28*, 988–994.

[15] A. B. D. Cassie, S. Baxter, *Trans. Faraday Soc.* **1944**, *40*, 546–551.

[16] M. N. Rittner, *J. Miner. Met. Mater. Soc.* **2004**, *56*, 22–26.

[17] G. B. Khomutov, V. V Kislov, M. N. Antipina, R. V Gainutdinov, S. P. Gubin, A. Y. Obydenov, S. A. Pavlov, A. A. Rakhnyanskaya, A. N. Sergeev-Cherenkov, E. S. Soldatov, et al., *Microelectron. Eng.* **2003**, *69*, 373–383.

[18] A. Serrà, S. Grau, C. Gimbert-Suriñach, J. Sort, J. Nogués, E. Vallés, *Appl. Catal. B Environ.* **2017**, *217*, 81–91.

[19] K. Jiang, D. Zhao, S. Guo, X. Zhang, X. Zhu, J. Guo, G. Lu, X. Huang, *Sci. Adv.* **2017**, *3*, e1601705.

[20] G. Otnes, M. T. Borgström, *Nano Today* **2017**, *12*, 31–45.

[21] M.-A. Doucey, S. Carrara, *Trends Biotechnol.* **2019**, *37*, 86–99.

[22] F. Patolsky, C. M. Lieber, *Mater. Today* **2005**, *8*, 20–28.

[23] J. Kim, H.-C. Lee, K.-H. Kim, M.-S. Hwang, J.-S. Park, J. M. Lee, J.-P. So, J.-H. Choi, S.-H. Kwon, C. J. Barrelet, et al., *Nat. Nanotechnol.* **2017**, *12*, 963.

[24] J.-L. Wang, Y.-R. Lu, H.-H. Li, J.-W. Liu, S.-H. Yu, *J. Am. Chem. Soc.* **2017**, *139*, 9921–9926.

[25] D. C. Kim, B. H. Kong, H. K. Cho, *J. Mater. Sci. Mater. Electron.* **2008**, *19*, 760–763.

[26] P. H. and B. M. and J. Piqueras, *Nanotechnology* **2007**, *18*, 155203.

[27] R. Brukh, S. Mitra, *Chem. Phys. Lett.* **2006**, *424*, 126–132.

[28] P. Viswanathamurthi, N. Bhattarai, H. Y. Kim, M. S. Khil, D. R. Lee, E.-K. Suh, *J. Chem. Phys.* **2004**, *121*, 441–445.

[29] Z. W. Pan, Z. R. Dai, Z. L. Wang, *Science (80-.).* **2001**, *291*, 1947 LP-1949.

[30] Y.-L. Cao, D.-Z. Jia, L. Liu, J.-M. Luo, *Chinese J. Chem.* **2004**, *22*, 1288–1290.

[31] B. Wang, Y. H. Yang, G. W. Yang, *Nanotechnology* **2006**, *17*, 4682–4688.

[32] X. Y. Kong, Z. L. Wang, *Nano Lett.* **2003**, *3*, 1625–1631.

[33] S. Tsoi, E. Fok, J. C. Sit, J. G. C. Veinot, *Chem. Mater.* **2006**, *18*, 5260–5266.

[34] X. Wang, Y. Li, *J. Am. Chem. Soc.* **2002**, *124*, 2880–2881.

[35] M. A. Dar, Y. S. Kim, W. B. Kim, J. M. Sohn, H. S. Shin, *Appl. Surf. Sci.* **2008**, *254*, 7477–7481.

[36] A. Phuruangrat, D. J. Ham, S. J. Hong, S. Thongtem, J. S. Lee, *J. Mater. Chem.* **2010**, *20*, 1683–1690.

[37] M. Chen, Y. Xie, J. Lu, Y. Xiong, S. Zhang, Y. Qian, X. Liu, *J. Mater. Chem.* **2002**, *12*, 748–753.

[38] W. Qingqing, X. Gang, H. Gaorong, *J. Solid State Chem.* **2005**, *178*, 2680–2685.

[39] M. Bechelany, A. Amin, A. Brioude, D. Cornu, P. Miele, *J. Nanoparticle Res.* **2012**, *14*, 980.

[40] H. Cao, X. Qiu, Y. Liang, L. Zhang, M. Zhao, Q. Zhu, *ChemPhysChem* **2006**, *7*, 497–501.

[41] R. S. Devan, R. A. Patil, J.-H. Lin, Y.-R. Ma, *Adv. Funct. Mater.* **2012**, *22*, 3326–3370.

[42] C. L. and G. F. and S. X. and D. Z. and X. Zhao, *Nanotechnology* **2006**, *17*, 5367.

[43] S. H. L. and Q. W. and W. L. L. and M. Z. and Z. F. D. and S. Y. W. and Z. T. S. and C. L. L. and J. Y. Dai, *Nanotechnology* **2004**, *15*, 1424.

[44] and Z. L. W. Z. W. Pan, Z. R. Dai, *Appl. Phys. Lett.* **2002**, *80*, 309–311.

[45] J.-M. W. and H. C. S. and W.-T. Wu, *Nanotechnology* **2006**, *17*, 105.

[46] H. Lv, D. Sang, H. Li, X. Du, D. Li, G. Zou, *Nanoscale Res. Lett.* **2010**, *5*, 620–624.

[47] A. A. Ansari, M. Alhoshan, M. S. Alsalhi, A. S. Aldwayyan, *Sensors* **2010**, *10*, DOI 10.3390/s100706535.

[48] H. Zheng, J. Zhong, W. Wang, Y. Zheng, C. Ma, *Thin Solid Films* **2008**, *516*, 4983–4987.

[49] S. Cao, C. Guo, Y. Wang, J. Miao, Z. Zhang, Q. Liu, *Solid State Commun.* **2009**, *149*, 87–90.

[50] P. Sundara Venkatesh, V. Ramakrishnan, K. Jeganathan, *CrystEngComm* **2012**, *14*, 3907–3914.

[51] B. Sirota, J. Reyes-Cuellar, P. Kohli, L. Wang, M. E. McCarroll, S. M. Aouadi, *Thin Solid Films* **2012**, *520*, 6118–6123.

[52] T. K. Kazuki Nagashima, Takeshi Yanagidaa, Hidekazu Tanaka, *J. Appl. Phys.* **2007**, *101*, 124304.

[53] J. Q. Hu, Y. Bando, Q. L. Liu, D. Golberg, *Adv. Funct. Mater.* **2003**, *13*, 493–496.

[54] S. Choopun, H. Tabata, T. Kawai, *J. Cryst. Growth* **2005**, *274*, 167–172.

[55] F. Kokai, K. Uchiyama, T. Shimazu, A. Koshio, *Appl. Phys. A* **2010**, *101*, 497–502.

[56] X. Duan, C. M. Lieber, *J. Am. Chem. Soc.* **2000**, *122*, 188–189.

[57] H. Zeng, X.-W. Du, S. C. Singh, S. A. Kulinich, S. Yang, J. He, W. Cai, *Adv. Funct. Mater.* **2012**, *22*, 1333–1353.

[58] Z. Huang, H. Fang, J. Zhu, *Adv. Mater.* **2007**, *19*, 744–748.

[59] C. L. Cheung, R. J. Nikolić, C. E. Reinhardt, T. F. Wang, *Nanotechnology* **2006**, *17*, 1339–1343.

[60] S. Donthu, Z. Pan, B. Myers, G. Shekhawat, N. Wu, V. Dravid, *Nano Lett.* **2005**, *5*, 1710–1715.

[61] V. Gopal, E. A. Stach, V. R. Radmilovic, I. A. Mowat, *Appl. Phys. Lett.* **2004**, *85*, 49–51.

[62] S. D. T. S. V. Dravid, *Adv. Mater.* **2007**, 125–128.

[63] J. C. Hulteen, C. R. Martin, *J. Mater. Chem.* **1997**, *7*, 1075–1087.

[64] Y. C. Choi, J. Kim, S. D. Bu, *Mater. Sci. Eng. B* **2006**, *133*, 245–249.

[65] C. Xu, G. Xu, Y. Liu, G. Wang, *Solid State Commun.* **2002**, *122*, 175–179.

[66] C. Xu, X. Zhao, S. Liu, G. Wang, *Solid State Commun.* **2003**, *125*, 301–304.

[67] C. Xu, G. Xu, G. Wang, *J. Mater. Sci.* **2003**, *38*, 779–782.

[68] A. Vantomme, Z.-Y. Yuan, G. Du, B.-L. Su, *Langmuir* **2005**, *21*, 1132–1135.

[69] K. Gerasopoulos, M. McCarthy, P. Banerjee, X. Fan, J. N. Culver, R. Ghodssi, *Nanotechnology* **2010**, *21*, 55304.

[70] D. Barreca, D. Bekermann, E. Comini, A. Devi, R. A. Fischer, A. Gasparotto, C. Maccato, G. Sberveglieri, E. Tondello, *Sensors Actuators B Chem.* **2010**, *149*, 1–7.

[71] M. F. Meléndrez, F. Solis-Pomar, C. D. Gutierrez-Lazos, P. Flores, A. F. Jaramillo, A. Fundora, E. Pérez-Tijerina, *Ceram. Int.* **2016**, *42*, 1160–1168.

[72] H. Huang, O. K. Tan, Y. C. Lee, M. S. Tse, J. Guo, T. White, *Nanotechnology* **2006**, *17*, 3668–3672.

[73] Z. Wang, H. Ogata, S. Morimoto, J. Ortiz-Medina, M. Fujishige, K. Takeuchi, H. Muramatsu, T. Hayashi, M. Terrones, Y. Hashimoto, et al., *Carbon N. Y.* **2015**, *94*, 479–484.

[74] V. Kaushik, A. K. Shukla, V. D. Vankar, *Appl. Phys. A* **2014**, *117*, 2197–2205.

[75] Y. Yao, F. Li, S.-T. Lee, *Chem. Phys. Lett.* **2005**, *406*, 381–385.

[76] C. Mudi, Z. Xiaodong, K. Bo, D. Fang, W. Xiaohui, Z. Haiyang, *Plasma Sci. Technol.* **2010**, *12*, 547–550.

[77] J. Thangala, S. Vaddiraju, R. Bogale, R. Thurman, T. Powers, B. Deb, M. K. Sunkara, *Small* **2007**, *3*, 890–896.

[78] S. Mitra, K. Sridharan, J. Unnam, K. Ghosh, *Thin Solid Films* **2008**, *516*, 798–802.

[79] V. Chakrapani, M. Brier, A. Puntambekar, T. DiGiovanni, *J. Mater. Res.* **2016**, *31*, 17–27.

[80] N.-H. Saddiqi, D. Patra, S. Seeger, *ChemPhysChem* **2019**, *20*, 538–544.

[81] J. S. Veinot, Jonathan Gordon Conn, De-ann Rollings, Shufen Tsoi, *U.S. Pat. Appl.* **2008**.

[82] Gao, T. J. McCarthy, *Langmuir* **2008**, *24*, 362–364.

[83] A. Stojanovic, S. Olveira, M. Fischer, S. Seeger, *Chem. Mater.* **2013**, *25*, 2787–2792.

[84] G. R. J. Artus, S. Olveira, D. Patra, S. Seeger, *Macromol. Rapid Commun.* **2017**, *38*, 1600558.

[85] R. S. Wagner, W. C. Ellis, *Appl. Phys. Lett.* **1964**, *4*, 89–90.

[86] Y.-R. Ma, C.-M. Lin, C.-L. Yeh, R.-T. Huang, *J. Vac. Sci. Technol. B Microelectron. Nanom.*

Struct. Process. Meas. Phenom. **2005**, *23*, 2141–2145.

[87] L. Kumari, J.-H. Lin, Y.-R. Ma, *J. Phys. Condens. Matter* **2007**, *19*, 406204.

[88] Y. L. and Y.-R. M. Rupesh S. Devan, Jin-Han Lin, Wei-Der Ho, Sheng Yun Wu, *J. Appl. Crystallogr.* **2010**, *43*, 1062–1067.

[89] Y.-J. Hsu, S.-Y. Lu, *J. Phys. Chem. B* **2005**, *109*, 4398–4403.

[90] P. A. Sedach, T. J. Gordon, S. Y. Sayed, T. Fürstenhaupt, R. Sui, T. Baumgartner, C. P. Berlinguette, *J. Mater. Chem.* **2010**, *20*, 5063–5069.

[91] J. Zimmermann, G. R. J. Artus, S. Seeger, *Superhydrophobic Coating*, **2004**, WO20040623.

[92] P. Cao, K. Xu, J. O. Varghese, J. R. Heath, *Nano Lett.* **2011**, *11*, 5581–5586.

[93] M. James, T. A. Darwish, S. Ciampi, S. O. Sylvester, Z. Zhang, A. Ng, J. J. Gooding, T. L. Hanley, *Soft Matter* **2011**, *7*, 5309–5318.

[94] J. E. Mates, I. S. Bayer, J. M. Palumbo, P. J. Carroll, C. M. Megaridis, *Nat. Commun.* **2015**, *6*, 8874.

[95] B. K. Sarma, A. Das, P. Barman, A. R. Pal, *J. Phys. D. Appl. Phys.* **2016**, *49*, 145304.

[96] P. Ducheyne, Q. Qiu, *Biomaterials* **1999**, *20*, 2287–2303.

[97] N. Eliaz, M. Eliyahu, *J. Biomed. Mater. Res. Part A* **2007**, *80A*, 621–634.

[98] J. Ma, C. Wang, K. W. Peng, *Biomaterials* **2003**, *24*, 3505–3510.

[99] M. H. Fathi, A. Hanifi, *Mater. Lett.* **2007**, *61*, 3978–3983.

[100] C. F. Koch, S. Johnson, D. Kumar, M. Jelinek, D. B. Chrisey, A. Doraiswamy, C. Jin, R. J. Narayan, I. N. Mihailescu, *Mater. Sci. Eng. C* **2007**, *27*, 484–494.

[101] L. Sun, C. C. Berndt, K. A. Gross, A. Kucuk, *J. Biomed. Mater. Res.* **2001**, *58*, 570–592.

[102] Y. W. Gu, K. A. Khor, P. Cheang, *Biomaterials* **2003**, *24*, 1603–1611.

[103] H. Li, W. Huang, Y. Zhang, M. Zhong, *Mater. Sci. Eng. C* **2007**, *27*, 756–761.

[104] Q. Liu, J. Ding, F. K. Mante, S. L. Wunder, G. R. Baran, *Biomaterials* **2002**, *23*, 3103–3111.

[105] A. Díaz, T. López, J. Manjarrez, E. Basaldella, J. M. Martínez-Blanes, J. A. Odriozola, *Acta Biomater.* **2006**, *2*, 173–179.

[106] L. Jongpaiboonkit, T. Franklin-Ford, W. L. Murphy, *ACS Appl. Mater. Interfaces* **2009**, *1*, 1504–1511.

[107] H. Liu, P. Xi, G. Xie, Y. Shi, F. Hou, L. Huang, F. Chen, Z. Zeng, C. Shao, J. Wang, *J. Phys. Chem. C* **2012**, *116*, 3334–3341.

[108] S. Flink, F. C. J. M. van Veggel, D. N. Reinhoudt, *J. Phys. Org. Chem.* **2001**, *14*, 407–415.

[109] N.-H. Saddiqi, D. Patra, S. Seeger, *Colloid Interface Sci. Commun.* **2017**, *16*, 1–5.

[110] B. A. Allo, A. S. Rizkalla, K. Mequanint, *ACS Appl. Mater. Interfaces* **2012**, *4*, 3148–3156.

[111] Y. Lu, S. Sathasivam, J. Song, C. R. Crick, C. J. Carmalt, I. P. Parkin, *Science (80-.).* **2015**, *347*, 1132 LP-1135.

[112] F. Guo, Q. Wen, Y. Peng, Z. Guo, *J. Colloid Interface Sci.* **2017**, *494*, 54–63.

[113] N. Wang, D. Xiong, Y. Deng, Y. Shi, K. Wang, *ACS Appl. Mater. Interfaces* **2015**, *7*, 6260–6272.

[114] Y. Lai, Y. Tang, J. Gong, D. Gong, L. Chi, C. Lin, Z. Chen, *J. Mater. Chem.* **2012**, *22*, 7420–7426.

[115] U. Mehmood, F. A. Al-Sulaiman, B. S. Yilbas, B. Salhi, S. H. A. Ahmed, M. K. Hossain, *Sol. Energy Mater. Sol. Cells* **2016**, *157*, 604–623.

[116] X. Su, H. Li, X. Lai, L. Zhang, X. Liao, J. Wang, Z. Chen, J. He, X. Zeng, *ACS Appl. Mater. Interfaces* **2018**, *10*, 4213–4221.

[117] G. B. Hwang, A. Patir, K. Page, Y. Lu, E. Allan, I. P. Parkin, *Nanoscale* **2017**, *9*, 7588–7594.

[118] Z. Chu, Y. Feng, S. Seeger, *Angew. Chemie Int. Ed.* **2015**, *54*, 2328–2338.

[119] J. Zhang, S. Seeger, *ChemPhysChem* **2013**, *14*, 1646–1651.

[120] Z.-T. Li, B. Lin, L.-W. Jiang, E.-C. Lin, J. Chen, S.-J. Zhang, Y.-W. Tang, F.-A. He, D.-H. Li, *Appl. Surf. Sci.* **2018**, *427*, 56–64.

[121] I. S. Bayer, A. Biswas, G. Ellialtioglu, *Polym. Compos.* **2011**, *32*, 576–585.

[122] I. S. Bayer, V. Caramia, D. Fragouli, F. Spano, R. Cingolani, A. Athanassiou, *J. Mater. Chem.* **2012**, *22*, 2057–2062.

[123] J. Zang, S. Ryu, N. Pugno, Q. Wang, Q. Tu, M. J. Buehler, X. Zhao, *Nat. Mater.* **2013**, *12*, 321.

[124] A. Das, C. M. Megaridis, L. Liu, T. Wang, A. Biswas, *Appl. Phys. Lett.* **2011**, *98*, DOI 10.1063/1.3583523.

[125] C. P. Wong, K. S. Moon, in *Nano-Bio- Electron. Photonic MEMS Packag.*, **2010**, pp. 1–17.

[126] C. Luo, X. Zuo, L. Wang, E. Wang, S. Song, J. Wang, J. Wang, C. Fan, Y. Cao, *Nano Lett.* **2008**, *8*, 4454–4458.

[127] M. Peng, Z. Liao, J. Qi, Z. Zhou, *Langmuir* **2010**, *26*, 13572–13578.

[128] F. Zhang, H. Qian, L. Wang, Z. Wang, C. Du, X. Li, D. Zhang, *Surf. Coatings Technol.* **2018**, *341*, 15–23.

[129] L. Zhao, W. L. Liu, L. D. Zhang, J. S. Yao, W. H. Xu, X. Q. Wang, Y. Z. Wu, *Colloids Surfaces A Physicochem. Eng. Asp.* **2013**, *423*, 69–76.

[130] H. Hu, Z. Zhao, W. Wan, Y. Gogotsi, J. Qiu, *ACS Appl. Mater. Interfaces* **2014**, *6*, 3242–3249.

[131] L. Zhu, Y. , Zhang, J. C., Zhai, J. , Zheng, Y. M., Feng, L. and Jiang, *Chem. Eur. J. Chem. Phys.* **2006**, *7*, 336–341.

[132] N.-H. Saddiqi, S. Seeger, *Adv. Mater. Interfaces* **2019**, *6*, 1900041.

[133] J. C. L. and W. O. and P. H. V. and P. Bergveld, *J. Micromechanics Microengineering* **1997**, *7*, 145.

[134] W. Luheng, D. Tianhuai, W. Peng, *Sensors Actuators A Phys.* **2007**, *135*, 587–592.

[135] D. Quére, A. Lafuma, J. Bico, *Nanotechnology* **2003**, *14*, 1109–1112.

[136] A. Das, H. T. Hayvaci, M. K. Tiwari, I. S. Bayer, D. Erricolo, C. M. Megaridis, *J. Colloid Interface Sci.* **2011**, *353*, 311–315.

[137] A. Das, T. M. Schutzius, I. S. Bayer, C. M. Megaridis, *Carbon N. Y.* **2012**, *50*, 1346–1354.

[138] K. Chen, W. Gou, L. Xu, Y. Zhao, *Compos. Sci. Technol.* **2018**, *156*, 177–185.

[139] N. Mittal, D. Deva, R. Kumar, A. Sharma, *Carbon N. Y.* **2015**, *93*, 492–501.

[140] M. Sansotera, W. Navarrini, G. Resnati, P. Metrangolo, A. Famulari, C. L. Bianchi, P. A.

Guarda, *Carbon N. Y.* **2010**, *48*, 4382–4390.

[141] L. Shen, H. Ding, Q. Cao, W. Jia, W. Wang, Q. Guo, *Carbon N. Y.* **2012**, *50*, 4284–4290.

[142] L. Ye, J. Guan, Z. Li, J. Zhao, C. Ye, J. You, Y. Li, *Langmuir* **2017**, *33*, 1368–1374.

[143] J. T. Han, B. K. Kim, J. S. Woo, J. I. Jang, J. Y. Cho, H. J. Jeong, S. Y. Jeong, S. H. Seo, G.-W. Lee, *ACS Appl. Mater. Interfaces* **2017**, *9*, 7780–7786.

[144] M. Peng, J. Qi, Z. Zhou, Z. Liao, Z. Zhu, H. Guo, *Langmuir* **2010**, *26*, 13062–13064.

[145] L.-Y. Meng, S.-J. Park, *J. Colloid Interface Sci.* **2010**, *342*, 559–563.

[146] H. Yao, C.-C. Chu, H.-J. Sue, R. Nishimura, *Carbon N. Y.* **2013**, *53*, 366–373.

[147] J. Yang, Z. Zhang, X. Men, X. Xu, *Appl. Surf. Sci.* **2009**, *255*, 9244–9247.

[148] J. Zou, H. Chen, A. Chunder, Y. Yu, Q. Huo, L. Zhai, *Adv. Mater.* **2008**, *20*, 3337–3341.

[149] G.-W. L. Joong Tark Han, Sun Young Kim, Jong Seok Woo, *Adv. Mater.* **2008**, 3724–3727.

[150] W. Yao, K.-J. Bae, M. Y. Jung, Y.-R. Cho, *J. Colloid Interface Sci.* **2017**, *506*, 429–436.

[151] P. O. Caffrey, M. C. Gupta, *Appl. Surf. Sci.* **2014**, *314*, 40–45.

[152] Y. Wang, X. Li, *Chem. – A Eur.* **2003**, *9*, 5627–5635.

[153] Y. Cui, C. M. Lieber, *Science (80-.).* **2001**, *291*, 851 LP-853.

[154] Y. Jiao, A. M. Hafez, D. Cao, A. Mukhopadhyay, Y. Ma, H. Zhu, *Small* **2018**, *14*, 1800640.

[155] R. A. & C. M. L. Xiangfeng Duan, Yu Huang, *Nature* **2003**, *421*, pages 241–245.

[156] L. Zhu, Y. , Li, J. , Wan, M. and Jiang, *Macromol. Rapid Commun.* **2008**, *29*, 239–243.

[157] K. W. Kolasinski, *Curr. Opin. Solid State Mater. Sci.* **2006**, *10*, 182–191.

[158] H. Wang, L. A. Zepeda-Ruiz, G. H. Gilmer, M. Upmanyu, *Nat. Commun.* **2013**, *4*, 1956.

[159] S. N. Mohammad, *Nano Lett.* **2008**, *8*, 1532–1538.

[160] T. P. H. Muhammad A Khan, Muhammad Farhan, in *IEEE Nanotechnol. Mater. Devices Conf.*, **2009**, pp. 5–8.

[161] Z. G. Bai, D. P. Yu, H. Z. Zhang, Y. Ding, Y. P. Wang, X. Z. Gai, Q. L. Hang, G. C. Xiong, S. Q. Feng, *Chem. Phys. Lett.* **1999**, *303*, 311–314.

[162] L. Armelao, F. Heigl, P.-S. G. Kim, R. A. Rosenberg, T. Z. Regier, T.-K. Sham, *J. Phys. Chem. C* **2012**, *116*, 14163–14169.

[163] Y. H. Tang, Y. F. Zhang, N. Wang, I. Bello, C. S. Lee, S. T. Lee, *Appl. Phys. Lett.* **1999**, *74*, 3824–3826.

[164] X. C. Wu, W. H. Song, B. Zhao, Y. P. Sun, J. J. Du, *Chem. Phys. Lett.* **2001**, *349*, 210–214.

[165] Y. Zhang, J. Zhu, Q. Zhang, Y. Yan, N. Wang, X. Zhang, *Chem. Phys. Lett.* **2000**, *317*, 504–509.

[166] L. Z. Pei, H. S. Zhao, W. Tan, Q. F. Zhang, *J. Appl. Phys.* **2009**, *105*, 54313.

[167] S. J. L. R. Denise T. B. De Salvi, Aldo E. Job, *J. Brazilian Chem. Soc.* **2015**, *26*, 992–1003.

[168] S. Deng, Q. Xie, D. Deduytsche, M. Schaekers, D. Lin, M. Caymax, A. Delabie, S. Van Den Berghe, X. Qu, C. Detavernier, *Appl. Phys. Lett.* **2011**, *99*, DOI 10.1063/1.3622649.

[169] V. Grossi, L. Ottaviano, S. Santucci, M. Passacantando, *J. Non. Cryst. Solids* **2010**, *356*, 1988–

1993.

[170] X. Wang, Z. Zhao, J. Xiang, W. Wang, J. Zhang, C. Zhao, T. Ye, *Appl. Surf. Sci.* **2016**, *390*, 472–480.

[171] D. E. Rollings, J. G. C. Veinot, *Langmuir* **2008**, *24*, 13653–13662.

[172] S. K. Wang, K. Kita, C. H. Lee, T. Tabata, T. Nishimura, K. Nagashio, A. Toriumi, *J. Appl. Phys.* **2010**, *108*, 54104.

[173] Z. Jiang, T. Xie, G. Z. Wang, X. Y. Yuan, C. H. Ye, W. P. Cai, G. W. Meng, G. H. Li, L. D. Zhang, *Mater. Lett.* **2005**, *59*, 416–419.

[174] D.-Y. Kang, N. A. Brunelli, G. I. Yucelen, A. Venkatasubramanian, J. Zang, J. Leisen, P. J. Hesketh, C. W. Jones, S. Nair, *Nat. Commun.* **2014**, *5*, 3342.

[175] Q. Qin, T. Kim, X. Duan, J. Lian, W. Zheng, *Cryst. Growth Des.* **2016**, *16*, 6139–6143.

[176] N. Jeong, S. Hong, C. Kim, K. Kim, *J. Am. Ceram. Soc.* **2015**, *98*, 4036–4043.

[177] N.-H. Saddiqi, S. Seeger, *J. Colloid Interface Sci.* **2019**, DOI https://doi.org/10.1016/j.jcis.2019.09.122.

[178] O. M. C. Reyes, Carlos Alberto Ríos, Williams, Craig, & Alarcón, *Mater. Res.* **2013**, *16(2)*, 424–438.

[179] A. ADAMCZYK, *Mater. Sci.* **2015**, *33*, 732–741.

[180] R. Chen, X. Zhang, Z. Su, R. Gong, X. Ge, H. Zhang, C. Wang, *J. Phys. Chem. C* **2009**, *113*, 8350–8356.

[181] G. P. Bhaskar J. Saikia, *J. Mod. Phys.* **2010**, *1*, 206–210.

[182] P. Padmaja, G. M. Anilkumar, P. Mukundan, G. Aruldhas, K. G. K. Warrier, *Int. J. Inorg. Mater.* **2001**, *3*, 693–698.

[183] F. Bauer, H.-J. Gläsel, U. Decker, H. Ernst, A. Freyer, E. Hartmann, V. Sauerland, R. Mehnert, *Prog. Org. Coatings* **2003**, *47*, 147–153.

[184] I. Mora-Barrantes, J. L. Valentín, A. Rodríguez, I. Quijada-Garrido, R. Paris, *J. Mater. Chem.* **2012**, *22*, 1403–1410.

[185] T. M. Arantes, A. H. Pinto, E. R. Leite, E. Longo, E. R. Camargo, *Colloids Surfaces A Physicochem. Eng. Asp.* **2012**, *415*, 209–217.

[186] C.-Y. C. Hsing-I Hsiang, *J. Am. Ceram. Soc.* **2008**, *91*, 387–390.

[187] E. Lippmaa, M. Maegi, A. Samoson, G. Engelhardt, A. R. Grimmer, *J. Am. Chem. Soc.* **1980**, *102*, 4889–4893.

[188] W. W.-L. Shao, NMR Studies of Amorphous Silicon and Aluminosilicate Glass, Iowa State University, **1989**.

Curriculum Vitae

Name: Saddiqi

First Name: Naeem-ul-Hasan

Date of Birth: February 15, 1991

Nationality: Pakistani

Education:

05/2015 – present	**PhD Candidate at Department of Chemistry** University of Zurich, Switzerland
09/2012 – 02/2015	**M.Sc. Hons. Advanced Materials and Processes** Friedrich-Alexander University of Erlangen-Nuremberg, Germany
09/2008 – 08/2012	**B.Sc. Metallurgical and Materials Engineering** University of Engineering & Technology, Lahore, Pakistan